

SCANNING TUNNELING MICROSCOPY STUDIES OF SUPERCONDUCTING SINGLE
LAYER IRON SELENIDE ON STRONTIUM TITANATE

by

Zhuozhi Ge

A Dissertation Submitted in

Partial Fulfilment of the

Requirements for the Degree of

Doctor of Philosophy

in Physics

at

The University of Wisconsin - Milwaukee

August 2018

ABSTRACT

SCANNING TUNNELING MICROSCOPY STUDIES OF SUPERCONDUCTING SINGLE LAYER IRON SELENIDE ON STRONTIUM TITANATE

by

Zhuozhi Ge

The University of Wisconsin – Milwaukee, 2018
Under the Supervision of Professor Lian Li and Professor Michael Weinert

The search for high temperature superconductivity has been a prominent topic in the field of condensed matter physics ever since the discovery of this novel phenomenon more than 100 years ago. In addition to the search for new materials, interfacial superconductivity has shown great potential as demonstrated recently in monolayer FeSe grown on SrTiO₃ (STO) (001) substrate, where superconducting transition temperature (T_c) has been enhanced by more than an order of magnitude compared to the bulk value. The uniqueness of this approach is the direct placement of the superconducting layer on a secondary substrate, which facilitates the independent control of interfacial interactions by methods such as electrical doping and optical gating. In addition, due to low dimensional nature of single layer film, quantum size effect is also expected to modify the superconductivity that allows for further tailoring. However, much is still unknown in this single layer FeSe/STO system. In particular, the substrate doping from the STO leads to distinct Fermi surface and band structure for the FeSe, giving rise to the pairing symmetry that is different from most of the iron pnictide superconductors. Furthermore, the interplay between magnetism and superconductivity at the single layer limit in iron chalcogenides also remains largely unexplored.

In this dissertation, I report on scanning tunneling microscopy/spectroscopy (STM/S) studies of single layer FeSe films grown on STO substrates using molecular beam epitaxy (MBE), focusing on the aspects discussed above. By mapping the spatially resolved superconducting gaps near the edges of single layer FeSe as a function of the edge orientations, I obtain evidence for sign-changing d wave pairing symmetry in single layer FeSe/STO. By further synthesizing well-defined rectangular nanoribbons with precisely controlled width, I establish the lowest length limit for superconducting single layer FeSe nanoribbons. To investigate the interplay between magnetism and superconductivity, I prepared single layer $\text{FeTe}_{1-x}\text{Se}_x$ films with different Se concentrations. A one-dimensional superconducting channel is observed on the edge of magnetically ordered single layer $\text{FeTe}_{1-x}\text{Se}_x$ films with Se concentration below 10%. This result suggests that the edge of the $\text{FeTe}_{1-x}\text{Se}_x$ ($x < 0.1$) film may help to destabilize the antiferromagnetic ordering and induce superconductivity. To identify the role of the interface, I prepared STO substrates with coexisting TiO_2 and SrO terminations for the FeSe growth, and found that the superconducting gap of single layer FeSe grown on SrO is $\sim 30\%$ smaller than that on TiO_2 , confirming the critical role of the TiO_2 termination in enhancing superconductivity. Those findings contribute significantly to the understanding of enhanced superconductivity in the FeSe/STO system, providing crucial insights into the design of interfacial control of superconductivity in the iron chalcogenide/oxide system.

TABLE OF CONTENTS

Chapter 1 Introduction	1
1.1 Conventional Superconductors	1
1.1.1 The Basic Phenomena	1
1.1.2 Bardeen-Cooper-Schrieffer Theory	4
1.2 Single Layer FeSe on SrTiO ₃	12
1.2.1 Iron-based Superconductors	12
1.2.2 Interface Superconductivity in Single Layer FeSe on SrTiO ₃	14
1.2.3 Structural and Electronic Properties	16
1.2.4 Mechanisms for T_c Enhancement	19
1.3 Dissertation Outline	22
Chapter 2 Experimental Techniques	29
2.1 Ultrahigh Vacuum System	29
2.2 Molecular Beam Epitaxy	32
2.3 Scanning Tunneling Microscopy	35
2.3.1 An Elementary Model – One-dimensional Potential Barrier	36
2.3.2 Bardeen’s Approach	40
2.3.3 Tersoff-Hamann Model	44
2.3.4 Operation Modes	47
2.4 Home-build MBE-STM System	48
Chapter 3 Nodeless d -wave Superconductivity in Single Layer FeSe/SrTiO ₃ Probed by Quasiparticle Scattering off Step Edges	51
3.1 Introduction	51
3.2 Results and Discussion	55
3.3 Summary	70
Chapter 4 Width-dependent Suppression of Superconductivity in Single Layer FeSe Nanoribbons	74
4.1 Introduction	74
4.2 Results and Discussion	75
4.3 Summary	83
Chapter 5 Superconductivity on Edge: One-dimensional Superconducting Channel on the Edge of Antiferromagnetic Single Layer FeTeSe Nanoribbons	85
5.1 Introduction	85

5.2 Results and Discussion.....	86
5.3 Summary	102
Chapter 6 Summary and Outlook.....	106
6.1 Summary	106
6.2 Outlook.....	108
6.2.1 Interface Engineering	108
6.2.2 Local Superconducting-like Pairing	110
CURRICULUM VITAE.....	113

LIST OF FIGURES

Figure 1.1 Zero resistivity and Meissner effect

Figure 1.2 Schematic of the formation of a Cooper pair

Figure 1.3 Experimental verifications of the BCS theory

Figure 1.4 Timeline of superconductors

Figure 1.5 The five classes of iron-based superconductors

Figure 1.6 Structure, STM image and STS on single layer and bilayer FeSe/STO

Figure 1.7 Crystal structure and Brillouin zone of single layer FeSe

Figure 1.8 2x1 ordering in single layer FeSe/STO and double TiO_x interface structure

Figure 1.9 Fermi surface of single layer FeSe and bulk (Ba_{0.6}K_{0.4})Fe₂As₂

Figure 1.10 Replica bands in single layer FeSe/STO

Figure 2.1 Relationship of several concepts defining the degree of vacuum

Figure 2.2 Pictures and schematics of different pumps and ion gauge

Figure 2.3 Picture and schematic of MBE growth

Figure 2.4 Picture and schematic of a Knudsen cell

Figure 2.5 Setup of STM and schematic of constant current mode scanning

Figure 2.6 Schematic of wavefunction tunneling through a one-dimensional potential barrier

Figure 2.7 Schematic of the Bardeen's approach

Figure 2.8 Schematic of the sample-tip tunneling process

Figure 2.9 Schematic of the TH model

Figure 2.10 Pictures of the home-built MBE-STM system

Figure 2.11 Illustration of STM tip cutting and etching, and images of cut and etched tips

Figure 3.1 Extrapolation length and pairing symmetries

Figure 3.2 Scattering at a specular edge of different pairing symmetries

Figure 3.3 Single layer FeSe films with $[110]_{\text{Fe}}$ and $[010]_{\text{Fe}}$ edges

Figure 3.4 As-grown FeSe film and the specular $[110]_{\text{Fe}}$ and the rough $[010]_{\text{Fe}}$ edges

Figure 3.5 Superconductivity in the annealed FeSe films

Figure 3.6 ARPES measurement of single layer FeSe

Figure 3.7 dI/dV spectra on the specular FeSe $[110]_{\text{Fe}}$ and $[010]_{\text{Fe}}$ edges

Figure 3.8 Normalization of the superconducting dI/dV spectrum

Figure 3.9 Uniform superconducting gaps parallel to the specular FeSe $[110]_{\text{Fe}}$ edge

Figure 3.10 Extrapolation length on the specular FeSe #1 $[110]_{\text{Fe}}$ grain boundary

Figure 3.11 Extrapolation length on the specular FeSe #2 $[110]_{\text{Fe}}$ FeSe-to-STO edge

Figure 3.12 Extrapolation length on the rough FeSe $[010]_{\text{Fe}}$ edge

Figure 3.13 In-gap states on specular FeSe $[110]_{\text{Fe}}$ and $[010]_{\text{Fe}}$ edges

Figure 3.14 In-gap states on rough FeSe $[010]_{\text{Fe}}$ edges

Figure 4.1 STM images and STS on single layer FeSe

Figure 4.2 STS on single layer FeSe ribbons of different widths

Figure 4.3 STS on a single layer FeSe ribbon with changing width

Figure 4.4 Size-dependent suppression of superconductivity in single layer FeSe ribbons

Figure 4.5 Quantum well states in STS and DFT calculation of FeSe nanoribbons

Figure 4.5 Schematic of edge scattering in different ribbons under d wave pairing

Figure 5.1 Growth and annealing of single layer $\text{FeTe}_{1-x}\text{Se}_x$ ($x < 0.1$)

Figure 5.2 STM and STS of four single layer $\text{FeTe}_{1-x}\text{Se}_x$ ($0 \leq x \leq 0.1$)

Figure 5.3 ARPES measurement of four single layer $\text{FeTe}_{1-x}\text{Se}_x$ ($0 \leq x \leq 0.1$)

Figure 5.4 One-dimensional edge channel in single layer $\text{FeTe}_{1-x}\text{Se}_x$ ($x < 0.1$)

Figure 5.5 Setpoint dependent imaging of the ribbon edge

Figure 5.6 Bias dependent imaging of the ribbon edges

Figure 5.7 One-dimensional edge superconductivity in single layer $\text{FeTe}_{1-x}\text{Se}_x$ ($x < 0.1$)

Figure 5.8 Normalization of the dI/dV spectra

Figure 5.9 Ribbon width dependence of the edge superconductivity

Figure 5.10 DFT of single layer $\text{FeTe}_{1-x}\text{Se}_x$ with different Se levels and magnetic orderings

Figure 5.11 Simulated STM image with 2×1 ordering and spin defects

Figure 5.12 Simulated STM and STS with 2×1 ordering parallel to the edge

Figure 5.13 Simulated STM and STS with 2x1 ordering perpendicular to the edge

Figure 6.1 Images of STO with TiO₂ and SrO terminations

Figure 6.2 Superconducting gaps of FeSe/TiO₂ and FeSe/SrO

Figure 6.3 Local pairing at extended defects on bilayer FeSe/STO

LIST OF ABBREVIATIONS

1D	One-dimensional
1 Fe UC	One-iron unit cell
1 Fe BZ	One-iron Brillouin zone
2D	Two-dimensional
2 Fe UC	Two-iron unit cell
2 Fe BZ	Two-iron Brillouin zone
3D	Three-dimensional
AFM	Antiferromagnetic
ARPES	Angle-resolved photoemission spectroscopy
BCL	Bicollinear
BZ	Brillouin zone
CB	Checkerboard
DFT	Density functional theory
dI/dV	Differential tunneling conductance
DOS	Density of states
FeSC	Iron-based superconductor
MBE	Molecular beam epitaxy

SOC	Spin-orbit coupling
STM	Scanning tunneling microscopy
STO	SrTiO ₃
STS	Scanning tunneling spectroscopy
TEM	Transmission electron microscopy
TH	Tersoff-Hamann
UHV	Ultra-high vacuum

ACKNOWLEDGMENTS

Without the help from numbers of people around me, this dissertation could not have been finished. First of all, I would like to thank my parents for their constant and unconditional support which helps me through the ups and downs of my life for these years. And special thanks to my dearest girlfriend, Yiran Tong, who is my light leading me through the obstacles in my path.

Thanks to all my past and present labmates: Shivani Rajput, Dushyant Tomer, Yaoyi Li, Xi Dong, Lawrence Hudy, Chenhui Yan, Liwei Liu, Huimin Zhang and Rusty Mundorf. They are my great friends in life, and they help me to resolve technical issues and discuss with me about physical problems during my research.

Thanks to all the teachers in the physics department of the University of Wisconsin Milwaukee for their professional education. Thanks to the graduate program assistant, Kate Valerius, for her patience in dealing with my all kinds of documents. Thanks to Michael Condon in the machine shop for making the parts to build our instrument.

Thanks to Peter Schwander and Jorg Woehl for their willingness to serve as my graduation committee members. Thanks to Daniel Agterberg for providing theoretical insights underlying our experimental discoveries. A special thanks to Michael Weinert, not only for his patience in explaining simple concepts, but also for his willingness to be my advisor at Milwaukee after I moved to Morgantown.

Finally, I would like to express my greatest gratitude to my advisor Lian Li for helping me understand how to achieve the goals both in my research career and daily life. I have always benefited from his scientific expertise in our field, and more importantly it is rewarding to learn

from his way of critical thinking and communicating. All the stories he shared with us pushed me closer and closer to becoming a qualified researcher. Particularly for me, his patience and willingness to listen have helped me overcome again and again the challenges during my graduate school time.

Chapter 1 Introduction

Superconductivity has been an active field of research since its discovery. Recently, the investigation on the newly discovered iron-based superconductors (FeSCs) family, especially single layer iron selenide on strontium titanate, significantly improves our understanding of this intriguing phenomenon. Section 1.1 introduces conventional superconductors, and the Bardeen-Cooper-Schrieffer theory of superconductivity. Section 1.2 summarizes recent work on epitaxial single layer iron selenide (FeSe) on strontium titanate (SrTiO_3) (001). Section 1.3 is the outline of the dissertation.

1.1 Conventional Superconductors

1.1.1 The Basic Phenomena

The phenomenon of superconductivity was first observed in mercury by Dutch physicist Heike Kamerlingh Onnes in 1911¹, just 3 years after he had first liquefied helium, which gave him the refrigeration technique to reach temperatures of a few degrees Kelvin. When he cooled mercury to the temperature of liquid helium, its resistance suddenly dropped to zero (Fig. 1.1a). The disappearance of electrical resistance below a critical temperature T_c , also known as perfect conductivity, is the first hallmark of superconductivity. This infinite conductivity implies that if a current were passed through a superconductor, the current would follow forever without any dissipation.

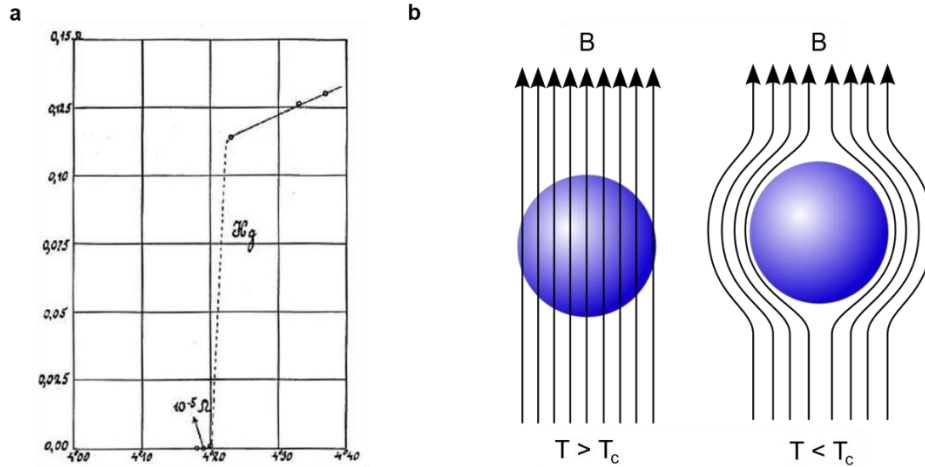


Figure 1.1 a, Zero resistivity below the critical temperature in Hg¹. **b**, Schematic of the Meissner effect².

The next hallmark to be discovered was perfect diamagnetism (Fig. 1.1b), found in 1933 by Meissner and Ochsenfeld³. They found that not only a magnetic field is excluded from entering a superconductor, but also that a field in an originally normal sample is expelled when dropping the temperature through T_c . The existence of such a reversible Meissner effect implies that superconductivity will be destroyed by a critical magnetic field H_c .

The perfect diamagnetism is more fundamental for a superconductor than the perfect conductivity. For a perfect conductor, the superconducting current density in an electric field \vec{E} is given by

$$\dot{\vec{J}}_s = \frac{n_s e^2}{m} \vec{E} \quad (1.1)$$

where n_s is the number density of superconducting electrons. Plugging into Faraday equation gives

$$\nabla \times \frac{\partial \vec{J}_s}{\partial t} = -\frac{n_s e^2}{cm} \frac{\partial \vec{B}}{\partial t} \quad (1.2)$$

From Ampere law

$$\nabla \times \vec{B} = \frac{4\pi}{c} \vec{J}_s \quad (1.3)$$

we obtain

$$\nabla \times \nabla \times \frac{\partial \vec{B}}{\partial t} = -\frac{4\pi n_s e^2}{mc^2} \frac{\partial \vec{B}}{\partial t} \quad (1.4)$$

Applying the identity $\nabla \times \nabla \times \vec{C} = \nabla(\nabla \cdot \vec{C}) - \nabla^2 \vec{C}$ and Gauss's law $\nabla \cdot \vec{B} = 0$, we have

$$\nabla^2 \left(\frac{\partial \vec{B}}{\partial t} \right) = \lambda^{-2} \left(\frac{\partial \vec{B}}{\partial t} \right) \quad (1.5)$$

where

$$\lambda = \sqrt{\frac{mc^2}{4\pi n_s e^2}} \quad (1.6)$$

Solving the differential equation (1.5) in x direction, we get an exponential decay of $\partial \vec{B} / \partial t$ with x ,

$$\frac{\partial \vec{B}}{\partial t} = \left(\frac{\partial \vec{B}}{\partial t} \right)_{x=0} e^{-x/\lambda} \quad (1.7)$$

This equation indicates the magnetic field inside a perfect conductor is constant (no change with time). However, considering a superconductor, with a magnetic field \vec{B}_0 applied above T_c . If we cool down the system below T_c , the Meissner effect says the magnetic field inside the superconductor will vanish to zero, rather than remain \vec{B}_0 for a perfect conductor. This tells us that a superconductor is more than a perfect conductor due to the Meissner effect.

1.1.2 Bardeen-Cooper-Schrieffer Theory

After the experimental discovery of superconductivity, tremendous effort has been put in search of a microscopic theory. In 1935, brothers Fritz and Heinz London developed the London equations to describe the magnetic field penetration length⁴. Although qualitatively describing well the perfect conductivity and perfect diamagnetism, the London equations overestimated the experimental measurements. The Ginzburg-Landau theory in 1950, was a phenomenological theory using the variational principle of quantum mechanics⁵. It was used to calculate macroscopic quantities of a superconductor assuming the phase transition to be of second order. However, it did not explain the foundation of superconductivity. It was not until almost half a century after the discovery of superconductivity, at 1957, that the first microscopic theory, describing the conceptual and mathematical foundation for conventional superconductivity, was established by Bardeen, Cooper and Schrieffer⁶.

The Bardeen-Cooper-Schrieffer (BCS) theory assumes that superconductivity arises when the attractive Cooper pair interaction is formed between electrons. A Cooper pair is an

electron-electron bound state mediated by the exchange of phonons. As demonstrated in Fig. 1.2, an electron (electron 1) moving through a crystal lattice will attract positive ions in the lattice and the lattice will deform slowly in the time scale of the electron. This positive charge of the lattice deformation (phonon) can attract another electron (electron 2) of opposite spin and momentum. Due to the retardation, the electron-electron Coulomb repulsion may be neglected. The net effect of the phonon is to create an attractive interaction between two electrons and form electron-electron Cooper pairs. These Cooper pairs then form a coherent macroscopic condensate ground state, which displays a gapped density of states spectrum and perfect diamagnetism.

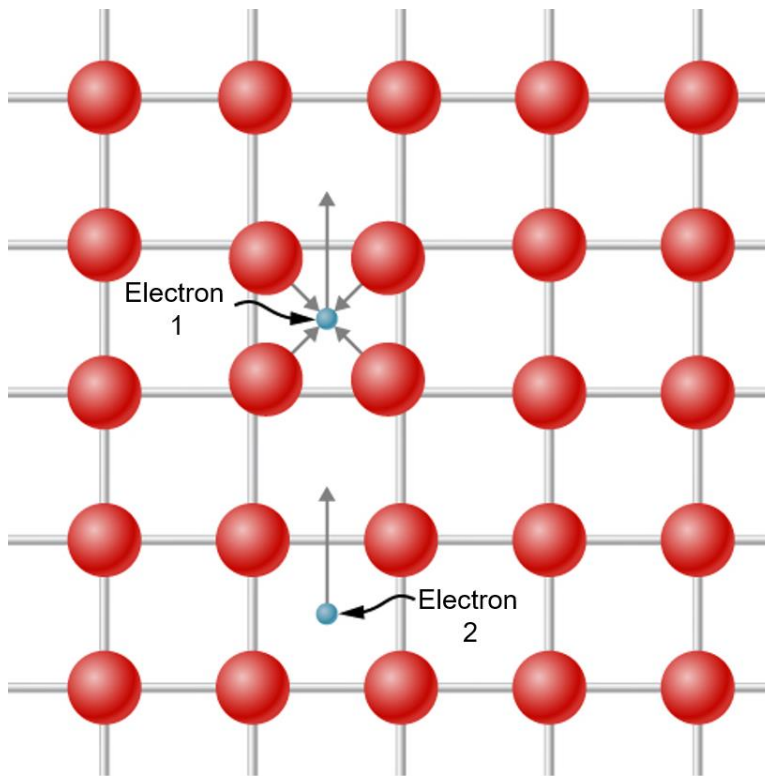


Figure 1.2 Schematic of the formation of a Cooper pair⁷.

The physical foundation of the BCS theory can be illustrated by looking at the formation of a single Cooper pair via attractive interaction. The Schrodinger equation of two electrons m at \vec{r}_1 and \vec{r}_2 with an attractive potential $V(\vec{r}_1 - \vec{r}_2)$ in the center of mass coordinate system is

$$\left[-\frac{\hbar^2 \nabla_{\vec{R}}^2}{2m^*} - \frac{\hbar^2 \nabla_{\vec{r}}^2}{2\mu} + V(\vec{r}) \right] \psi(\vec{r}, \vec{R}) = E \psi(\vec{r}, \vec{R}) \quad (1.8)$$

where $\vec{R} = \frac{1}{2}(\vec{r}_1 - \vec{r}_2)$ is the center of mass, $\vec{r} = \vec{r}_1 - \vec{r}_2$ is the relative displacement, $m^* = 2m$ is the total mass and $\mu = m/2$ is the reduced mass. Separating the variables as $V(\vec{r})$ is independent of \vec{R} , the solution can be written as

$$\psi(\vec{r}, \vec{R}) = \phi(\vec{r}) e^{i\vec{K} \cdot \vec{R}} \quad (1.9)$$

where \vec{K} is the momentum of the center of mass. Then we have

$$\left[-\frac{\hbar^2 \nabla_{\vec{r}}^2}{2\mu} + V(\vec{r}) \right] \phi(\vec{r}) = \tilde{E} \phi(\vec{r}) \quad (1.10)$$

where $\tilde{E} = E - \frac{\hbar^2 K^2}{2m^*}$. The system has the lowest energy E when $\vec{K} = 0$ (the two electrons have opposite momenta). Hence, we consider $E = \tilde{E}$ for the following.

Converting the Schrodinger equation to the momentum space by Fourier transform, we have

$$\int d^3r V(\vec{r}) \phi(\vec{r}) e^{-i\vec{k} \cdot \vec{r}} = \left(E - \frac{\hbar^2 k^2}{m} \right) \phi(\vec{k}) \quad (1.11)$$

Defining the scattering vector $\vec{q} = \vec{k} - \vec{k}'$ and free electron energy $\varepsilon_k = \frac{\hbar^2 k^2}{2m}$, then we have

$$\int \frac{d^3 k'}{(2\pi)^3} V(\vec{q}) \phi(\vec{k}') = (E - 2\varepsilon_k) \phi(\vec{k}) \quad (1.12)$$

where $V(\vec{q}) = \int d^3 r V(\vec{r}) e^{-i\vec{q}\cdot\vec{r}}$. It gives

$$\Delta(\vec{k}) = - \int \frac{d^3 k'}{(2\pi)^3} \frac{V(\vec{k} - \vec{k}')}{2\varepsilon_{k'} - E} \Delta(\vec{k}') \quad (1.13)$$

where $\Delta(\vec{k}) = (E - 2\varepsilon_k) \phi(\vec{k})$ is the modified wavefunction.

Taking the mean field approximation, considering an attractive potential within the Debye window

$$V(\vec{k} - \vec{k}') = \begin{cases} -V_0 & \text{for } 0 < \varepsilon_k, \varepsilon_{k'} < \hbar\omega_D \\ 0 & \text{otherwise} \end{cases} \quad (1.14)$$

where ω_D is the Debye frequency. Here we look for a solution with constant $\Delta(\vec{k}) = \Delta$ within the BCS theory. This implies an even spatial wavefunction and the spins of the two electrons must be opposite. Using the identity

$$\int g(\varepsilon) d\varepsilon = \int \frac{d^3 k}{(2\pi)^3} \quad (1.15)$$

where $g(\varepsilon) = \frac{\sqrt{2}m^{3/2}}{\hbar^3 \pi^2} \sqrt{\varepsilon}$ is the density of states (note that we do not have the spin factor of 2

because the spins of the two electrons are antiparallel), equation (1.13) becomes

$$\Delta = \int_0^{\hbar\omega_D} g(\varepsilon) d\varepsilon \frac{V_0\Delta}{2\varepsilon - E} \quad (1.16)$$

which gives

$$1 = \frac{\sqrt{2}V_0m^{3/2}}{\hbar^3\pi^2} \left[\sqrt{\hbar\omega_D} - \sqrt{\frac{-E}{2}} \tan^{-1} \left(\sqrt{\frac{2\hbar\omega_D}{-E}} \right) \right] \quad (1.17)$$

The minimum value of V_0 for a bound state ($E \rightarrow 0^-$) is

$$V_{0,min} = \frac{\hbar^{5/2}\pi^2}{m^{3/2}\sqrt{2\omega_D}} \quad (1.18)$$

This implies that we need a minimum strength of attractive interaction to form a Cooper pair.

However, in the actual material, only the electrons near the Fermi level will be affected by the attractive interaction. We then consider another attractive potential for the electrons above the Fermi level

$$V(\vec{k} - \vec{k}') = \begin{cases} -V_0 & \text{for } \varepsilon_F < \varepsilon_k, \varepsilon_{k'} < \varepsilon_F + \hbar\omega_D \\ 0 & \text{otherwise} \end{cases} \quad (1.19)$$

then equation (1.13) becomes

$$\Delta = \int_{\varepsilon_F}^{\varepsilon_F + \hbar\omega_D} g(\varepsilon) d\varepsilon \frac{V_0\Delta}{2\varepsilon - E} \quad (1.20)$$

Approximating constant density of states near ε_F within the Debye window, equation (1.20)

becomes

$$\frac{2}{V_0 g(\varepsilon_F)} = \ln \left(\frac{2\varepsilon_F - E + 2\hbar\omega_D}{2\varepsilon_F - E} \right) \quad (1.21)$$

Defining the binding energy E_b

$$E_b \equiv 2\varepsilon_F - E = \frac{2\hbar\omega_D}{e^{2/V_0 g(\varepsilon_F)} - 1} \approx 2\hbar\omega_D e^{-2/V_0 g(\varepsilon_F)} > 0 \quad (1.22)$$

Here, a two-electron bound state will be formed ($E < 2\varepsilon_F$) near the Fermi level no matter how small the attractive interaction V_0 is. Comparing with the free electron case where a minimum attractive potential is required, it indicates that the existence of a well-defined Fermi surface is key to the formation of Cooper pairs.

The weak phonon-mediated attractive interaction is sufficient to destabilize the Fermi sea and promote the formation of a Cooper pair ($\vec{k} \uparrow, -\vec{k} \downarrow$). Many electrons can participate in this process and many Cooper pairs are formed, yielding a new state, the superconducting phase, of the system.

For a superconducting system, the modified wavefunction $\Delta(\vec{k})$ is given by (similar to equation (1.13))

$$\Delta(\vec{k}) = - \sum_{\vec{k}'} \frac{V(\vec{k} - \vec{k}') \Delta(\vec{k}')}{2E_{k'}} \tanh \left(\frac{E_{k'}}{2k_B T} \right) \quad (1.23)$$

where $E_k = \sqrt{\xi_k^2 + \Delta(\vec{k})^2}$ and $\xi_k = \varepsilon_k - \varepsilon_F$. $\Delta(\vec{k})$ is also called the gap function, because even at the Fermi level, the energy spectrum of a superconductor has a gap of size $|\Delta(\vec{k})|$. In general, the gap function $\Delta(\vec{k})$ depends on \vec{k} . With different symmetries of the gap function, we can define superconductors of different pairing symmetries, e.g. *s* wave superconductors with constant $\Delta(\vec{k}) = \Delta$ and *d* wave superconductors where $\Delta(\vec{k})$ changes sign for every rotation by $\pi/2$. Within the BCS theory, all conventional superconductors are *s* wave pairing. The excitation energy, which is the minimum energy to break a Cooper pair, is $\Delta E_{min} = 2\Delta$. Again, taking the mean field approximation, we obtain

$$1 = V_0 g(\varepsilon_F) \int_0^{\hbar\omega_D} \frac{d\xi}{\sqrt{\xi^2 + \Delta^2}} \tanh\left(\frac{\sqrt{\xi^2 + \Delta^2}}{2k_B T}\right) \quad (1.24)$$

At temperature $T = 0$

$$\Delta_0 \equiv \Delta(T = 0) \approx 2\hbar\omega_D e^{-1/V_0 g(\varepsilon_F)} \quad (1.25)$$

The critical temperature T_c is where a non-zero gap first appears. Setting $\Delta \rightarrow 0$, we have

$$T_c = 1.14 \frac{\hbar\omega_D}{k_B} e^{-1/V_0 g(\varepsilon_F)} \quad (1.26)$$

Combining equations (1.25) and (1.26) gives the universal ratio for conventional superconductors

$$\frac{\Delta_0}{k_B T_c} \approx 1.76 \quad (1.27)$$

According to the BCS theory, conventional superconductors are characterized by two important properties, the presence of the energy gap Δ and the involvement of phonons. The energy gap is manifest in the low temperature specific heat and density of states measurements.

For a fermionic gas the specific heat $C = \frac{T}{V} \frac{dS}{dT}$ can be calculated from the entropy

$$S = -k_B \sum_k [(1 - f_k) \ln(1 - f_k) + f_k \ln f_k] \quad (1.28)$$

where $f_k = 1/(1 + e^{E_k/k_B T})$ is the Fermi-Dirac distribution. At the superconducting transition temperature, the specific heat is discontinuous

$$\Delta C = C_s - C_n = -g(\varepsilon_F) \left(\frac{d\Delta^2}{dT} \right)_{T=T_c} \quad (1.29)$$

This is demonstrated by the heat capacities of superconducting aluminum in Fig. 1.3a⁸. In the scanning tunneling spectroscopy measurement, the gap in the density of states of superconducting NbS₂ is directly shown in Fig. 1.3b⁹. From equation (1.31), the transition temperature depends linearly on the Debye frequency, which is proportional to the inverse square root of the ionic mass, i.e. $T_c \sim \omega_D \sim M^{-1/2}$. This leads to the isotope effect that the superconducting transition temperature varies with the isotopic mass, which has been observed in mercury (Fig. 1.3c)^{10,11}.

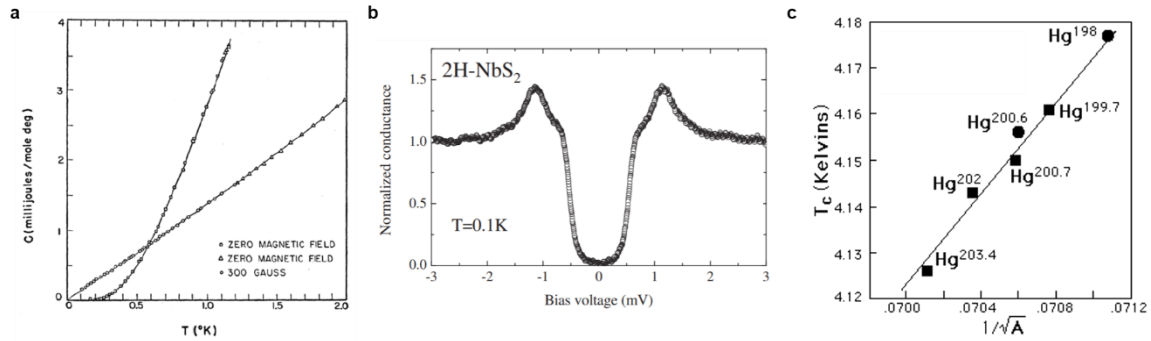


Figure 1.3 **a**, Heat capacities of Al at the normal phase (linear) and the superconducting phase (nonlinear)⁸. **b**, STS spectrum taken on superconducting NbS_2 at 0.1 K⁹. **c**, Superconducting transition temperature of Hg as a function of isotope mass¹².

1.2 Single Layer FeSe on $SrTiO_3$

1.2.1 Iron-based Superconductors

About three decades after the BCS theory was established, cuprate superconductors are discovered with T_c up to 153 K^{13,14}, which breaks the McMillian limit of 40 K of conventional superconductors. The discovery of cuprates starts a new chapter, unconventional superconductivity (or high temperature superconductivity), in the research history of superconducting science. Different from the conventional BCS superconductors, unconventional superconductors have higher T_c , which potentially can reach room temperature, and the unconventional Cooper pairs are not mediated by phonons¹⁵. Physicists have been looking for various unconventional superconductors with higher T_c experimentally (Fig. 1.4) and trying to establish a microscopic theory for unconventional electron-electron pairing theoretically.

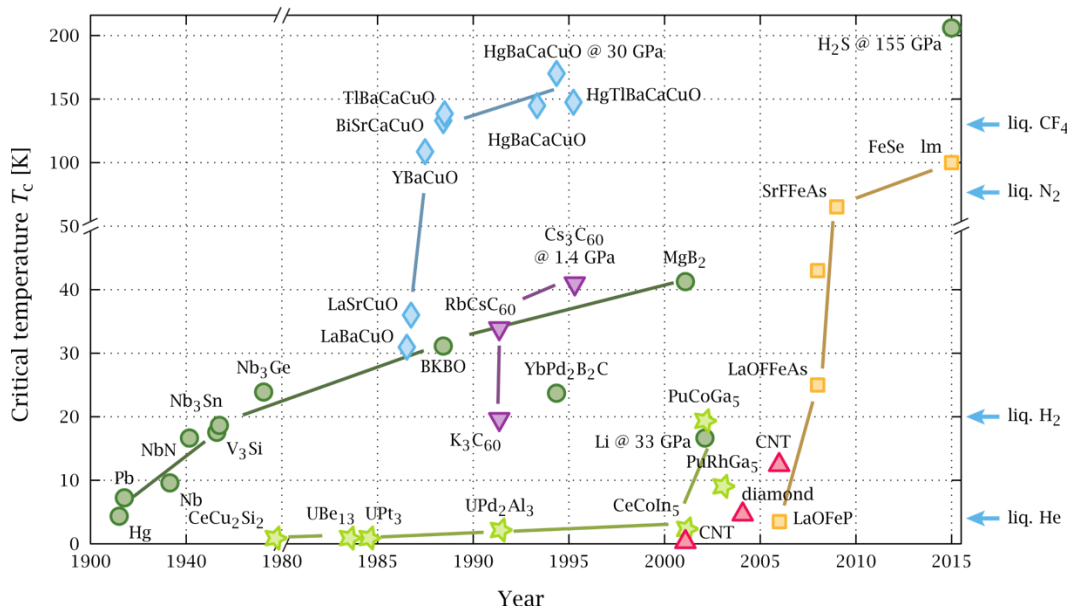


Figure 1.4 Timeline of superconductors¹⁶.

In 2008, superconductivity at 26 K in LaOFeAs with primitive tetragonal structure was reported by Hosono's group¹⁷. This is not the first report of superconducting compounds containing iron¹⁸, but it is the cutting-edge work which leads to the build-up of the iron-based superconductors (FeSCs) family. Almost immediately after the LaOFeAs, higher T_c of ~ 56 K was observed in other iron compounds via doping with different rare-earth ions¹⁹⁻²¹. With the discovery of more and more iron-containing superconductors by playing with the chemical pressure and physical pressure, the high temperature FeSCs family with two branches of the iron pnictides (FePn, where Pn is As or P) and the iron chalcogenides (FeCh, where Ch is S, Se or Te) is established^{22,23}. In addition to the potential of finding higher T_c materials, FeSCs are underlyingly interesting because it implies that the high temperature superconducting pairing mechanism could be related to the coexistent magnetism due to the presence of iron in the phase diagram²⁴.

There are five classes of iron-based superconducting compounds, all with tetragonal structures at room temperature²² (Fig. 1.5). All these compounds share a common quasi-two-dimensional layer consisting of a square lattice of iron atoms tetragonally connected with pnictide or chalcogenide atoms. It is widely accepted this common FePn/Ch trilayer is critical to support high temperature superconductivity in FeSCs^{22,23}. Hence the 11-type iron chalcogenide (FeS, FeSe and FeTe), which has the simplest crystal structure among FeSCs, is a key system to investigate the mechanism of iron-based superconductivity²⁵.

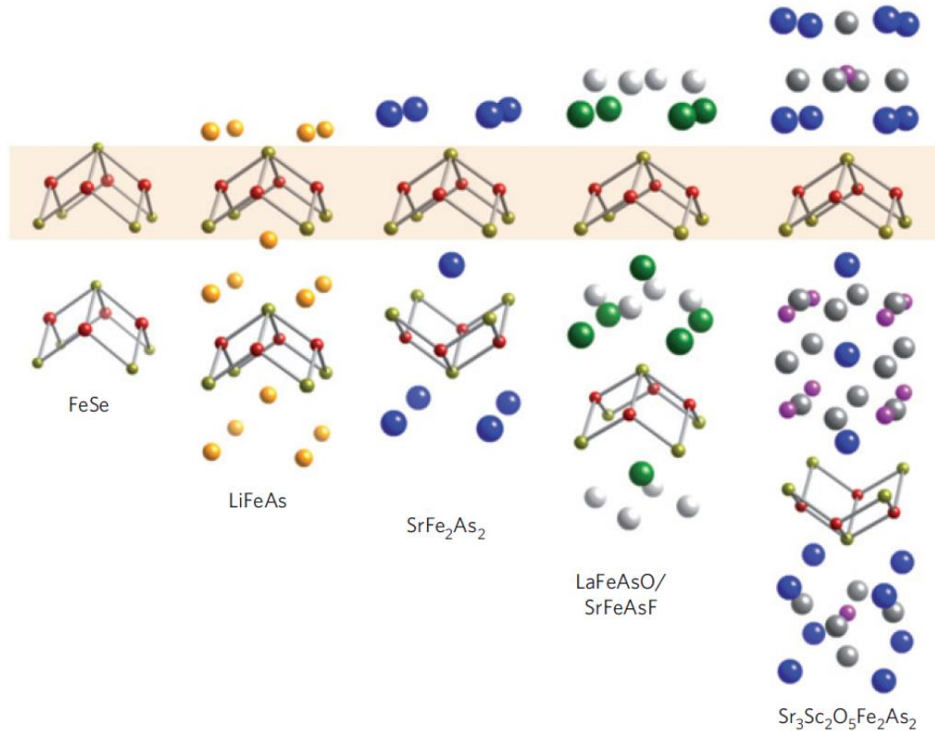


Figure 1.5 The five classes of FeSCs²².

1.2.2 Interface Superconductivity in Single Layer FeSe on SrTiO₃

FeSe is an ideal material to investigate iron-based superconductivity. The tetragonal phase α -FeSe with PbO structure (space group: $P4/nmm$) exhibits bulk superconductivity at 8

K²⁶. This T_c can be increased by applying pressure^{27,28}, intercalating alkali metal atoms²⁹⁻³¹ or electrical gating^{32,33}. More surprisingly, in 2012, scanning tunneling microscopy (STM) measurements from Xue's group revealed a superconducting-like gap up to 20 meV in single layer FeSe films grown on SrTiO₃(001) (STO) substrates by molecular beam epitaxy³⁴ (MBE) (Fig. 1.6), suggesting dramatically enhanced superconductivity in this heterostructure. Considering the 2.2 meV gap of bulk FeSe crystal³⁵ and assuming the same ratio between the superconducting gap and the transition temperature, the T_c of single layer FeSe/STO would be estimated of ~ 80 K. Another *in situ* transport study reported a transition temperature even above 100 K³⁶, indicating that single layer FeSe/STO has the highest T_c among all FeSCs. As a comparison, MBE grown single layer FeSe on bilayer graphene does not exhibit superconductivity cooled down to as low as 2.2 K³⁷. It suggests that the STO substrate is critical to the T_c enhancement.

Ex situ electrical transport and diamagnetic measurements have also been conducted to confirm the high-temperature superconducting nature of single layer FeSe/STO³⁸. However, the T_c by *ex situ* measurement is not as high as expected from the *in situ* STM³⁴ or angle-resolved photoemission spectroscopy³⁹ (ARPES) measurements. In *ex situ* measurements, the single layer FeSe films are always capped by multiple FeTe protection layers to prevent direct air exposure. This FeTe capping layer could reduce the charge doping level in the FeSe films. What's more, the magnetic structure of FeTe⁴⁰ is different from the FeSe layer⁴¹, and this difference may have a negative influence on superconductivity. Therefore, *in situ* techniques are preferred for investigation on single layer FeSe/STO.

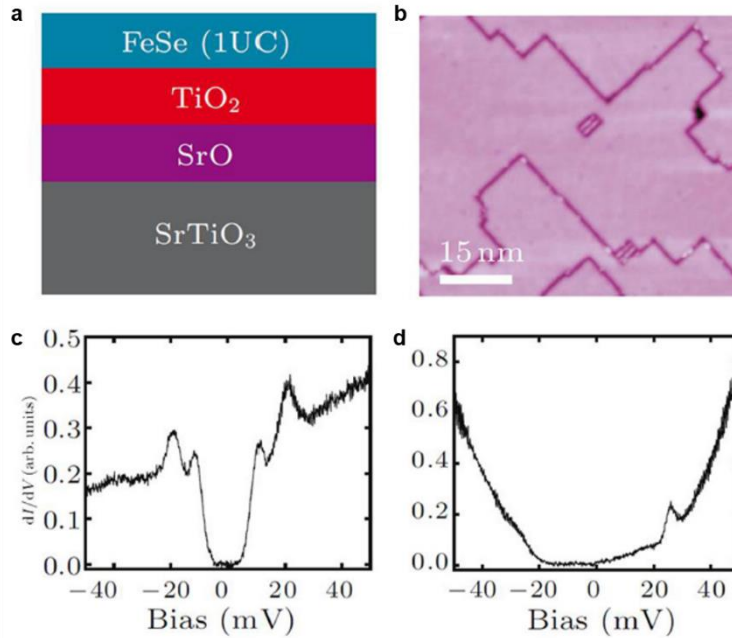


Figure 1.6 **a**, Structure (side view) of single layer FeSe/STO system³⁴. **b**, STM image of single layer FeSe/STO. The dark contrast lines are grain boundaries³⁴. **c**, dI/dV spectrum taken on single layer FeSe/STO at 4.2 K, with a superconducting-like gap³⁴. **d**, dI/dV spectrum taken on bilayer FeSe/STO at 4.2 K, with a semiconducting-like behavior³⁴.

1.2.3 Structural and Electronic Properties

The crystal structure of single layer FeSe is shown in Fig. 1.7a. Each Fe atom is tetragonally connected with four Se atoms, among which two of the Se atoms are above the Fe plane and the other two Se atoms are below the Fe plane. Due to this staggering, the primitive unit cell contains two Fe atoms, referred to as two iron unit cell (2 Fe UC). However, because the electrons contributing to the superconductivity in FeSe are dominantly from the Fe 3d orbitals, one may neglect the Se layers and focus on the Fe plane, where one iron unit cell (1 Fe UC) is used. The corresponding one iron and two iron Brillouin zones (BZ) are shown in Fig. 1.7b.

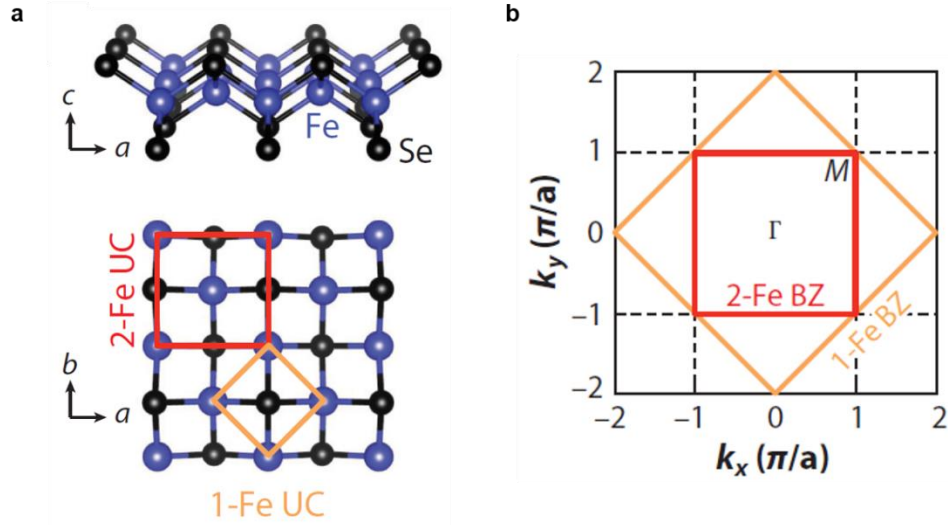


Figure 1.7 a, Crystal structure of single layer FeSe. The upper is side view and the lower is top view. Both one iron unit cell and two iron unit cell are illustrated⁴². **b**, One iron and two iron Brillouin zones in the momentum space⁴².

The interface structure between FeSe and STO could be complicated based on several experimental indications. The first indication is the 2x1 ordering in single layer FeSe/STO from STM topographic images^{34,43} (Fig. 1.8a), which is unexpected because both the FeSe and the STO crystal have 4-fold symmetry. Note that this 2x1 ordering has not been universally observed⁴⁴. A more direct evidence of the complex interface structure comes from transmission electron microscopy (TEM) measurements, as shown in Fig. 1.8b, where a double TiO_x termination was imaged at the interface⁴⁵. This double TiO_x structure was also resolved from X-ray diffraction and electron diffraction experiments⁴⁶. The extra TiO_x termination could impact superconductivity in FeSe by facilitating the charge transfer from the STO oxygen vacancies⁴⁶, modifying the electrostatic potential⁴⁷ or changing the magnetic properties⁴⁸.

The Fermi surface and band structure of single layer FeSe/STO were revealed by ARPES measurements^{39,49,50}, as shown in Fig. 1.9a. Only electron pockets at the BZ corners (*M* points)

were observed, while no Fermi surface is present at the BZ center (Γ point). This type of Fermi surface is similar to that of alkali metal doped FeSe⁵¹. Compared with the Fermi surface of bulk FeSe^{52,53}, which has a hole pocket at the Γ point, as well as electron pockets at M points, the corresponding hole pocket at the Γ point sinks ~ 80 meV below the Fermi level in single layer FeSe/STO (Fig. 1.9b). Measuring the size of the electron pocket at the Γ point yields a carrier density of 0.1 electrons per iron atom, indicating the single layer FeSe film is electron doped.

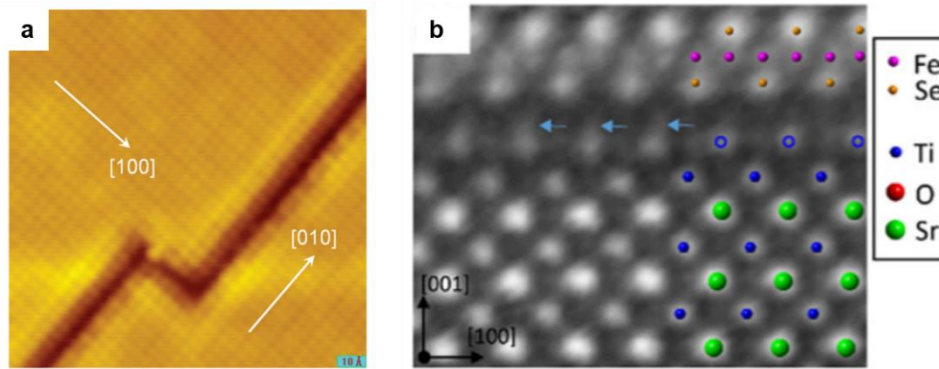


Figure 1.8 a, STM image of single layer FeSe with two grains. The left grain has 2x1 ordering along the [100] direction and the right grain has 2x1 ordering along the [010] direction⁴³. **b**, TEM image of single layer FeSe on STO, revealing a double TiO_x structure⁴⁵.

In unconventional superconductors, Cooper pairs are usually formed via quantum fluctuations, other than phonons in the case of BCS superconductors¹⁵. Considering the nature of the multiband Fermi surface, various pairing symmetries, in addition to s wave with a constant sign, are possible for FeSCs. So far, the most widely accepted scenario for iron pnictides is s_{++} pairing⁵⁴ (Fig. 1.9c), which is mediated by repulsive spin fluctuations from scattering between the electron pockets at the BZ corners and the hole pocket at the BZ center (Fig. 1.9d). However, for single layer FeSe/SrTiO₃, the s_{++} pairing symmetry is inconsistent with the Fermi surface which has only electron pockets and no hole pockets. Taking account of the fully opened gaps by

STM and ARPES measurements, four primary pairing candidates involving only electron pockets are proposed for single layer FeSe/STO: plain s wave⁵⁵⁻⁵⁷, nodeless d wave⁵⁸⁻⁶⁰, bonding-antibonding s wave⁶¹, and incipient s + $-$ wave⁶². More investigations, especially by phase sensitive probes, will help to determine the gap structure.

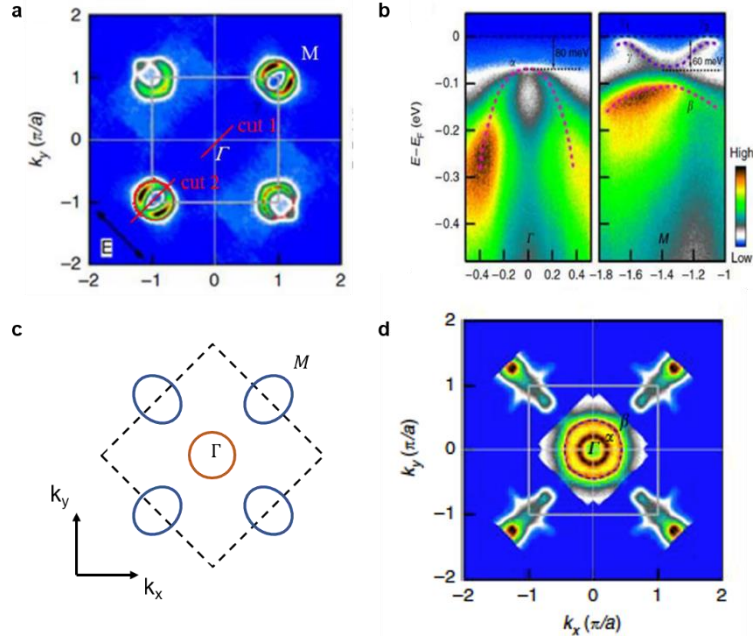


Figure 1.9 **a**, Fermi surface of single layer FeSe/STO at 20 K from ARPES measurement⁴⁹. **b**, Band structure along the cut 1 (left panel) and along the cut 2 (right panel)⁴⁹. **c**, Schematic of sign changing s + $-$ wave pairing. The electron pocket at M is blue and positive, and the hole pocket at Γ is brown and negative. **d**, Fermi surface of $(\text{Ba}_{0.6}\text{K}_{0.4})\text{Fe}_2\text{As}_2$ at 14 K from ARPES measurement⁴⁹.

1.2.4 Mechanisms for T_c Enhancement

After the discovery of enhanced interface superconductivity in single layer FeSe/STO, several factors have been proposed for the T_c enhancement: the tensile strain due to the lattice

mismatch between FeSe and STO, the charge doping from the STO substrate, and the electron-phonon coupling between the electrons in FeSe and the phonons in STO.

The strain is an important factor to tune T_c for FeSCs^{63,64}. The in-plane lattice constant is 3.77 Å for FeSe⁶⁵ and 3.91 Å for SrTiO₃(001)⁶⁶ and there is a 3.7% lattice mismatch. Atomic resolution STM images have shown that the lattice constant of epitaxially grown single layer FeSe films is extended to 3.9 Å⁵⁰, following the lattice constant of the STO substrate, indicating the existence of tensile strain in the FeSe films. To study the role of strain on superconductivity, single layer FeSe films were grown on different substrates with various lattice constants⁶⁷⁻⁶⁹. It turns out that the T_c just fluctuates slightly around 60 to 70 K changing the tensile strain from 0.4% to 6%, showing no rigid dependence on the substrate lattice constant. Therefore, the influence of tensile strain on superconductivity in single layer FeSe/STO is not significant.

Carrier density is another factor that plays a fundamental role in superconductivity. In the BCS model, equation (1.26) shows that the T_c increases with higher density of states at the Fermi level. For iron-based superconductors, the situation is more complicated. The phase diagram of T_c versus the dopant concentration usually exhibits a dome-like shape²². Nevertheless, optimal amount of charge doping can increase the transition temperature. For single layer FeSe/STO, the significant role of charge doping is first revealed by studying the post-annealing process³⁹. The as-grown single layer FeSe/STO always behaves like an insulator and subsequent annealing is necessary to induce superconductivity. During annealing, the electron pockets at the M points gradually sinks and enlarges, indicating the charge carrier (electron) concentration is increased. Hence the emergence of superconductivity is related with the increase of the charge doping level. Another experimental indication is the observation of potassium doping induced superconductivity of ~48 K in three layers of FeSe films on STO⁷⁰. In the FeSe/STO system,

only the single layer FeSe film is superconducting and multilayer FeSe films exhibit semiconducting-like behavior. It is suspected that the charge doping from the STO substrate is dominant in the first layer and the carrier concentration in the upper FeSe layers are too low to support superconductivity. By depositing K atoms on top of trilayer FeSe/STO, the charge concentration in the upper FeSe layers are increased, thus superconductivity is then realized. ARPES results also demonstrate that after K doping the Fermi surface of multilayer FeSe films become similar to that of single layer FeSe, with only electron pockets at the M points⁷⁰. Therefore, charge doping plays an important role for the T_c enhancement in single layer FeSe/STO.

However, the highest T_c of doping induced superconductivity in multilayer FeSe (~ 50 K) is lower than that of single layer FeSe/STO (above 60 K), implying that the STO substrate plays a critical role in boosting the T_c more than providing charge carriers. Interface-enhanced electron-phonon coupling has been suggested as an origin of the dramatic T_c enhancement in single layer FeSe/STO⁷¹⁻⁷³. The experimental evidence first comes from the observation of replica bands in single layer FeSe/STO by high-resolution ARPES measurements⁷⁴. As shown in Fig. 1.10a, the primary bands A and B at the M point have two extra fainter replicas A' and B' with an energy shift of ~ 100 meV. The band offset of ~ 100 meV is identified as the surface phonon mode energy of the Ti-O bonds in the STO substrate⁷¹. The shape of the replica bands is identical to their corresponding main bands. In addition, the replica bands persisted at least to 120 K (Fig. 1.10b), well above the superconducting transition temperature. Moreover, such replica bands only exist in the single layer FeSe film and are absent in thicker films (Fig. 1.10c), indicating an interfacial origin of this feature. For comparison, superconducting T_c of 60 K has also been observed in single layer FeSe grown on TiO₂ substrate, in which the replica bands

were detected as well^{72,75}. However, such high T_c of 60 K has never been reached in any FeSe based system without additional coupling to STO or TiO₂ substrates. The coincidental observation of a high T_c and the replica bands suggests that the coupling between the FeSe electrons and the Ti-O phonons might be responsible for the enhanced superconductivity. Despite all the advances that have been made, further investigations are still needed to uncover the T_c enhancement mystery in single layer FeSe/STO.

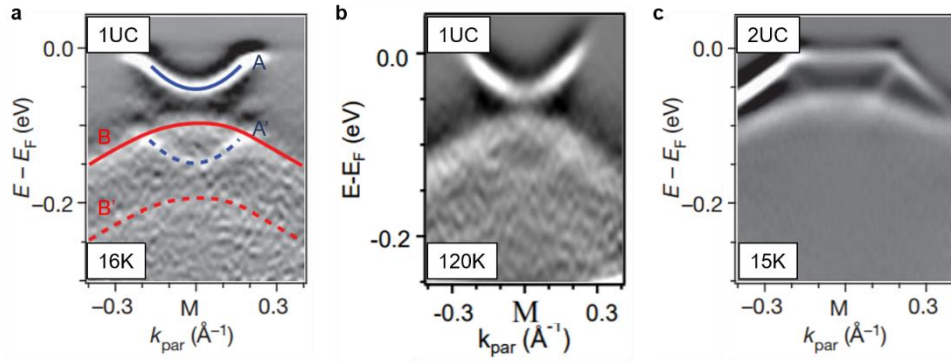


Figure 1.10 a, ARPES measurement of the band structure of single layer FeSe/STO along a high-symmetry cut centered at the M point taken at 16 K, revealing the existence of replica bands⁷⁴. **b**, The replica bands persist in the M cut at 120 K⁷⁴. **c**, The replica bands are absent in the M cut on bilayer FeSe/STO⁷⁴.

1.3 Dissertation Outline

This dissertation focuses on scanning tunneling microscopy studies of superconductivity in single layer FeSe grown on SrTiO₃ substrates by molecular beam epitaxy, and is organized as follows:

Chapter 2 is a brief description of the experimental techniques, including ultrahigh vacuum system, molecular beam epitaxy growth method and scanning tunneling microscopy/spectroscopy.

Chapter 3 presents STM/S investigation of single layer FeSe film with edges of different orientations and roughness. Spatially resolved tunneling spectra are taken on various edges to explore the influence of edge scattering on superconductivity. Then the pairing symmetry in single layer FeSe is investigated by analyzing the extrapolation length.

Chapter 4 presents work on single layer FeSe nanoribbons with well-controlled width. The superconducting gap as a function of the FeSe ribbon width is obtained and the critical ribbon width, below which superconductivity is suppressed, is determined. Possible mechanisms for the ribbon width dependent pair breaking will also be discussed.

Chapter 5 presents the research of single layer $\text{FeTe}_{1-x}\text{Se}_x$ films with various Se concentrations and well-defined edges. By comparing the tunneling spectra taken on the edge and in the bulk, a one-dimensional superconducting channel is observed on the edge of $\text{FeTe}_{1-x}\text{Se}_x$ with Se concentration below 10%. Results of density functional theory (DFT) calculations are utilized to explore the origin of the edge superconductivity.

Finally, Chapter 6 presents a summary of the main findings presented in this dissertation first, followed by preliminary work on FeSe/STO interface engineering, and local superconducting gaps on bilayer FeSe.

References

- 1 Onnes, H. Communications from the Physical Laboratory of the University of Leiden (1911).
- 2 https://en.wikipedia.org/wiki/Meissner_effect.
- 3 Meissner, W. & Ochsenfeld, R. Ein neuer effekt bei eintritt der supraleitfähigkeit. *Naturwissenschaften* **21**, 787-788 (1933).
- 4 London, F. & London, H. The Electromagnetic Equations of the Supraconductor. *Proc. R. Soc. A* **149**, 71 (1935).
- 5 Ginzburg, V.L. & Landau, L.D. On the Theory of superconductivity. *Zh. Eksp. Teor. Fiz.* **20**, 1064-1082 (1950).
- 6 Bardeen, J., Cooper, L. N. & Schrieffer, J. R. Theory of Superconductivity. *Physical Review* **108**, 1175-1204 (1957).
- 7 https://phys.libretexts.org/TextBooks_and_TextMaps
- 8 Phillips, N. E. Heat Capacity of Aluminum between 0.1K and 4.0K. *Physical Review* **114**, 676-685 (1959).
- 9 Guillamón, I. *et al.* Superconducting Density of States and Vortex Cores of 2H-NbS₂. *Physical Review Letters* **101**, 166407 (2008).
- 10 Maxwell, E. Isotope Effect in the Superconductivity of Mercury. *Physical Review* **78**, 477-477 (1950).
- 11 Reynolds, C. A., Serin, B., Wright, W. H. & Nesbitt, L. B. Superconductivity of Isotopes of Mercury. *Physical Review* **78**, 487-487 (1950).
- 12 <http://ummalqura-phy.com/HYPER1/coop.html>.
- 13 Schilling, A., Cantoni, M., Guo, J. D. & Ott, H. R. Superconductivity above 130 K in the Hg-Ba-Ca-Cu-O system. *Nature* **363**, 56 (1993).
- 14 Chu, C. W. *et al.* Superconductivity above 150 K in HgBa₂Ca₂Cu₃O_{8+δ} at high pressures. *Nature* **365**, 323 (1993).
- 15 Stewart, G. R. Unconventional superconductivity. *Advances in Physics* **66**, 75-196 (2017).
- 16 Ray, P. J. Structural investigation of La_{2-x}Sr_xCuO₄. (2015).
- 17 Kamihara, Y., Watanabe, T., Hirano, M. & Hosono, H. Iron-Based Layered Superconductor La[O_{1-x}F_x]FeAs (x = 0.05-0.12) with T_c = 26 K. *Journal of the American Chemical Society* **130**, 3296-3297 (2008).
- 18 Kamihara, Y. *et al.* Iron-Based Layered Superconductor: LaOFeP. *Journal of the American Chemical Society* **128**, 10012-10013 (2006).

- 19 Cao, W. *et al.* Thorium-doping-induced superconductivity up to 56 K in $\text{Gd}_{1-x}\text{Th}_x\text{FeAsO}$. *EPL (Europhysics Letters)* **83**, 67006 (2008).
- 20 Wu, G. *et al.* Superconductivity at 56 K in samarium-doped SrFeAsF . *Journal of Physics: Condensed Matter* **21**, 142203 (2009).
- 21 Peng, C. *et al.* High-Tc superconductivity induced by doping rare-earth elements into CaFeAsF . *EPL (Europhysics Letters)* **85**, 67003 (2009).
- 22 Paglione, J. & Greene, R. L. High-temperature superconductivity in iron-based materials. *Nature Physics* **6**, 645 (2010).
- 23 Stewart, G. R. Superconductivity in iron compounds. *Reviews of Modern Physics* **83**, 1589-1652 (2011).
- 24 Dai, P. Antiferromagnetic order and spin dynamics in iron-based superconductors. *Reviews of Modern Physics* **87**, 855-896 (2015).
- 25 Mizuguchi, Y. & Takano, Y. Review of Fe Chalcogenides as the Simplest Fe-Based Superconductor. *Journal of the Physical Society of Japan* **79**, 102001 (2010).
- 26 Hsu, F.-C. *et al.* Superconductivity in the PbO-type structure $\alpha\text{-FeSe}$. *Proceedings of the National Academy of Sciences* **105**, 14262-14264 (2008).
- 27 Medvedev, S. *et al.* Electronic and magnetic phase diagram of $\beta\text{-Fe}_{1.01}\text{Se}$ with superconductivity at 36.7 K under pressure. *Nature Materials* **8**, 630 (2009).
- 28 Imai, T., Ahilan, K., Ning, F. L., McQueen, T. M. & Cava, R. J. Why Does Undoped FeSe Become a High-Tc Superconductor under Pressure? *Physical Review Letters* **102**, 177005 (2009).
- 29 Guo, J. *et al.* Superconductivity in the iron selenide $\text{K}_x\text{Fe}_2\text{Se}_2$ ($0 \leq x \leq 1.0$). *Physical Review B* **82**, 180520 (2010).
- 30 Sun, L. *et al.* Re-emerging superconductivity at 48 kelvin in iron chalcogenides. *Nature* **483**, 67 (2012).
- 31 Dagotto, E. Colloquium: The unexpected properties of alkali metal iron selenide superconductors. *Reviews of Modern Physics* **85**, 849-867 (2013).
- 32 Shiogai, J., Ito, Y., Mitsuhashi, T., Nojima, T. & Tsukazaki, A. Electric-field-induced superconductivity in electrochemically etched ultrathin FeSe films on SrTiO_3 and MgO . *Nature Physics* **12**, 42 (2015).
- 33 Lei, B. *et al.* Evolution of High-Temperature Superconductivity from a Low-Tc Phase Tuned by Carrier Concentration in FeSe Thin Flakes. *Physical Review Letters* **116**, 077002 (2016).
- 34 Wang, Q.-Y. *et al.* Interface-Induced High-Temperature Superconductivity in Single Unit-Cell FeSe Films on SrTiO_3 . *Chinese Physics Letters* **29**, 037402 (2012).
- 35 Song, C.-L. *et al.* Direct Observation of Nodes and Twofold Symmetry in FeSe Superconductor. *Science* **332**, 1410-1413 (2011).

- 36 Ge, J.-F. *et al.* Superconductivity above 100 K in single-layer FeSe films on doped SrTiO₃. *Nature Materials* **14**, 285 (2014).
- 37 Song, C.-L. *et al.* Molecular-beam epitaxy and robust superconductivity of stoichiometric FeSe crystalline films on bilayer graphene. *Physical Review B* **84**, 020503 (2011).
- 38 Zhang, W.-H. *et al.* Direct Observation of High-Temperature Superconductivity in One-Unit-Cell FeSe Films. *Chinese Physics Letters* **31**, 017401 (2014).
- 39 He, S. *et al.* Phase diagram and electronic indication of high-temperature superconductivity at 65 K in single-layer FeSe films. *Nature Materials* **12**, 605 (2013).
- 40 Enayat, M. *et al.* Real-space imaging of the atomic-scale magnetic structure of Fe_{1+y}Te. *Science* **345**, 653-656 (2014).
- 41 Shishidou, T., Agterberg, D. F. & Weinert, M. Magnetic fluctuations in single-layer FeSe. *Communications Physics* **1**, 8 (2018).
- 42 Huang, D. & Hoffman, J. E. Monolayer FeSe on SrTiO₃. *Annual Review of Condensed Matter Physics* **8**, 311-336 (2017).
- 43 Bang, J. *et al.* Atomic and electronic structures of single-layer FeSe on SrTiO₃(001): The role of oxygen deficiency. *Physical Review B* **87**, 220503 (2013).
- 44 Zhang, W. *et al.* Interface charge doping effects on superconductivity of single-unit-cell FeSe films on SrTiO₃ substrates. *Physical Review B* **89**, 060506 (2014).
- 45 Fangsen, L. *et al.* Atomically resolved FeSe/SrTiO₃(001) interface structure by scanning transmission electron microscopy. *2D Materials* **3**, 024002 (2016).
- 46 Zou, K. *et al.* Role of double TiO₂ layers at the interface of FeSe/SrTiO₃ superconductors. *Physical Review B* **93**, 180506 (2016).
- 47 Herger, R. *et al.* Surface of Strontium Titanate. *Physical Review Letters* **98**, 076102 (2007).
- 48 Sims, H. *et al.* Intrinsic interfacial van der Waals monolayers and their effect on the high-temperature superconductor FeSe/SrTiO₃. *arXiv* 1805.03293 (2018).
- 49 Liu, D. *et al.* Electronic origin of high-temperature superconductivity in single-layer FeSe superconductor. *Nature Communications* **3**, 931 (2012).
- 50 Tan, S. *et al.* Interface-induced superconductivity and strain-dependent spin density waves in FeSe/SrTiO₃ thin films. *Nature Materials* **12**, 634 (2013).
- 51 Zhang, Y. *et al.* Nodeless superconducting gap in A_xFe₂Se₂ (A=K,Cs) revealed by angle-resolved photoemission spectroscopy. *Nature Materials* **10**, 273 (2011).
- 52 Nakayama, K. *et al.* Reconstruction of Band Structure Induced by Electronic Nematicity in an FeSe Superconductor. *Physical Review Letters* **113**, 237001 (2014).
- 53 Shimojima, T. *et al.* Lifting of xz/yz orbital degeneracy at the structural transition in detwinned FeSe. *Physical Review B* **90**, 121111 (2014).

- 54 Mazin, I. I., Singh, D. J., Johannes, M. D. & Du, M. H. Unconventional Superconductivity with a Sign Reversal in the Order Parameter of $\text{LaFeAsO}_{1-x}\text{F}_x$. *Physical Review Letters* **101**, 057003 (2008).
- 55 Fang, C., Wu, Y.-L., Thomale, R., Bernevig, B. A. & Hu, J. Robustness of s-Wave Pairing in Electron-Overdoped $\text{A}_{1-y}\text{Fe}_{2-x}\text{Se}_2$ ($\text{A}=\text{K}, \text{Cs}$). *Physical Review X* **1**, 011009 (2011).
- 56 Yi, Z., Dong-Hui, X., Fu-Chun, Z. & Wei-Qiang, C. Theory for superconductivity in $(\text{Tl},\text{K})\text{Fe}_x\text{Se}_2$ as a doped Mott insulator. *EPL (Europhysics Letters)* **95**, 17003 (2011).
- 57 Yang, F., Wang, F. & Lee, D.-H. Fermiology, orbital order, orbital fluctuations, and Cooper pairing in iron-based superconductors. *Physical Review B* **88**, 100504 (2013).
- 58 Maier, T. A., Graser, S., Hirschfeld, P. J. & Scalapino, D. J. d-wave pairing from spin fluctuations in the $\text{K}_x\text{Fe}_{2-y}\text{Se}_2$ superconductors. *Physical Review B* **83**, 100515 (2011).
- 59 Fa, W. *et al.* The electron pairing of $\text{K}_x\text{Fe}_{2-y}\text{Se}_2$. *EPL (Europhysics Letters)* **93**, 57003 (2011).
- 60 Agterberg, D. F., Shishidou, T., O'Halloran, J., Brydon, P. M. R. & Weinert, M. Resilient Nodeless d-Wave Superconductivity in Monolayer FeSe. *Physical Review Letters* **119**, 267001 (2017).
- 61 Mazin, I. I. Symmetry analysis of possible superconducting states in $\text{K}_x\text{Fe}_y\text{Se}_2$ superconductors. *Physical Review B* **84**, 024529 (2011).
- 62 Chen, X., Maiti, S., Linscheid, A. & Hirschfeld, P. J. Electron pairing in the presence of incipient bands in iron-based superconductors. *Physical Review B* **92**, 224514 (2015).
- 63 Kim, J. S., Tam, G. N. & Stewart, G. R. Unusual sensitivity of superconductivity to strain in iron-based 122 superconductors. *Physical Review B* **91**, (2015).
- 64 Han, Y. *et al.* Superconductivity in Iron Telluride Thin Films under Tensile Stress. *Physical Review Letters* **104**, 017003 (2010).
- 65 Böhmer, A. E. *et al.* Lack of coupling between superconductivity and orthorhombic distortion in stoichiometric single-crystalline FeSe. *Physical Review B* **87**, 180505 (2013).
- 66 Schmidbauer, M., Kwasniewski, A. & Schwarzkopf, J. High-precision absolute lattice parameter determination of SrTiO_3 , DyScO_3 and NdGaO_3 single crystals. *Acta Crystallographica Section B* **68**, 8-14 (2012).
- 67 Peng, R. *et al.* Measurement of an Enhanced Superconducting Phase and a Pronounced Anisotropy of the Energy Gap of a Strained FeSe Single Layer in $\text{FeSe}/\text{Nb:SrTiO}_3/\text{KTaO}_3$ Heterostructures Using Photoemission Spectroscopy. *Physical Review Letters* **112**, 107001 (2014).
- 68 Peng, R. *et al.* Tuning the band structure and superconductivity in single-layer FeSe by interface engineering. *Nature Communications* **5**, 5044 (2014).

- 69 Huang, Z. C. *et al.* Electronic structure and superconductivity of single-layer FeSe on Nb:SrTiO₃/LaAlO₃ with varied tensile strain. *2D Materials* **3**, 014005 (2016).
- 70 Miyata, Y., Nakayama, K., Sugawara, K., Sato, T. & Takahashi, T. High-temperature superconductivity in potassium-coated multilayer FeSe thin films. *Nature Materials* **14**, 775 (2015).
- 71 Zhang, S. *et al.* Role of SrTiO₃ phonon penetrating into thin FeSe films in the enhancement of superconductivity. *Physical Review B* **94**, 081116 (2016).
- 72 Rebec, S. N. *et al.* Coexistence of Replica Bands and Superconductivity in FeSe Monolayer Films. *Physical Review Letters* **118**, 067002 (2017).
- 73 Dung-Hai, L. What makes the T_c of FeSe/SrTiO₃ so high? *Chinese Physics B* **24**, 117405 (2015).
- 74 Lee, J. J. *et al.* Interfacial mode coupling as the origin of the enhancement of T_c in FeSe films on SrTiO₃. *Nature* **515**, 245 (2014).
- 75 Ding, H. *et al.* High-Temperature Superconductivity in Single-Unit-Cell FeSe Films on Anatase TiO₂(001). *Physical Review Letters* **117**, 067001 (2016).

Chapter 2 Experimental Techniques

The research was carried out in an ultrahigh vacuum system with combined *in-situ* capabilities of material growth and property characterization. The involved techniques were ultrahigh vacuum (UHV), molecular beam epitaxy (MBE), and scanning tunneling microscopy/spectroscopy (STM/S). This chapter provides the basic working principles of those techniques. Section 2.1 covers ultrahigh vacuum system. Section 2.2 presents molecular beam epitaxy. Section 2.3 describes scanning tunneling microscopy /spectroscopy. Section 2.4 provides details of a home-built MBE-STM system.

2.1 Ultrahigh Vacuum System

It is critical to keep the experimental system under vacuum to prevent contamination from other molecules for surface science research. An important concept to define the degree of vacuum is the monolayer formation time, which is the time required for a clean surface to be covered by one-layer thickness of gas molecules. For a surface with the sticking coefficient of 1, it takes only one hour to absorb one layer of molecules even under a vacuum of 10^{-9} Torr (Fig. 2.1). Therefore, to maintain a clean sample surface longer than the usual time for laboratory measurements to study the real surface properties, the experiment should be done under ultrahigh vacuum (below 10^{-10} Torr).

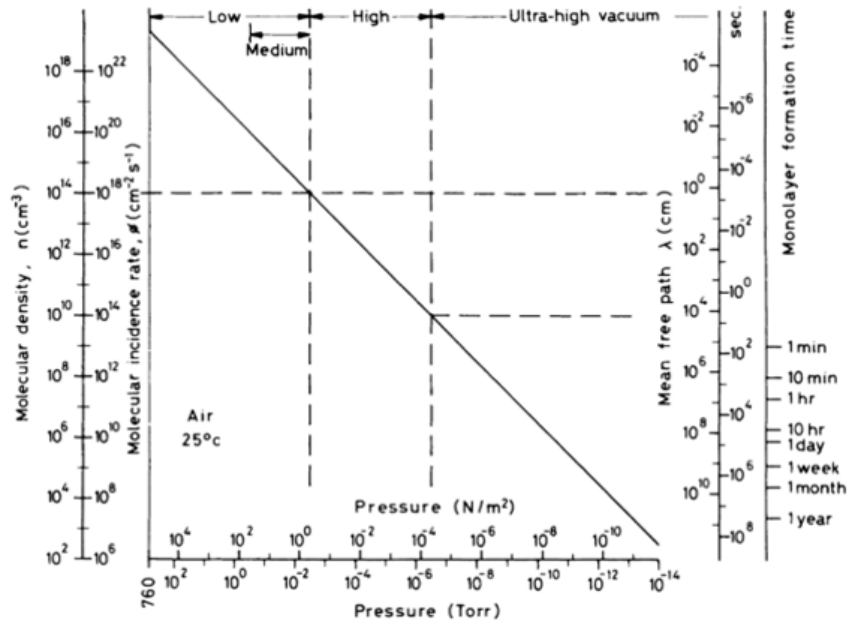


Figure 2.1 Relationship of several concepts defining the degree of vacuum¹.

There are four types of gas sources in a vacuum chamber. First, the initial atmosphere, which is the main gas volume before pumpdown. Second, permeation from the outside. Gas molecules, especially the light ones, e.g. hydrogen and helium, can permeate into the vacuum chamber due to the pressure difference between the inside and the outside. Third, outgassing from chamber surfaces. After pumpdown, the main gas load from the chamber surface is always water vapor. Sufficient bakeout above 100 °C helps to remove the majority of the water. Forth, outgassing from materials. Any material put into the vacuum chamber to be studied or processed will keep evaporating inside the system. Most solid materials we study have a low vapor pressure at room temperature and have little impact on the ultrahigh vacuum. To achieve and sustain ultrahigh vacuum, vacuum pumps are necessarily utilized to remove the initial atmosphere and the constant gas load from both inside and outside of the chambers.

Different pumps have different pumping speed and vacuum limit. The common pumps used in our lab to obtain ultrahigh vacuum are mechanical pump (Fig. 2.2a), turbo pump (Fig. 2.2c) and ion pump (Fig. 2.2d). The pressure inside the vacuum chambers is monitored by the ion gauge (Fig. 2.2g).

The mechanical pump (or rotary pump) is constituted of a stator and an eccentric rotor which has two vanes in a diametral slot (Fig. 2.2b). By rotating the eccentric rotor, gas from the vacuum chamber is sucked into the crescent shaped volume through the inlet, compressed and then exhausted through the outlet. The pressure limit of a typical mechanical pump is about 10^{-4} Torr. The turbo pump is based on the momentum transfer of gas molecules which strike a fast-moving blade. Most turbo pumps employ multiple stages, each consisting of a quickly rotating rotor blade and stationary stator blade pair (Fig. 2.2d). After the gas molecules enter the pump, the rotating blades hit the molecules and transfer mechanical energy to the gas. With this newly acquired momentum, the gas molecules move into the stator layer, which leads them to the next stage where they again collide with the rotor surface. This process is continued, finally leading the gas to the backing pump. Turbo pumps work in the pressure range between 10^{-3} and 10^{-10} Torr, and a backing pump (usually a rotary pump) is necessary.

The ion pump is capable of reaching pressures from 10^{-6} to 10^{-13} Torr, without generating mechanical vibrations, which makes it ideal for STM chambers. An ion pump ionizes gas molecules within the vessel and employs a strong electrical potential, typically 3 to 7 kV, which allows the ions to accelerate into and be captured by a solid electrode (usually titanium) (Fig. 2.2f). Magnets are always used to elongate the trajectory of the ion and increase the ionization rate, thus improve the pumping speed. A forepump (usually a turbo pump) is required to start up the ion pump.

The ion gauge is most widely used high vacuum measuring device. A hot cathode ionization gauge uses the thermionic emission of a heated filament, the emitted electrons being accelerated by the electrostatic field through the helical grid (Fig. 2.2h). The electrons collide with and ionize gas molecules in the enclosed volume. The gas ions are attracted to the ion collector and produce an ion current to reflect the pressure inside.

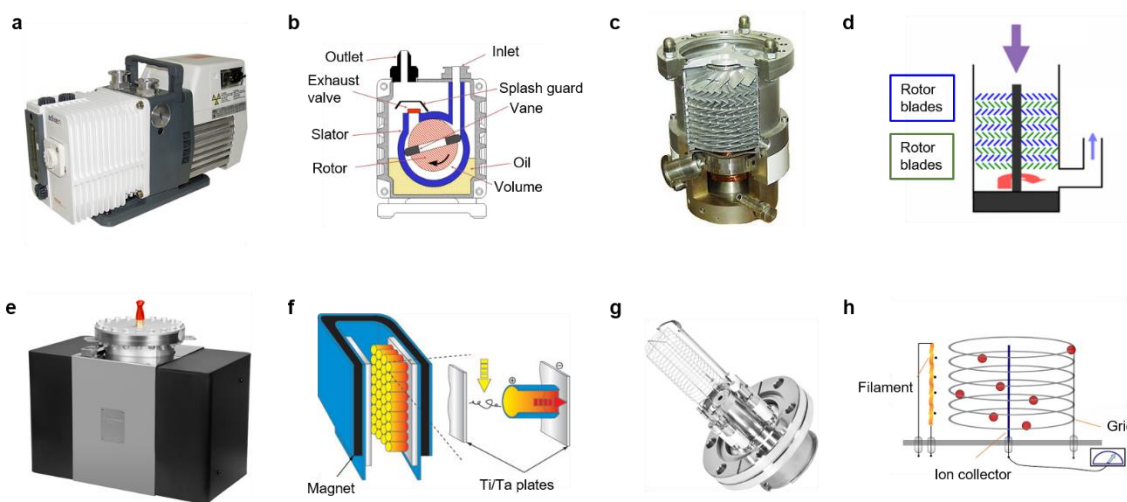


Figure 2.2 a,b, Mechanical pump and the schematic². c,d, Turbo pump and the schematic³. e,f, Ion pump and the schematic⁴. g,h, Ion gauge and the schematic⁵.

2.2 Molecular Beam Epitaxy

Molecular beam epitaxy is the most widely used UHV-based technique to prepare high quality epitaxial structures with monolayer control. The principle underlying MBE is based on the interaction of one or several molecular or atomic beams that occurs on the surface of a heated crystalline substrate. One of our MBE growth chambers is shown in Fig. 2.3a and the schematic of a typical MBE system is shown in Fig. 2.3b. The solid sources materials are placed in effusion

cells to provide an angular distribution of atoms or molecules in a beam. The substrate can be heated to the required temperature for growth.

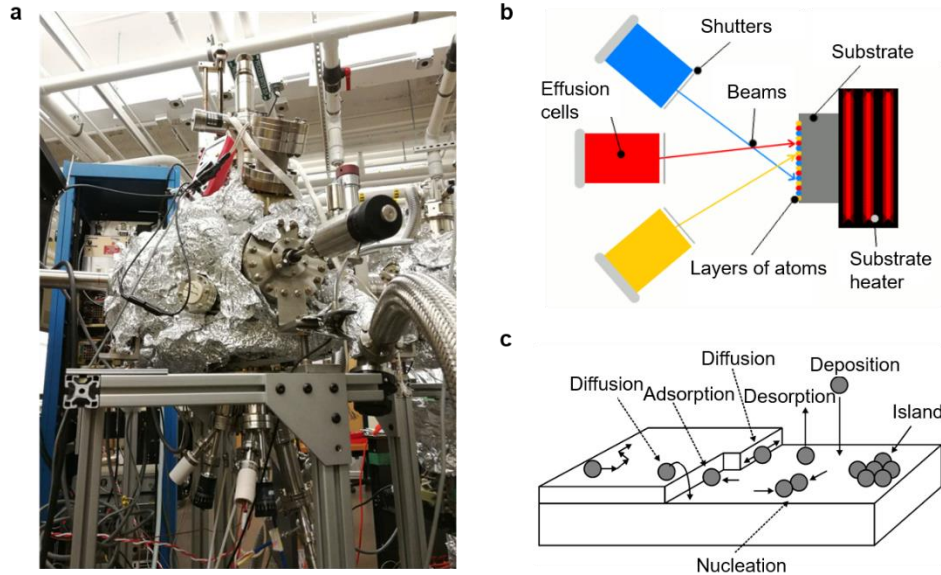


Figure 2.3 a, Picture of an MBE growth chamber. b, Schematic of an MBE system⁶. c, Different surface processes in MBE growth⁷.

There are three phases defined in the MBE process. The first is the crystalline phase of the solid structure grown on the substrate. The second is the gas phase of the source molecular beams. Under ultrahigh vacuum, the mean free path of the flux is much larger than the MBE chamber dimension (Fig. 2.1) that the MBE flux is ballistic and no homogeneous reactions happen in the gas phase. Between the crystalline and gas phases, a third phase which is a surface transition layer can be identified where the deposited source molecules or atoms react with each other and the hot substrate (Fig. 2.3c). This surface transition layer determines the MBE growth process. MBE growth has many advantages. First, the growth takes place under ultrahigh vacuum and avoids contaminations. Second, the growth rate is low and precise monolayer thickness control can be achieved. Third, all sources and the substrate temperature are independently

controlled. Finally, the MBE growth is a non-equilibrium growth process, making it possible to prepare abundant and novel materials.

The effusion cell is the most important component of an MBE system. Commercial MBE source is usually the Knudsen cell (K-cell) (Fig. 2.4). The main components are (1) crucible, made of pyrolytic boron nitride (PBN) or Al_2O_3 . (2) filament, made of tantalum or tungsten. (3) heat shield, to create a uniform heating volume. (4) thermocouple, to measure the material temperature, with a PID regulator to precisely control the source flux. (5) shutter, to control the start and finish of the growth.

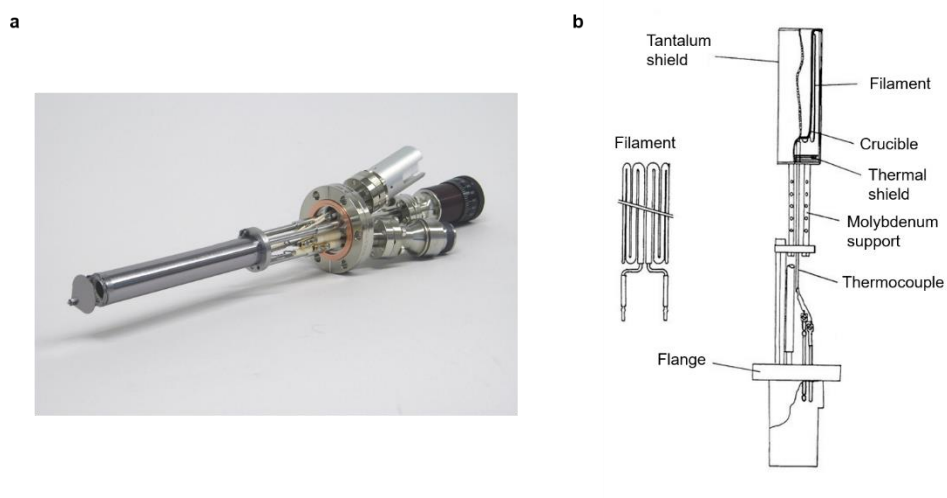


Figure 2.4 a, A Knudsen cell. **b**, Schematic of a Knudsen cell⁸.

Sometimes, home-made tantalum boats are used to evaporate high vapor-pressure metals or molecules, such as Al, Ag, Cu, Fe, Ga, Bi, Sb, Sn and C_{60} . For materials that need very high temperature to evaporate, like W, Mo, Nb, Ta, the e-beam source is used. For gas, liquid molecules and high vapor-pressure (easily sublimated) solids, leak valves are used to control the input. For active metals, like alkali metals, the generating material is a mixture of an alkali metal chromate with a reducing agent and the material is sealed in the alkali metal dispenser.

2.3 Scanning Tunneling Microscopy

Gred Binnig and Heinrich Rohrer, from IBM Zurich, invented scanning tunneling microscope in 1982 and were awarded the Nobel Prize in Physics in 1986. STM is an instrument using a sharp tip to scan the sample surface. Atomic resolution imaging is achieved by detecting the quantum tunneling current between the tip and the sample surface. Both the structural and electronic properties of the sample surface are obtained during the scanning. The invention of STM boosts the development of surface science and nanotechnology.

Schematic of STM setup and the tunneling process is shown in Fig. 2.5. The STM tip is very close ($< 10 \text{ \AA}$) on top of a conducting sample surface. When a bias voltage is applied to the sample or tip, electrons quantum-mechanically tunnel across the potential barrier between the sample and tip, producing a measurable tunneling current (Fig. 2.5a). During imaging, the tip scans across the sample surface controlled by xy piezoelectric elements. To maintain a constant current, a feedback loop is used to adjust the tip height by z piezoelectric element (Fig. 2.5b). The tip motion is recorded and displayed as an STM image, which contains both topographic and electronic information of the sample surface.

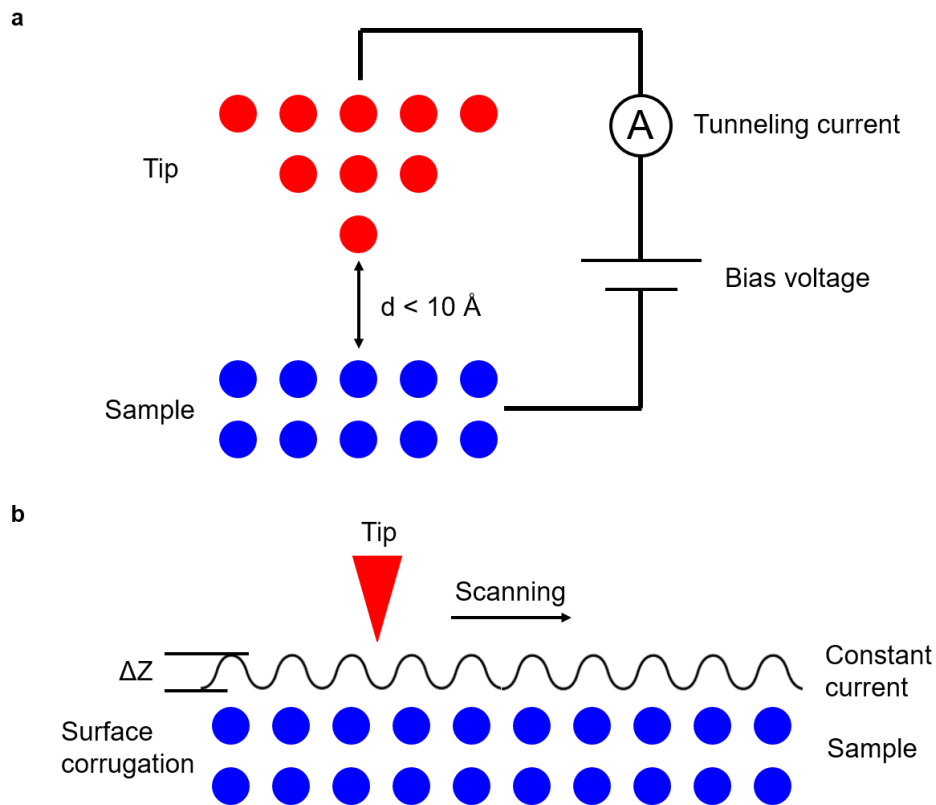


Figure 2.5 a, Setup of an STM. **b**, Schematic of the constant current mode scanning.

2.3.1 An Elementary Model – One-dimensional Potential Barrier

Determination of the tunneling current is the crucial part in STM theory. A simple quantum mechanical calculation demonstrates that the probability of transmission through the potential barrier (between the tip and sample) decreases exponentially with the barrier width and the square root of the barrier height relative to the electron energy (a schematic is shown in Fig. 2.6).

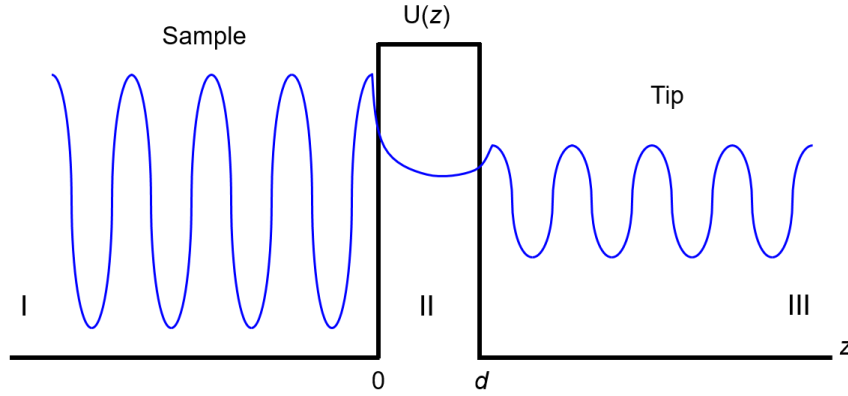


Figure 2.6 Schematic of wavefunction tunneling through a one-dimensional potential barrier of width d .

An electron with mass m and energy E moving in a one-dimensional (in z direction) potential $U(z) > 0$ is described by a wavefunction $\psi(z)$, which satisfies the Schrodinger equation

$$-\frac{\hbar^2}{2m} \frac{d^2}{dz^2} \psi(z) + U(z)\psi(z) = E\psi(z) \quad (2.1)$$

In the classically allowed region $E > U$, solutions are

$$\psi(z) = \psi(0)e^{\pm ikz} \quad (2.2)$$

with wave vector

$$k = \frac{\sqrt{2m(E - U)}}{\hbar} \quad (2.3)$$

and the electron is moving in the positive or negative direction with a constant momentum $p_z = \hbar k$.

In the classically forbidden region $E < U$, solutions are

$$\psi(z) = \psi(0)e^{\pm\kappa z} \tag{2.4}$$

with decay constant

$$\kappa = \frac{\sqrt{2m(U - E)}}{\hbar} \tag{2.5}$$

and the electron is decaying in the $+z$ or $-z$ direction. The probability density of observing an electron near a point z is proportional to $|\psi(z)|^2 = |\psi(0)|^2 e^{\pm 2\kappa z}$.

We can interpret the metal-vacuum-metal (sample-vacuum-tip) junction by taking use of this elementary model. The Fermi level E_F is the upper limit of the occupied states in a metal. The work function ϕ of a metal surface is defined as the minimum energy required to remove an electron from the bulk to the vacuum level, thus from the Fermi level to the vacuum level. In a sample-vacuum-tip junction, without bias voltage, the sample and tip Fermi levels equalize, thus no empty states for net tunneling to happen. By applying a negative sample bias $-V$, the sample Fermi energy will shift up eV . Electrons with energy E between $E_F - eV$ and E_F at the sample surface can tunnel through the vacuum barrier into the tip. The total wavefunction at sample, vacuum (barrier), tip regions are:

I, sample region $z < 0$

$$\psi_{\text{I}} = e^{ikz} + Ae^{-ikz}, k = \frac{\sqrt{2mE}}{\hbar} \quad (2.6)$$

II, barrier region $0 < z < d$

$$\psi_{\text{II}} = Be^{\kappa z} + Ce^{-\kappa z}, \kappa = \frac{\sqrt{2m\phi}}{\hbar} \quad (2.7)$$

III, tip region $z > d$

$$\psi_{\text{III}} = De^{ikz}, k = \frac{\sqrt{2mE}}{\hbar} \quad (2.8)$$

The coefficients A, B, C and D are calculated by the continuity condition of the wavefunctions at the sample-barrier and barrier-tip interface.

The probability current density is defined as

$$j = \frac{\hbar}{2im} \left(\psi^* \frac{d\psi}{dz} - \psi \frac{d\psi^*}{dz} \right) \quad (2.9)$$

The incident wavefunction is $\psi_{\text{I}} = e^{ikz}$, then the incident current is $j_{\text{I}} = \frac{\hbar k}{m}$. The transmitted

wavefunction is ψ_{T} , then the transmitted current is $j_{\text{T}} = \frac{\hbar k}{m} |D|^2$. The transmission coefficient is

$$T = \frac{j_{\text{T}}}{j_{\text{I}}} = \frac{1}{1 + \frac{(\kappa^2 + k^2)^2}{4\kappa^2 k^2} \sinh^2(\kappa d)} \quad (2.10)$$

In common STM experiments, $\phi \sim 4 \text{ eV}$ and $d \sim 5 \text{ \AA}$, the decay constant is large $\kappa \sim 1 \text{ \AA}^{-1}$.

$$T \sim e^{-2\kappa d} \tag{2.11}$$

Therefore, with the sample-tip distance change of 1 \AA , the tunneling current will change by one order of magnitude. This exponential relation between the tunneling current and the sample tip separation gives rise to the high imaging resolution of STM.

2.3.2 Bardeen's Approach

A more sophisticated treatment of the tunneling problem by Bardeen is schematically shown in Fig. 2.7. Bardeen's approach is based on time-dependent perturbation theory with some additional assumptions.

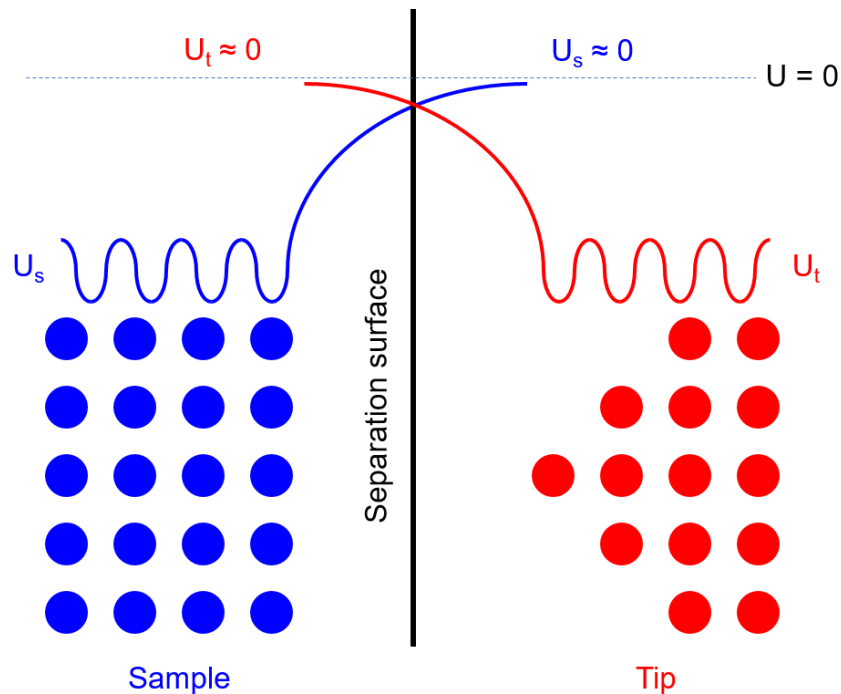


Figure 2.7 Schematic of the Bardeen's approach.

A well-known result from first-order time-dependent perturbation theory is Fermi's golden rule, which states that the transmission rate from the initial state $|i\rangle$ to a final state $|f\rangle$ is given by

$$R_{i \rightarrow f} = \frac{2\pi}{\hbar} |M_{fi}|^2 \delta(E_i - E_f) \quad (2.12)$$

where M_{fi} is the matrix element of the perturbation potential between the initial and final states, and the δ -function ensures energy conservation.

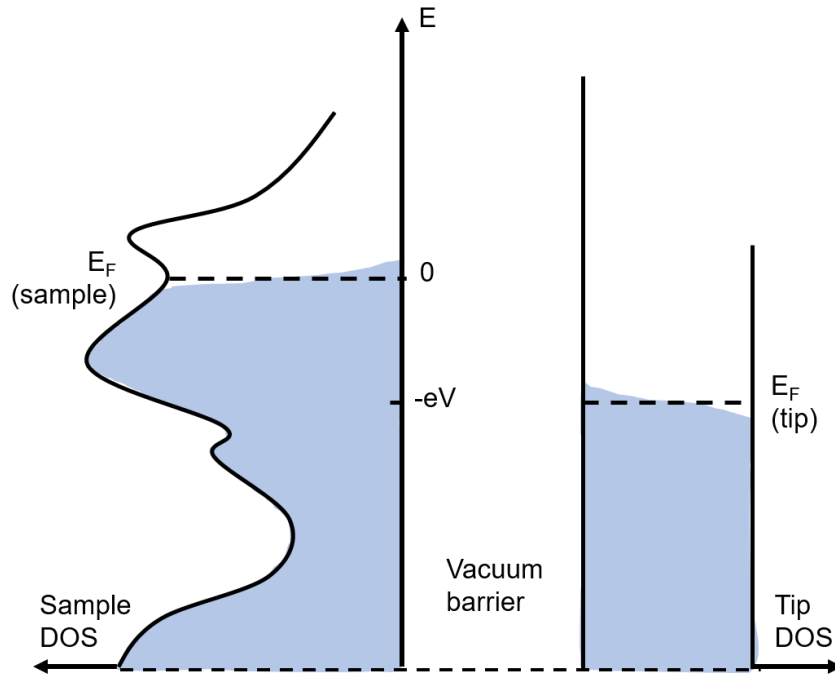


Figure 2.8 Schematic of the sample-tip tunneling process.

This result can be applied to the tunneling process as illustrated in Fig. 2.8. According to Fermi's golden rule, when a negative bias $-V$ is applied to the sample surface, the tunneling current from the sample to the tip for states of energy E (with respect to the Fermi level of the sample) is

$$I_{s \rightarrow t} = 2(-e) \frac{2\pi}{\hbar} |M|^2 \rho_s(E) f_s(E) \rho_t(E + eV) [1 - f_t(E + eV)] \quad (2.13)$$

where the factor 2 accounts for the two spin channels, $-e$ is the electron charge, M is the matrix element, $\rho(E)$ is the density of states, and $f(E)$ is the Fermi-Dirac distribution

$$f(E) = \frac{1}{1 + e^{E/k_B T}} \quad (2.14)$$

The tunneling current from the tip to the sample is

$$I_{t \rightarrow s} = 2(-e) \frac{2\pi}{\hbar} |M|^2 \rho_t(E + eV) f_t(E + eV) \rho_s(E) [1 - f_s(E)] \quad (2.15)$$

The total tunneling current from the sample to the tip is achieved by summing the these two current and then integrate over all energies E

$$I = -\frac{4\pi e}{\hbar} \int_{-E_f(\text{tip})}^{\infty} |M|^2 \rho_t(E + eV) \rho_s(E) \{f(E)[1 - f(E + eV)] - f(E + eV)[1 - f(E)]\} dE \quad (2.16)$$

This expression can be simplified considering all measurements reported in this dissertation were conducted at 6 K and the Fermi-Dirac distribution is nearly a step function

$$I \approx \frac{4\pi e}{\hbar} \int_0^{eV} |M|^2 \rho_t(E + eV) \rho_s(E) dE \quad (2.17)$$

To evaluate the tunneling matrix element M , Bardeen made some assumptions (Fig. 2.7). First, the electron-electron interaction during tunneling is neglected, which is reasonable for low temperature measurement. Second, the tip and sample regimes are considered independent, which is valid if the tip-sample distance is large enough (more than 4 Å should be sufficient). In this scheme, the tip and sample wavefunctions are described by two independent Schrodinger equations

$$(T + U_s)\psi_s = E_s\psi_s \quad (2.18)$$

$$(T + U_t)\psi_t = E_t\psi_t \quad (2.19)$$

where T is the single electron kinetic energy operator, U_s and U_t are the sample and tip potentials. Considering the tip potential as the perturbation, the tunneling matrix element is

$$M = \langle \psi_t | U_t | \psi_s \rangle = \int \psi_t^* U_t \psi_s d^3r \quad (2.20)$$

According to Bardeen's assumption that the tip/sample potential drops exponentially to zero into the sample/tip region, a separation surface S is introduced that at the tip/sample region, $U_s = 0/U_t = 0$. Using $M^* = \langle \psi_s | U_t | \psi_t \rangle$ and equations (2.18) and (2.19), the integral is nontrivial only in the tip region

$$M^* = \int_{\Omega_t} \psi_s^* U_t \psi_t d^3r = \int_{\Omega_t} (\psi_s^* U_t \psi_t - \psi_t U_s \psi_s^*) d^3r$$

$$= \int_{\Omega_t} [\psi_s^*(E_t - T)\psi_t - \psi_t(E_s - T)\psi_s^*]d^3r \quad (2.21)$$

For elastic tunneling, $E_t = E_s$, the matrix element becomes

$$M = \int_{\Omega_t} [\psi_t^*T\psi_s - \psi_sT\psi_t^*]d^3r \quad (2.22)$$

where Ω_t is the tip region volume. This volume integral can be converted to a surface integral by partial integration

$$M = \int_S [\psi_s\nabla\psi_t^* - \psi_t^*\nabla\psi_s]dS \quad (2.23)$$

where S is the separation surface. The tunneling matrix element is independent of the energy difference between the two side of the barrier, i.e. the matrix remains unchanged even if the sample transits from the normal state to the superconducting state.

2.3.3 Tersoff-Hamann Model

From Bardeen's approach, it is necessary to know the tip and sample wavefunctions to calculate the matrix element. In principle it is possible to calculate all tunneling matrix elements with ab-initio methods to gain the tunneling current. However, experimentally the tip structure is not straightforward to access, making it challenging to compute the actual tip wavefunction.

Tersoff and Hamann suggested replacing the unknown electronic structure of the tip with a

simple model, in which the wavefunction of the outmost tip atom is assumed to be an atomic s wave function. Therefore, the STM image is related to the properties of the sample surface alone.

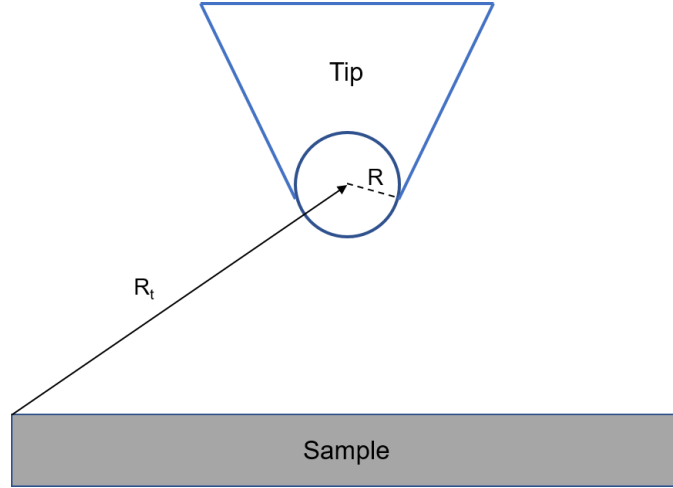


Figure 2.9 Schematic of the TH model.

As shown in the schematic Fig. 2.9, the tip is modeled as a local s wave function of radius R and centered at \vec{R}_t . As the tip and sample regimes are independent, in the separation surface both the tip and sample wavefunctions satisfy the Schrodinger equation

$$-\frac{\hbar^2}{2m}\Delta\psi = -\phi\psi \quad (2.24)$$

where ϕ is the surface work function. With the approximation that the tip is a single atom with s wave function, we take the regular solution that is characterized by an exponential decay from the tip to vacuum

$$\psi_t(\vec{r} - \vec{R}_t) = C \frac{e^{-\kappa|\vec{r} - \vec{R}_t|}}{\kappa|\vec{r} - \vec{R}_t|} \quad (2.25)$$

where \vec{r} is a position in the vacuum (thus no singularity), C is a normalization constant and $\kappa = \frac{\sqrt{2m\phi}}{\hbar}$. Inserting into the expression for the tunneling matrix element and carrying out the integration lead to

$$M = -\frac{2\pi C \hbar^2}{\kappa m} \psi_s(\vec{R}_t) \quad (2.26)$$

Hence the tunneling current at low temperature is

$$I = \frac{16\pi^3 C^2 \hbar^3 e}{\kappa^2 m^2} \rho_t \int_0^{eV} \rho_s(\vec{R}_t, E) dE \quad (2.27)$$

where ρ_t is constant in the TH model, $\rho_s(\vec{R}_t, E) = \sum_s |\psi_s(\vec{R}_t)|^2 \delta(E_s - E)$.

For a small bias voltage V , ρ_s is treated as constant and the tunneling current simplifies to

$$I = \frac{16\pi^3 C^2 \hbar^3 e^2}{\kappa^2 m^2} V \rho_t \rho_s(\vec{R}_t, eV) \quad (2.28)$$

The differential conductance is

$$\frac{dI}{dV} = \frac{16\pi^3 C^2 \hbar^3 e^2}{\kappa^2 m^2} \rho_t \rho_s(\vec{R}_t, eV) \quad (2.29)$$

which is proportional to the sample local density of states $\rho_s(\vec{R}_t, eV)$ at energy eV and position \vec{R}_t .

2.3.4 Operation Modes

Topography

STM is most commonly used to get the sample surface topography. During imaging the tip scans the surface at a fixed bias voltage, and the detected tunneling current goes into a feedback system to control the z piezo voltage to keep the tunneling current constant at the setpoint I_{set} . Recording the voltage to the z piezo during scanning maps the height variation of the sample surface. From equation (2.28), the tunneling current depends on both the tip-sample separation and the local density of states on the sample surface. Hence the topography is a convolution of the geometric corrugation and the electronic density of states.

Spectroscopy

From equation (2.29), the differential conductance at bias V is proportional to the sample local density of states $\rho_s(\vec{R}_t, eV)$. Holding the tip at a constant height, $\rho_s(\vec{R}_t, eV)$ can be measured by sweeping the bias voltage and recording dI/dV . We can measure $I(V)$ and take a numerical derivative to get dI/dV , but the result will be noisy. A better way is to use a lock-in amplifier with a small AC modulation of V to directly measure the difference conductance. The modulated voltage is

$$V(t) = V_0 + V_m \cos(\omega t + \varphi) \quad (2.30)$$

then the measured current is

$$I(V(t)) = I(V_0) + \frac{dI}{dV} \Big|_{V_0} V_m \cos(\omega t + \varphi) + \dots \quad (2.31)$$

where the first harmonic gives the differential conductance. The dI/dV spectrum can be taken at a single point to get the local density of states. It can also be taken when the tip is scanning the surface, giving a spectroscopic imaging.

2.4 Home-built MBE-STM System

Experiments reported in this dissertation are done in a home-built MBE-STM combination system (Fig. 2.10a). The system was first pumped down by mechanical pumps and turbo pumps to 10^{-7} Torr, then baked at $150\text{ }^{\circ}\text{C}$ to reach a base pressure of 10^{-10} Torr. The ultrahigh vacuum is sustained by ion pumps or turbo pumps for different chambers.

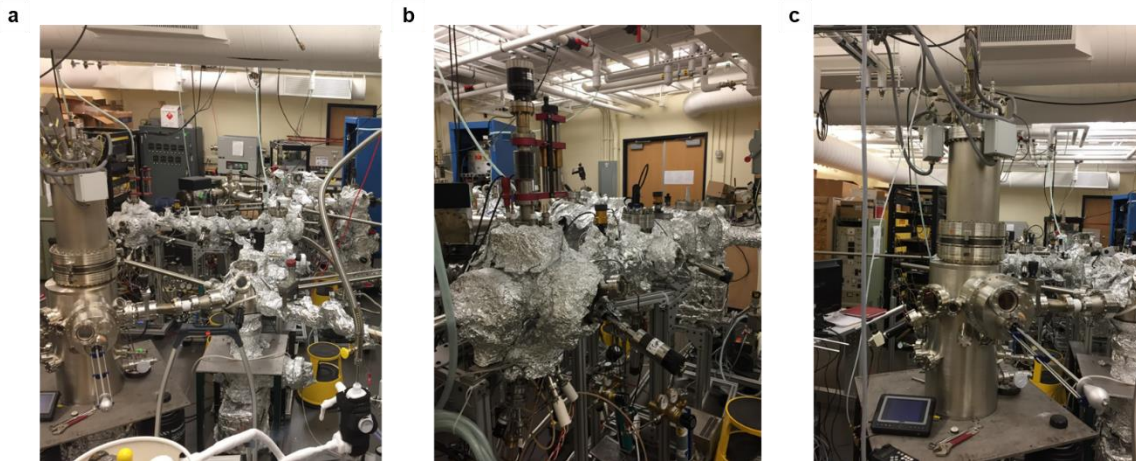


Figure 2.10 **a**, The home-built MBE-STM system. **b**, The FeSe MBE chamber. **c**, The Omicron STM.

Figure 2.10b shows the MBE chamber for single layer FeSe growth. The iron source comes from an e-beam evaporator, and the Se/Te source are controlled by Knudsen cells. A commercial Omicron STM is connected with the ultrahigh vacuum system (Fig. 2.10c). The as-prepared sample can be transferred to the STM chamber for characterization with air exposure,

which is critical for samples with an active surface, e.g. single layer FeSe. The STM chamber is placed on an air-table with four air-legs to reduce vibrational noise. Electronic noise is reduced by adding ceramic feedthrough to electronically isolate the STM, using the same grounding to get rid of ground loops and integrating filters. The STM head, with sample stage and tip, is surrounded by two layers of circular column tanks, which can be filled with liquid nitrogen or liquid helium, to cool down the sample to as low as 6 K.

Two types of STM tips are used in our lab, the mechanically cut platinum iridium (PtIr) tip (fig) and the electrochemically etched tungsten (W) tip (fig) (Fig. 2.11). All the tips are in-situ processed on epitaxially grown silver islands to achieve an ideal condition for imaging and spectroscopy.

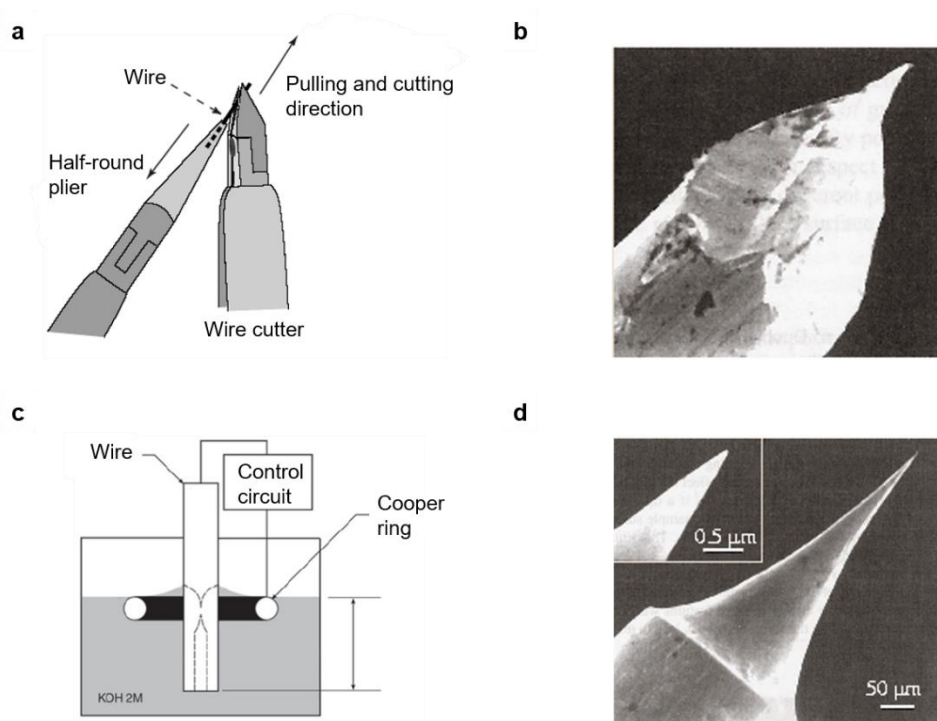


Figure 2.11 a, Illustration of tip cutting. b, Image of a cut PtIr tip. c, Setup of tip etching⁹. d, Image of an etched W tip⁹.

References

- 1 Roth, A. *Vacuum technology*. Elsevier (2012).
- 2 <http://blog.precisionplus.com/commercial-vacuum-pumps-a-summary-of-styles-applications/>.
- 3 https://en.wikipedia.org/wiki/Turbomolecular_pump.
- 4 <http://canvactech.ca/wp/archives/category/rebuilt-categories/ion>.
- 5 <https://www.slideshare.net/LukeHinkle/complex2-simple-vacuum-training-quick-demo-presentation>.
- 6 <https://www.explainthatstuff.com/molecular-beam-epitaxy-introduction.html>.
- 7 <https://www.physik.uni-kl.de/hillebrands/research/methods/molecular-beam-epitaxy/>.
- 8 <https://www.appropedia.org>.
- 9 Bhushan, B. *Springer handbook of nanotechnology*. Springer (2017).

Chapter 3 Nodeless *d*-wave Superconductivity in Single Layer FeSe/SrTiO₃ Probed by Quasiparticle Scattering off Step Edges

3.1 Introduction

A central milestone in the search for high temperature Fe-based superconductors (FeSCs)^{1,2} is the determination of the symmetry of the pairing gap³⁻⁶. The commonly presumed gap structure for FeSCs is sign reversing *s*+ pairing, which results from interband scattering between hole pockets around Γ point and electron pockets around M point in the Brillouin zone (BZ)^{3,7}. This mechanism, however, presents a conundrum in the case of the recently discovered single layer FeSe/STO(001) with the highest superconducting temperature (T_c) to date amongst all FeSCs⁸⁻¹⁰. Due to charge doping from the substrate, the Fermi surface of FeSe consists of only electron pockets centered at the corner (M), with the zone center (Γ) states completely pushed below the Fermi level¹¹⁻¹⁴. Clearly, this poses a challenge for pairing theories that involve both pockets^{3,9}. While isotropic plain *s*-wave pairing was suggested based on earlier ARPES observations and STM measurements of quasiparticle interference (QPI)^{11,15}, more recent ARPES measurements indicate gap anisotropy¹⁶. This anisotropy is naturally explained by a nodeless *d*-wave state, for which the observed gap minima are a manifestation of nodes that have not formed¹⁷. However, gap anisotropy is not a robust probe of pairing symmetry and direct confirmation of any pairing symmetry by phase sensitive measurements is sorely needed³.

One such approach is corner junction measurements^{18,19}, which have revealed *d*-wave pairing in YBa₂Cu₃O_{7- δ} . However, this is challenging for the single layer FeSe system, because the interfacial Josephson current will be suppressed for all states except a plain vanilla *s*-wave state due to gaps of opposite signs on different bands. Alternatively, quasiparticle interference measurements using STM can provide phase sensitive information, however, if the atomic impurities are located at the top surface atomic plane, i.e., Se layer, and not embedded within the Fe plane that is responsible for superconductivity, such scattering and interference patterns may not provide sufficient information on the pairing symmetry^{9,20}.

Within weak-coupling theory²¹, quasiparticle scattering at the boundary of a superconductor is determined by the symmetry of the order parameter (OP) and hence provides another avenue to probe the pairing symmetry. For example, a superconducting OP with phase changes can lead to antiphase interference and suppress superconductivity at the boundary for certain orientations²². This effect can be described by the de Gennes extrapolation length b ²³, which reflects the spatial evolution of the OP near the boundary (Fig. 3.1a)²⁴. For example, for elastic scattering off a specular one-dimensional (1D) edge in two-dimensions, the \mathbf{q} vector is always perpendicular to the edge (Fig. 3.2a). Thus the extrapolation length depends critically on the orientation of the boundary for *d*-wave, but not for conventional *s*-wave superconductors, providing a definitive signature for anisotropic pairing (Fig. 3.2b-e). In the case of single layer FeSe/STO⁹, for nodeless *d*-wave pairing (Fig. 3.1c)^{17,25,26}, the order parameter will change sign after a 90° rotation, where destructive interference can diminish the OP and reduce the pairing gap near the boundary. On the other hand, for *s*-wave pairing (Figs. 3.1d-f)²⁷⁻³⁰, the phase of the order parameter is preserved after a 90° rotation in the one Fe BZ, resulting in a constant gap upon reflection at the boundary. An additional consequence for *d*-wave pairing is the appearance

of Andreev bound states within the gap³¹⁻³⁴. In the case of single layer FeSe, antiphase quasiparticle scattering should lead to in-gap states at specular $[110]_{\text{Fe}}$ edges, but not $[010]_{\text{Fe}}$ edges. As summarized in Table I, the measurements of de Gennes extrapolation length and in-gap states near 1D boundaries with different orientations can provide a viable means to determine the pairing symmetry in single layer FeSe.

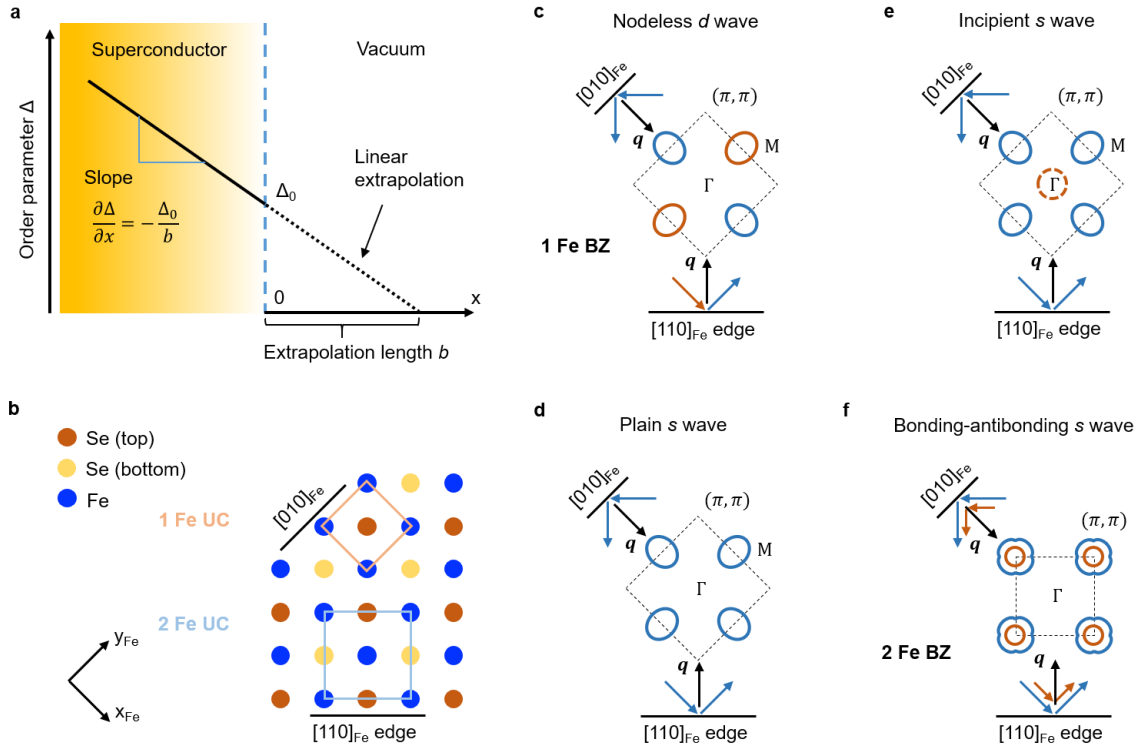


Figure 3.1 a, Schematic diagram of the superconducting extrapolation length. The dashed blue line represents the boundary between a superconductor and the vacuum. The inclined solid black line shows the diminishment of the superconducting order parameter near the boundary. The inclined dotted black line demonstrates linear extrapolation of the order parameter into the vacuum. Δ_0 is the order parameter right at the boundary. The slope of the order parameter profile can be used to determine the extrapolation length b . **b**, Crystal structure of single layer FeSe. The Fe square lattice is rotated 45° to the Se square lattice. The edge orientations $[010]_{\text{Fe}}$ and $[110]_{\text{Fe}}$

are defined in the Fe plane. Both one Fe unit cell (1 Fe UC) and two Fe unit cell (2 Fe UC) are shown and in different colors. **c-f**, Schematics of nodeless d wave, plain s wave and incipient s wave pairing in the one Fe Brillouin zone (1 Fe BZ), and bonding-antibonding s wave pairing in the two Fe Brillouin zone (2 Fe BZ). The ellipses represent the gap structure and the arrows demonstrate the quasiparticle scattering on the $[010]_{\text{Fe}}$ and $[110]_{\text{Fe}}$ edges. The two colors indicate the two signs (blue is positive and brown is negative) of the order parameter.

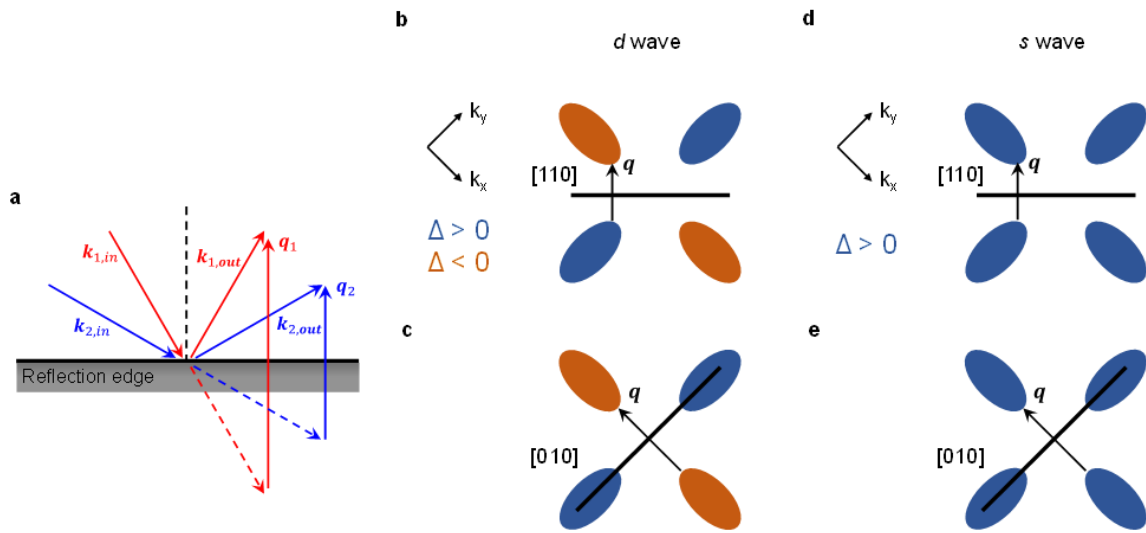


Figure 3.2 **a**, Scattering at a specular edge, where the \mathbf{q} vector is always perpendicular to the edge. **b,c**, Scattering at $[110]$ and $[010]$ edges for d -wave pairing. **d,e**, Scattering at $[110]$ and $[010]$ edges for s -wave pairing.

	<i>D</i> -wave	Plain <i>s</i> -wave	Incipient <i>s</i> -wave	Bonding-antibonding <i>s</i> -wave
b at $[110]_{\text{Fe}}$ edge	Finite	Infinite	Infinite	Finite
IGS at $[110]_{\text{Fe}}$ edge	Yes	No	No	Yes
b at $[010]_{\text{Fe}}$ edge	Infinite	Infinite	Infinite	Finite
IGS at $[010]_{\text{Fe}}$ edge	No	No	No	Yes

Table I Expected extrapolation length b and in-gap states (IGS) at different edges of single layer FeSe for different pairing symmetries.

Here, we present a systematic investigation of edge scattering on superconductivity in MBE grown single layer FeSe/STO(001). *In-situ* STM/S reveals a positive and finite extrapolation length of 8.0 nm for scattering off the $[110]_{\text{Fe}}$ edges, indicating strong Cooper pair destabilization. On the specular $[010]_{\text{Fe}}$ edge, the extrapolation length is nearly infinite. These results are consistent with the nodeless d wave pairing for single layer FeSe film on STO, contrary to previous studies¹⁵. Our study thus demonstrates a new phase sensitive approach to probe the pairing symmetry by boundary scattering in Fe-based superconducting thin films.

3.2 Results and Discussion

Two type of single layer FeSe films were grown on SrTiO₃(001) substrates by MBE in an ultrahigh vacuum system with a base pressure below 1.0×10^{-10} Torr. Nb-doped STO(001) (0.05 wt%) substrates were first annealed at 950 °C for 30 min to produce an atomically flat surface. Then both FeSe films were grown under Se-rich conditions (Fe/Se: 1/10) where Fe flux was provided by electron beam evaporation, and Se from a Knudsen cell with a 0.2 monolayer per minute growth rate. The FeSe films followed a layer-by-layer growth mode, and were post-annealed at ~550 °C for 2-3 hours to remove excess Se on the surface to reach a superconducting state. Afterward, FeSe film #1 was further annealed at ~650 °C for 4 hours and FeSe film #2 was further annealed at ~620 °C for 4 hours to produce single layer films with different types of edges. STM/STS measurements were conducted in an ultrahigh vacuum system with a base pressure of 2.0×10^{-11} Torr, which is directly connected to the MBE growth chamber.

Electrochemically etched polycrystalline W tips, or mechanically sharpened Pt/Ir tips were used for STM imaging at room temperature and liquid helium temperature with the bias voltage applied to the sample. Tunneling spectra were taken at 6 K with a lock-in amplifier (with an AC modulation of 0.4 mV at 860 Hz).

Shown in Figs. 3.3a,c are STM images of two superconducting single layer FeSe films on SrTiO₃(001) with different edge structures. The as-grown films are conformal to the step-terrace morphology of the STO substrates⁸, and not superconducting, likely due to the presence of excess Se as a result of Se-rich growth conditions (Fig. 3.4). Both films were then extensively annealed to induce superconductivity, as verified by *in situ* STM/S and angle-resolved photoemission spectroscopy (ARPES) measurements (Figs. 3.5&3.6). Furthermore, different annealing conditions were used to produce different types of step edges, as discussed in more detail below.

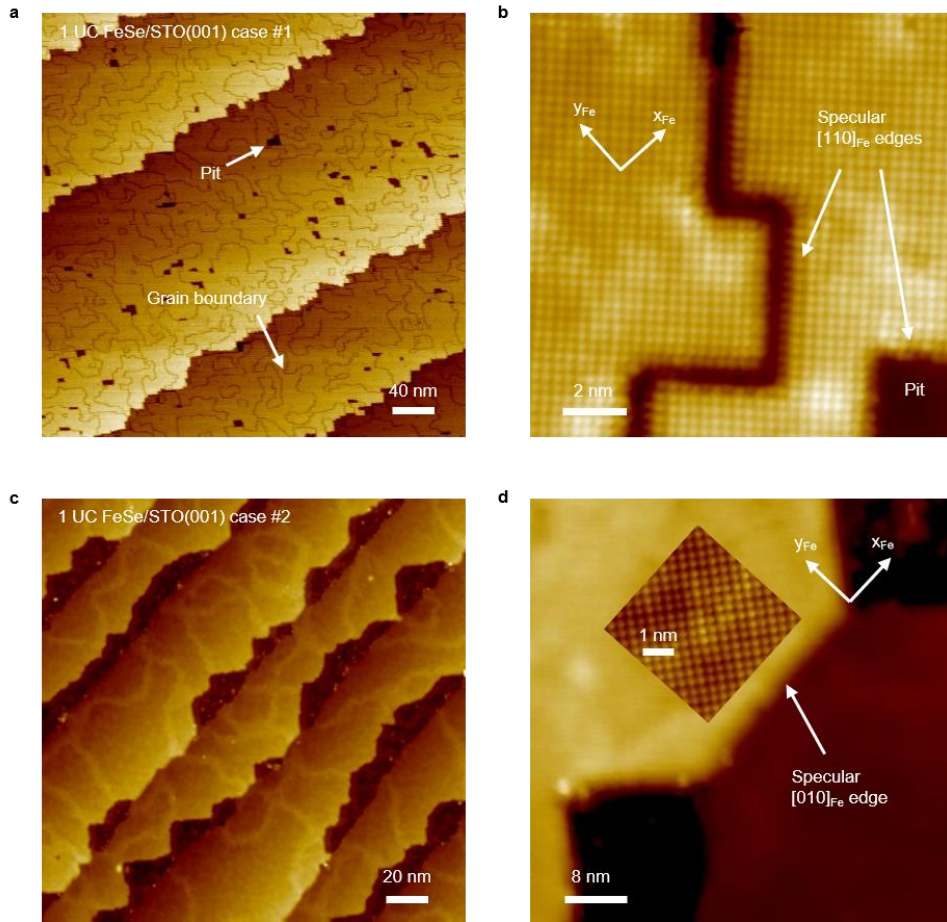


Figure 3.3 a, Large scale STM image of the annealed single layer (1 UC) FeSe film #1 on SrTiO₃(001) ($V_s = 1.0$ V, $I_t = 0.1$ nA). After annealing, there is a high density of low contrast trench grain boundaries and some pits. **b**, Atomic resolution image of specular $[110]_{\text{Fe}}$ edges on FeSe #1 ($V_s = 0.5$ V, $I_t = 0.1$ nA). The single layer FeSe film assumes the in-plane lattice constant of STO(001), thus is slightly under tensile strain. There are two types of $[110]_{\text{Fe}}$ edges here, one is the trench grain boundary (in the middle) and the other is the FeSe-to-STO edge (on the bottom right corner). **c**, Large scale STM image of the annealed single layer FeSe film #2 ($V_s = 1.2$ V, $I_t = 0.1$ nA). The film edges are randomly oriented. **d**, STM image showing a specular $[010]_{\text{Fe}}$ edge on FeSe #2 ($V_s = 1.0$ V, $I_t = 0.1$ nA). Inset is an atomic resolution image indicating the crystalline directions ($V_s = 0.5$ V, $I_t = 0.1$ nA).

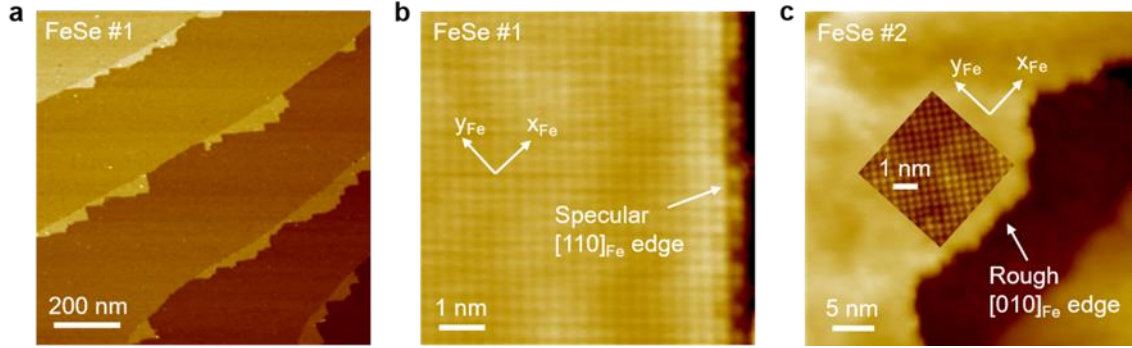


Figure 3.4 a, Large scale STM image of the as-grown single layer FeSe film #1 on SrTiO₃(001) ($V_s = -1.0$ V, $I_t = 0.1$ nA). **b**, Atomic resolution image of a specular FeSe-to-STO $[110]_{Fe}$ edge on FeSe #1 ($V_s = 0.75$ V, $I_t = 0.13$ nA). Some Se atoms along the edge are missing during annealing. **c**, STM image showing a rough $[010]_{Fe}$ edge on FeSe #2 ($V_s = 1.2$ V, $I_t = 0.1$ nA). Inset is an atomic resolution image indicating the crystalline directions ($V_s = 0.5$ V, $I_t = 0.1$ nA).

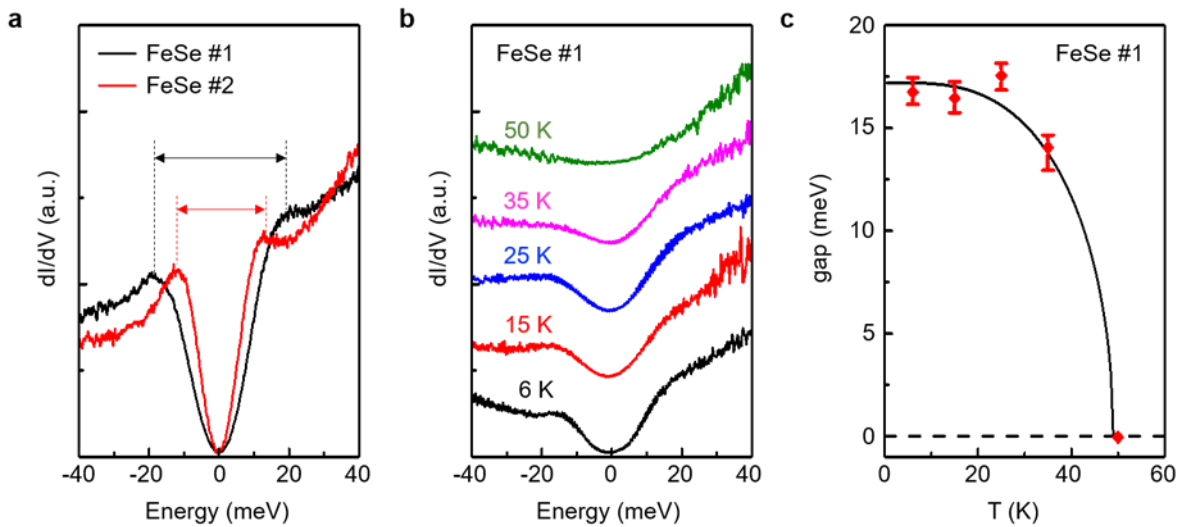


Figure 3.5 a. Two dI/dV spectra taken on FeSe #1 (black) and FeSe #2 (red). The average superconducting gap on FeSe #2 (13 to 15 meV) is smaller than that on FeSe #1 (17 to 19 meV), probably due to the different FeSe/STO interface structures and post-annealing temperatures. **b**. dI/dV spectra taken on FeSe #1 at temperatures marked. **c**, Measured superconducting gaps (red

diamond), and BCS-like fitting (black curve), indicating a superconducting transition temperature of 49 K.

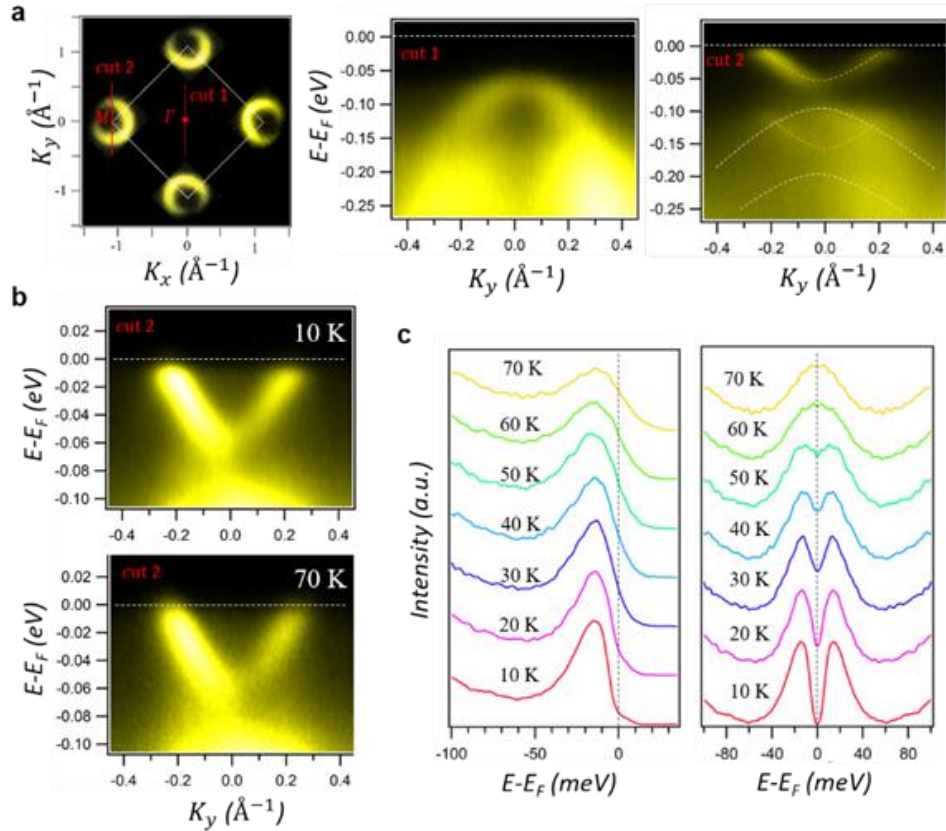


Figure 3.6 a, In-situ ARPES spectra of single layer FeSe film grown on insulating STO substrate, taken across Γ -point (left) and M-point (middle) along the directions as marked in the right 2D intensity plot. **b**, Spectra across M-point measured at 10 K (top) and 70 K (bottom). **c**, Temperature dependent energy distribution curves (EDCs) and symmetrized EDCs at the Fermi crossing, showing the superconducting gap opening between 50 and 60 K.

In the first case, single layer FeSe films (Fig. 3.3) exhibit two types of edges: edges of pits, and those at the low-contrast trench grain boundaries. Figure 3.3b is an atomic resolution image of the edges, showing that both are specular without much disorder (also see Fig. 3.4b).

The square arrays of bright features correspond to Se atoms that terminates the surface. The Fe square lattice lies in the layer below and is diagonally aligned to the surface Se along the labeled x/y directions. Thus, both the edges along the pits and grain boundaries are specular $[110]_{\text{Fe}}$ edges. A superconducting gap of 19 meV is found by dI/dV spectroscopy measurements (Fig. 3.5a). The superconducting transition temperature of 49 K is determined from BCS-like fitting of temperature dependent gaps (Fig. 3.5c), consistent with our ARPES measurements (Fig. 3.6) and earlier works^{8,35}.

In the second case, the FeSe films exhibit randomly oriented high-contrast boundaries, as shown in Fig. 3.3c. This difference in topography is likely due to different post-annealing conditions, and/or the FeSe/STO interface¹⁵. The superconducting gap of this types of sample is also slightly smaller than that on FeSe #1 (Fig. 3.5a), but within the variation from sample to sample that is typically observed. Interestingly, specular $[010]_{\text{Fe}}$ edges are formed along the steps, shown in Fig. 3.3d, with an atomic resolution image showing the Se square lattice rotated 45 degrees from the x/y directions. Rough $[010]_{\text{Fe}}$ edges are also present in this type of samples (Fig. 3.4c).

To determine the superconducting extrapolation length, spatially resolved dI/dV spectra were taken on the both the specular $[110]_{\text{Fe}}$ edge on FeSe #1 (Figs. 3.7a,c) and the specular $[010]_{\text{Fe}}$ edge on FeSe #2 (Figs. 3.7b, d). For the specular $[110]_{\text{Fe}}$ edge, dI/dV spectra taken along the black arrow from point 1 (away from the edge) to point 21 (right at the edge) are shown in Fig. 3.7c. A superconducting gap is observed for all spectra (The procedure to determine the superconducting gap size is illustrated in Fig. 3.8). However the magnitude varies: it is nearly constant at 18.0 ± 0.2 meV for the first 3.5 nm, and then monotonically decreases to 12.8 meV towards the edge. We note that this reduction in the superconducting gap is constant along the

edge, as shown in Fig. 3.9, indicating that suppression in superconductivity is not a local effect. The spatial dependence of the superconducting gap is summarized in Fig. 3.7e, which yields an extrapolation length of 8.0 nm.

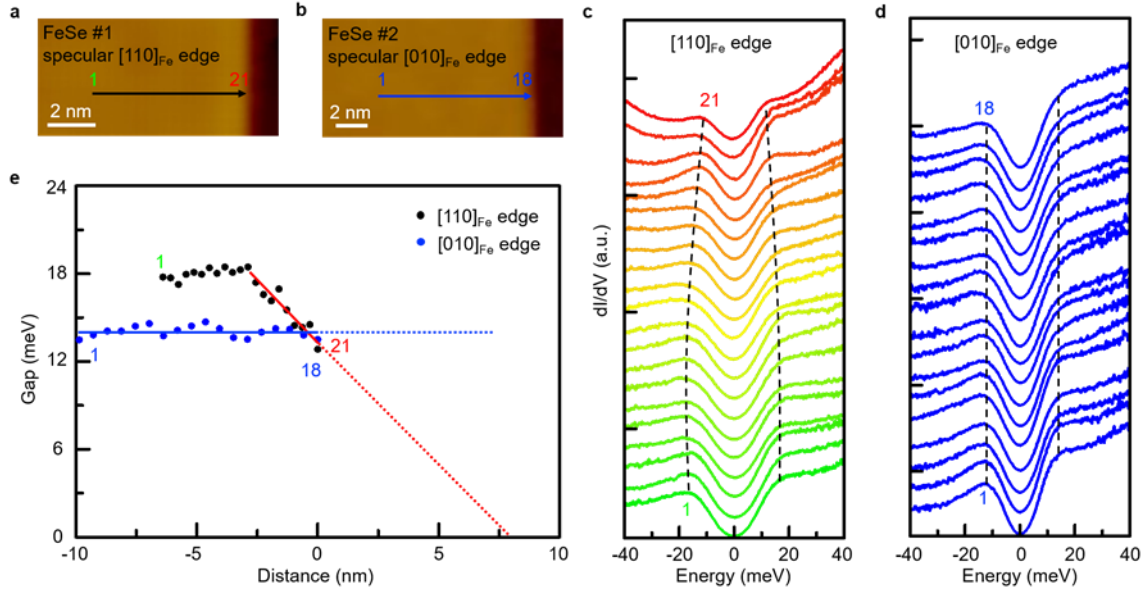


Figure 3.7 **a**, STM image of a specular FeSe #1 $[110]_{\text{Fe}}$ edge ($V_s=1.0$ V, $I_t=0.1$ nA). **b**, STM image of a specular FeSe #2 $[010]_{\text{Fe}}$ edge ($V_s=1.0$ V, $I_t=0.1$ nA). **c**, Spatially resolved dI/dV spectra taken on the $[110]_{\text{Fe}}$ edge, along the black arrow in **a**. The gap size is reduced approaching the edge. The dashed black lines are guide to the evolution of the gap. **d**, Spatially resolved dI/dV spectra taken on the $[010]_{\text{Fe}}$ edge, along the blue arrow in **b**. The gap size is constant of 13.9 ± 0.8 meV. **e**, Profile of the measured superconducting gaps on the $[110]_{\text{Fe}}$ (black dots) and $[010]_{\text{Fe}}$ (blue dots) edges as a function of the position. The solid red line is a linear fit of the gap close to the $[110]_{\text{Fe}}$ edge and the dotted red line is the linear extrapolation. The fitting function is $(13.3-1.67x)$ for the $[110]_{\text{Fe}}$ edge, where x is the distance from the edge and the origin of x is right on the edge. The solid blue line marks the average gap close to the $[110]_{\text{Fe}}$ edge and the dotted blue line is the linear extrapolation.

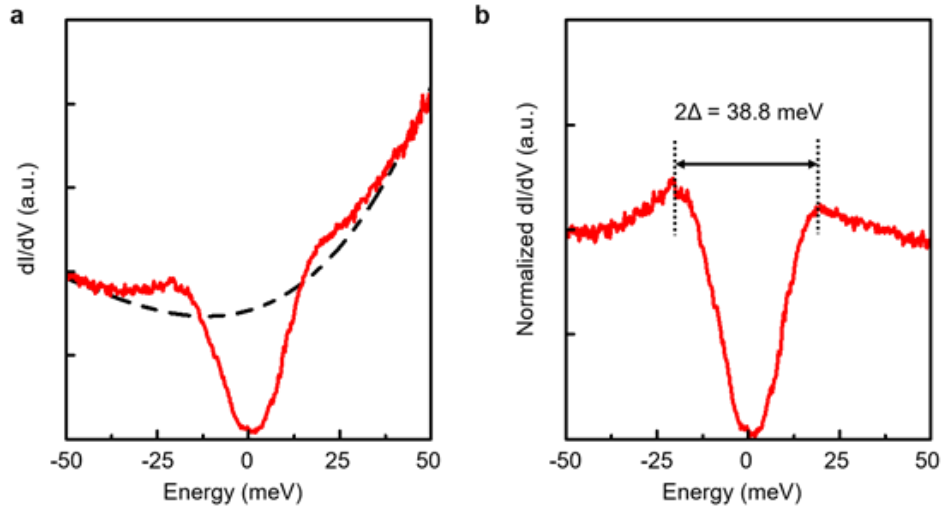


Figure 3.8 a, A cubic fit of the background of a superconducting dI/dV spectrum. The solid red curve is the raw data and the dashed black curve is the cubic fit. **b**, Normalized dI/dV spectrum from **a** by dividing the raw spectrum (the red curve) by the cubic background fit (the black curve). The normalized spectrum has well-defined coherence peaks yielding a superconducting gap of 19.4 ± 0.2 meV.

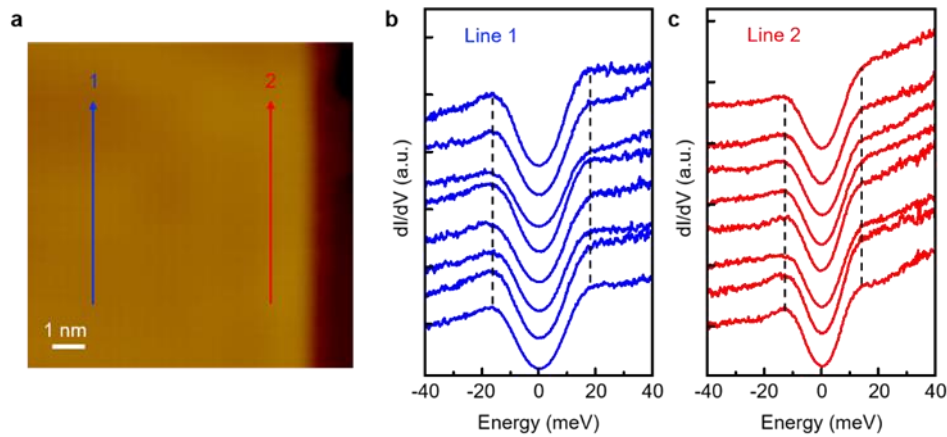


Figure 3.9 a, STM image of the specular $\text{FeSe [110]}_{\text{Fe}}$ film edge in Fig. 3a inset ($V_s = 1.0$ V, $I_t = 0.1$ nA). **b,c**, Spatially resolved dI/dV spectra taken along two lines parallel to the edge. The blue spectra in **b** are taken along the blue arrow in **a**, which is 7 nm away from the edge. The red

spectra in **c** are taken along the red arrow in **a**, which is 1 nm away from the edge. The dashed black lines are guide to the evolution of the gap. The gap sizes are 18.0 ± 0.4 meV in **b** and 14.5 ± 0.3 meV in **c**.

For the specular $[110]_{\text{Fe}}$ edge along grain boundaries on the same sample, a similar analysis of spatially resolved dI/dV spectra reveals a similar extrapolation length of 7.8 nm (Fig. 3.10). This is consistent with the previously proposed grain boundary model³⁴, and confirms that the FeSe step edge and edges at trench boundaries can be considered effectively the same for quasiparticle scattering. For the specular $[110]_{\text{Fe}}$ edge on the second type of FeSe, the extrapolation length is also positive and finite at 9.6 nm (Fig. 3.11), further confirming a consistent behavior for a given edge orientation.

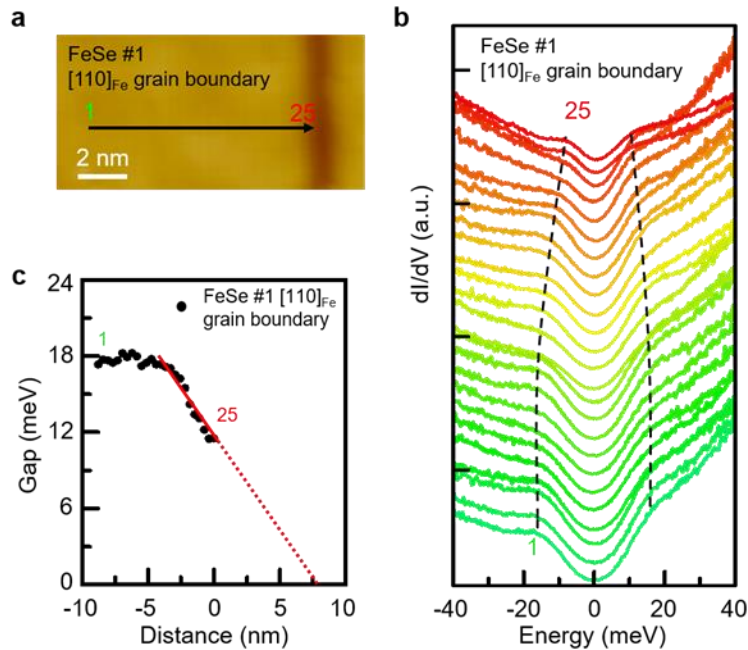


Figure 3.10 a, STM image of a specular FeSe #1 $[110]_{\text{Fe}}$ grain boundary ($V_s = -0.5$ V, $I_t = 0.1$ nA). **b**, Spatially resolved dI/dV spectra taken on the $[110]_{\text{Fe}}$ grain boundary, along the black arrow in **a**. The dashed black lines are guide to the evolution of the gap. **c**, Profile of the

measured superconducting gaps on the $[110]_{\text{Fe}}$ grain boundary as a function of the position. The solid red line is a linear fit of the gap close to the edge and the dotted red line is the linear extrapolation. The fitting function is $11.5-1.48x$, where x is the distance from the edge and the origin of x is right on the edge.

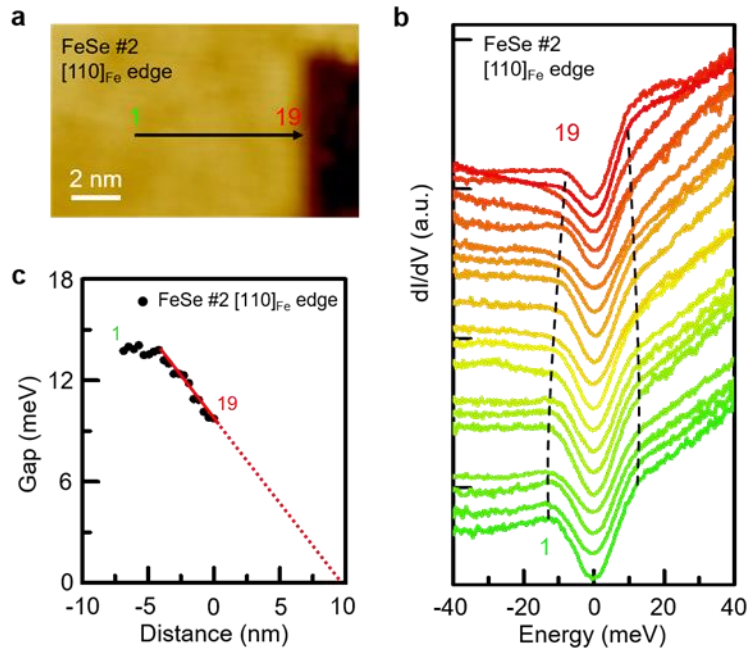


Figure 3.11 a, STM image of a specular FeSe #2 $[110]_{\text{Fe}}$ edge ($V_s= 1.0$ V, $I_t= 0.1$ nA). **b**, Spatially resolved dI/dV spectra taken on the $[110]_{\text{Fe}}$ edge, along the black arrow in **a**. The dashed black lines are guide to the evolution of the gap. **c**, Profile of the measured superconducting gaps on the $[110]_{\text{Fe}}$ edge as a function of the position. The solid red line is a linear fit of the gap close to the edge, and the dotted red line is the linear extrapolation. The fitting function is $9.6-1.0x$, where x is the distance from the edge and the origin of x is right on the edge.

The behavior is quite different for the specular $[010]_{\text{Fe}}$ edge on sample FeSe #2 (Fig. 3.7b). As shown by the spatially resolved dI/dV spectra taken along the blue arrow from point 1

to point 18 in Fig. 3.7d, the gap size is nearly constant at 13.9 ± 0.8 meV at all positions, indicating a nearly infinite extrapolation length (Fig. 3.7e).

For the $[110]_{\text{Fe}}$ edge of single layer FeSe/STO, the positive and finite extrapolation length, about two to three times that of the superconducting coherence length (~ 3.2 nm¹⁵), indicates a strong pair breaking effect. On the contrary for the $[010]_{\text{Fe}}$ edge, the nearly infinite extrapolation length indicates no suppression of superconductivity. This orientation dependent pair breaking effect suggests a 2-fold anisotropy in the superconducting order parameter, which is expected for nodeless d -wave pairing, but not for s -wave pairing. For nodeless $d_{x^2-y^2}$ wave pairing (Fig. 3.1c), the OP changes sign under 90° rotation (C_2 symmetry) in momentum space, and has symmetry such that $\Delta(\mathbf{k}_{in}) = -\Delta(\mathbf{k}_{out})$ for $[110]_{\text{Fe}}$ edge scattering, where \mathbf{k}_{in} and \mathbf{k}_{out} are the incoming and reflected scattering wave vectors. The antiphase interference between $\Delta(\mathbf{k}_{in})$ and $\Delta(\mathbf{k}_{out})$ will diminish the order parameter and suppress superconductivity near the $[110]_{\text{Fe}}$ edge. For the $[010]_{\text{Fe}}$ edge scattering, the OP has a symmetry that warrants $\Delta(\mathbf{k}_{in}) = \Delta(\mathbf{k}_{out})$, thus will not change the pairing gap. Hence no pair breaking effect is expected at the $[010]_{\text{Fe}}$ edge for nodeless d -wave pairing.

On the other hand, for plain s -wave (Fig. 3.1d) and other types of s -wave pairing (Figs. 3.1e&f), the phase of the order parameter is preserved under 90° rotation, thus $\Delta(\mathbf{k}_{in}) = \Delta(\mathbf{k}_{out})$ for both the $[110]_{\text{Fe}}$ and $[010]_{\text{Fe}}$ edge scatterings. Thus, the s -wave superconducting gap will be constant and the extrapolation length will be infinite regardless of the edge orientation. This is consistent with earlier observations of nearly constant superconducting gaps near the edge of Pb islands with conventional s -wave pairing³⁶.

The pair breaking effect should also be sensitive to the roughness of the edges²². In the presence of nanoscale disorder, the scattering angle cannot be precisely defined as it will be a mixture of several possible directions including $[110]_{\text{Fe}}$. Hence antiphase interference will take place regardless of the edge orientation, and superconductivity can be suppressed even at the $[010]_{\text{Fe}}$ edge of the single layer FeSe with nodeless d -wave pairing. Note that in this case the pair breaking effect is weaker and the extrapolation length will be longer than that of the specular $[110]_{\text{Fe}}$ edge where scattering is coherent. Shown in Fig. 3.12a is an STM image of a rough $[010]_{\text{Fe}}$ edge on sample FeSe #2, and spatially resolved dI/dV spectra (Fig. 3.12b). Clearly, a reduction in the superconducting gap size from 13.8 to 10.1 meV is observed towards the edge (Figs. 3.12b,c). A linear fit indicates an extrapolation length of 16.3 nm, which is finite but longer than that for the specular $[110]_{\text{Fe}}$ edge (Figs. 3.7c,e), in excellent agreement with that would be expected for scattering off of a rough edge in a nodeless d -wave superconductor.

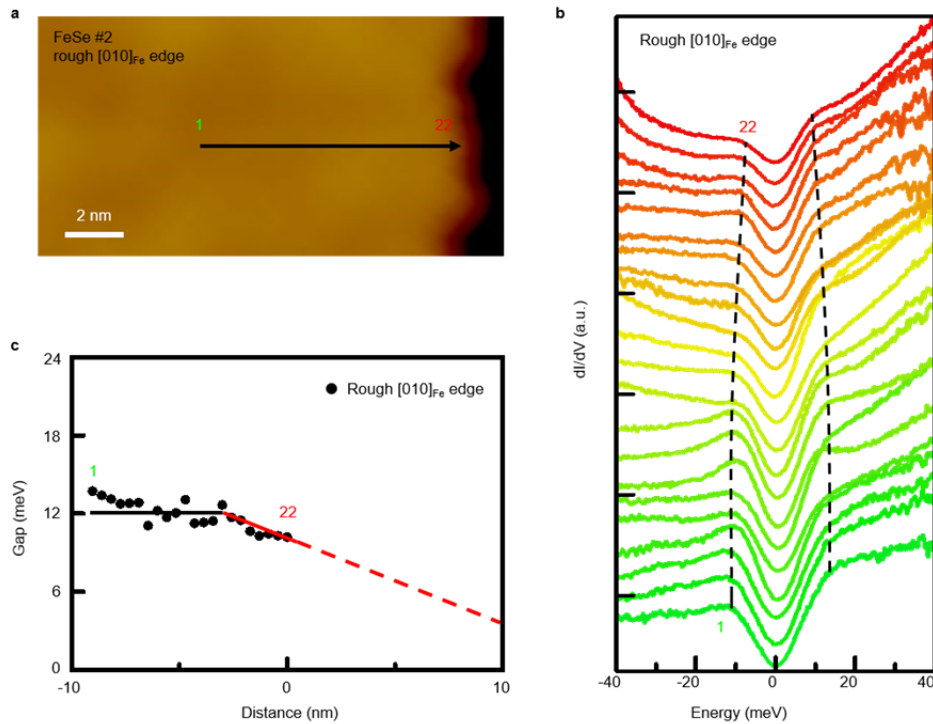


Figure 3.12 a, STM image of a rough FeSe #2 $[010]_{\text{Fe}}$ edge ($V_s= 1.2$ V, $I_t= 0.1$ nA). **b**, Spatially resolved dI/dV spectra taken on the rough $[010]_{\text{Fe}}$ edge, along the black arrow in **a**. The dashed black lines are guide to the evolution of the gap. **c**, Profile of the measured superconducting gaps on the $[010]_{\text{Fe}}$ edge as a function of the position. The solid red line is a linear fit of the gap close to the edge and the dotted red line is the linear extrapolation. The fitting function is $(9.97-0.61x)$, where x is the distance from the edge and the origin of x is right on the edge.

Our experimental observation of anisotropic extrapolation length is also inconsistent with the plain s_{++} and incipient s -wave pairing (Figs. 3.1d&e, respectively) where only one phase of the superconducting OP around the M point exists and hence no antiphase interference is expected. For bonding-antibonding s -wave pairing (Fig. 3.1f), the OP has two phases around the M point, hence antiphase interference can, in principle, occur via interband scattering between the electron pockets. However, here the pair breaking effect is independent of edge orientation, and would occur on both specular $[110]_{\text{Fe}}$ and $[010]_{\text{Fe}}$ edges. This is inconsistent with our observations (Fig. 3.7), where the large anisotropy in the extrapolation length observed between the specular $[110]_{\text{Fe}}$ and $[010]_{\text{Fe}}$ edges indicates a C_2 angular symmetry of the superconducting order parameter. Therefore, our findings indicate that of the possible candidate gap structures (Figs. 3.1c-f) proposed, nodeless d wave pairing is the most likely pairing symmetry for single layer FeSe on STO.

We note that the weak-coupling theory previously developed for the extrapolation length assumes a single band Fermi surface²¹. However, single layer FeSe is multiband and this plays a key feature in the nodeless d -wave pairing state¹⁷. If the FeSe were single band, then any d -wave state has to have nodes. The fact that two bands have energy differences less than the gap energy in some momentum-space directions is what allows for nodeless pairing. In these cases,

interband pairing can now play a role. The multiband Fermi surface in single layer FeSe thus presents a difficulty in using previous calculations to determine the extrapolation length. However, once the band splitting is greater than the gap energy, then the usual theory can be used. This applies to most of the Fermi surface of single layer FeSe, except a narrow range near where the nodes should have been. Hence the nodeless d -wave order parameter will have sign changes as in earlier theories and the pairing symmetry analysis from the extrapolation length can be applied to our experiment.

As discussed above (c.f. Table I), a nodeless d -wave pairing will also give rise to in-gap states at finite energies for specular $[110]_{\text{Fe}}$ edges, in contrast to the usually expected zero energy states for a nodal d -wave superconductor. To better visualize the appearance of in-gap states, we normalize the spatially resolved dI/dV spectra shown in Figs. 3.7c,d by subtracting spectrum 1 (away from the edge), as shown in Figs. 3.13a,b. The normalized zero bias conductance (ZBC) is summarized in Fig. 3.13c. For the specular $[110]_{\text{Fe}}$ edge, in-gap states (peaked at $\pm (6 \pm 1)$ meV) appear at 3 to 4 nm from the edge and enhances significantly towards the edge. In contrast, for the specular $[010]_{\text{Fe}}$ edge, only weak fluctuations are observed in the normalized dI/dV spectra with no in-gap states present. For the rough $[010]_{\text{Fe}}$ edge, in-gap states do appear (Fig. 3.14) as a result of contributions from different scattering angles. Comparison to the expected signatures of several pairing gap structures proposed as summarized in Table I, our findings indicate nodeless d -wave pairing symmetry for single layer FeSe/STO.

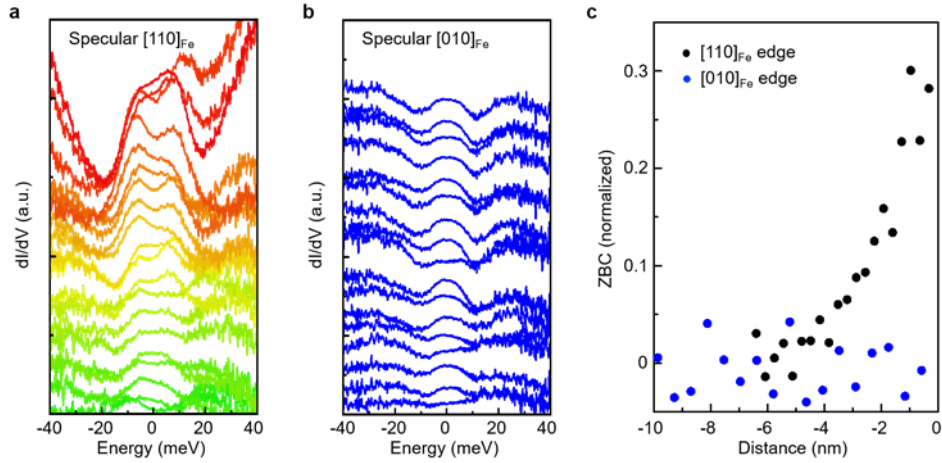


Figure 3.13 a, The same set of spatially resolved dI/dV spectra on the specular $[110]_{Fe}$ edge as in Fig. 3.7c, except that the spectrum at point 1 is subtracted as the background to highlight the in-gap density of state. **b**, The same set of spatially resolved dI/dV spectra on the specular $[010]_{Fe}$ edge as in Fig. 3.7d, except that the spectrum at point 1 is subtracted as the background to highlight the in-gap density of state. **c**, Zero bias conductance (ZBC), extracted from **a** and **b**, evolution approaching the $[110]_{Fe}$ edge (black dots) and the $[010]_{Fe}$ edge (blue dots).

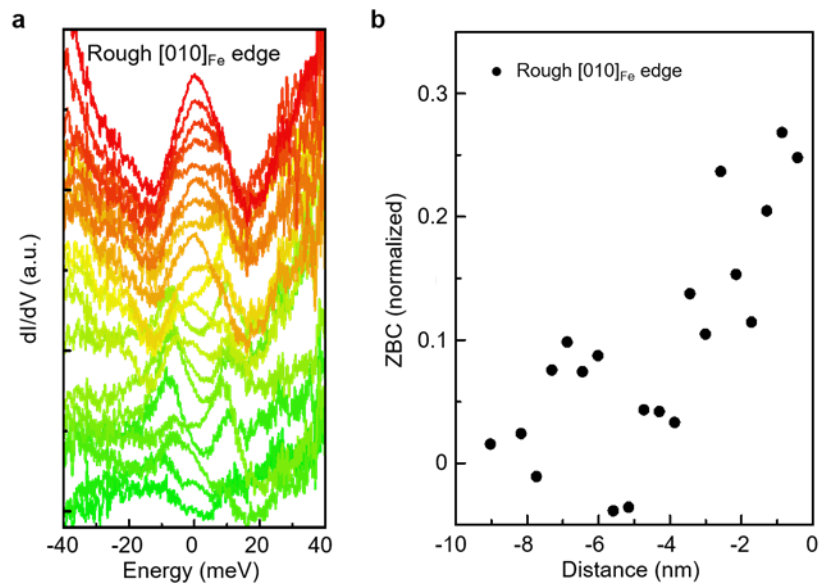


Figure 3.14 a, The same set of spatially resolved dI/dV spectra on the rough $[010]_{\text{Fe}}$ edge as in Fig. 3.12b, except that the spectrum at point 1 is subtracted as the background to highlight the in-gap density of state. **b**, Zero bias conductance (ZBC), extracted from **a**, evolution approaching the rough $[010]_{\text{Fe}}$ edge (black dots).

3.3 Summary

In conclusion, we have epitaxially grown superconducting single layer FeSe films on STO(001) substrates with various types of edges: the specular $[110]_{\text{Fe}}$ and $[010]_{\text{Fe}}$, and the rough $[010]_{\text{Fe}}$ edges. For the specular $[110]_{\text{Fe}}$ edge, spatially resolved dI/dV spectroscopy reveals a suppression of superconductivity near the edge with an extrapolation length of 8.0 nm, indicating strong pair breaking. In contrast, at the specular $[010]_{\text{Fe}}$ edge, no suppression of superconductivity is observed with a near infinite extrapolation length. At the rough $[010]_{\text{Fe}}$ edge, a longer extrapolation length of 16.3 nm is observed, as a result of the mixed scattering directions. This edge orientation dependence on pairing destabilization is consistent with nodeless d -wave pairing symmetry. Our findings further demonstrate that quasiparticle scattering at the boundaries of nanostructures is a viable phase sensitive probe of pairing symmetry of Fe-based superconductors.

References

- 1 Paglione, J. & Greene, R. L. High-temperature superconductivity in iron-based materials. *Nature Physics* **6**, 645 (2010).
- 2 Stewart, G. R. Superconductivity in iron compounds. *Reviews of Modern Physics* **83**, 1589-1652 (2011).
- 3 Hirschfeld, P. J., Korshunov, M. M. & Mazin, I. I. Gap symmetry and structure of Fe-based superconductors. *Reports on Progress in Physics* **74**, 124508 (2011).
- 4 Hirschfeld, P. J. Using gap symmetry and structure to reveal the pairing mechanism in Fe-based superconductors. *Comptes Rendus Physique* **17**, 197-231(2016).
- 5 Chubukov, A. Pairing Mechanism in Fe-Based Superconductors. *Annual Review of Condensed Matter Physics* **3**, 57-92 (2012).
- 6 Wang, F. & Lee, D.-H. The Electron-Pairing Mechanism of Iron-Based Superconductors. *Science* **332**, 200-204 (2011).
- 7 Mazin, I. I., Singh, D. J., Johannes, M. D. & Du, M. H. Unconventional Superconductivity with a Sign Reversal in the Order Parameter of $\text{LaFeAsO}_{1-x}\text{F}_x$. *Physical Review Letters* **101**, 057003 (2008).
- 8 Wang, Q.-Y. *et al.* Interface-Induced High-Temperature Superconductivity in Single Unit-Cell FeSe Films on SrTiO_3 . *Chinese Physics Letters* **29**, 037402 (2012).
- 9 Huang, D. & Hoffman, J. E. Monolayer FeSe on SrTiO_3 . *Annual Review of Condensed Matter Physics* **8**, 311-336 (2017).
- 10 Ge, J.-F. *et al.* Superconductivity above 100 K in single-layer FeSe films on doped SrTiO_3 . *Nature Materials* **14**, 285 (2014).
- 11 Liu, D. *et al.* Electronic origin of high-temperature superconductivity in single-layer FeSe superconductor. *Nature Communications* **3**, 931 (2012).
- 12 Tan, S. *et al.* Interface-induced superconductivity and strain-dependent spin density waves in FeSe/ SrTiO_3 thin films. *Nature Materials* **12**, 634 (2013).
- 13 Lee, J. J. *et al.* Interfacial mode coupling as the origin of the enhancement of T_c in FeSe films on SrTiO_3 . *Nature* **515**, 245 (2014).
- 14 He, S. *et al.* Phase diagram and electronic indication of high-temperature superconductivity at 65 K in single-layer FeSe films. *Nature Materials* **12**, 605 (2013).
- 15 Fan, Q. *et al.* Plain s -wave superconductivity in single-layer FeSe on SrTiO_3 probed by scanning tunneling microscopy. *Nature Physics* **11**, 946 (2015).
- 16 Zhang, Y. *et al.* Superconducting gap anisotropy in monolayer FeSe thin film. *Physical Review Letters* **117**, 117001 (2016).
- 17 Agterberg, D. F., Shishidou, T., O'Halloran, J., Brydon, P. M. R. & Weinert, M. Resilient nodeless d -Wave superconductivity in monolayer FeSe. *Physical Review Letters* **119**, 267001 (2017).

- 18 Wollman, D. A., Van Harlingen, D. J., Lee, W. C., Ginsberg, D. M. & Leggett, A. J. Experimental determination of the superconducting pairing state in YBCO from the phase coherence of YBCO-Pb dc SQUIDs. *Physical Review Letters* **71**, 2134-2137 (1993).
- 19 Van Harlingen, D. J. Phase-sensitive tests of the symmetry of the pairing state in the high-temperature superconductors - Evidence for $d_{x^2-y^2}$ symmetry. *Reviews of Modern Physics* **67**, 515-535 (1995).
- 20 Liu, C. *et al.* Extensive impurity-scattering study on the pairing symmetry of monolayer FeSe films on SrTiO₃. *Physical Review B* **97**, 024502 (2018).
- 21 Monthoux, P., Balatsky, A. V. & Pines, D. Weak-coupling theory of high-temperature superconductivity in the antiferromagnetically correlated copper oxides. *Physical Review B* **46**, 14803-14817 (1992).
- 22 Alber, M. *et al.* Surface boundary conditions for the Ginzburg-Landau theory of d-wave superconductors. *Physical Review B* **53**, 5863-5871 (1996).
- 23 De Gennes, P. G. Boundary effects in superconductors. *Reviews of Modern Physics* **36**, 225-237 (1964).
- 24 Fink, H. J., Haley, S. B., Giuraniuc, C. V., Kozhevnikov, V. F. & Indekeu *, J. O. Boundary conditions, dimensionality, topology and size dependence of the superconducting transition temperature. *Molecular Physics* **103**, 2969-2978 (2005).
- 25 Maier, T. A., Graser, S., Hirschfeld, P. J. & Scalapino, D. J. d-wave pairing from spin fluctuations in the K_xFe_{2-y}Se₂ superconductors. *Physical Review B* **83**, 100515 (2011).
- 26 Fa, W. *et al.* The electron pairing of K_xFe_{2-y}Se₂. *EPL (Europhysics Letters)* **93**, 57003 (2011).
- 27 Fang, C., Wu, Y.-L., Thomale, R., Bernevig, B. A. & Hu, J. Robustness of s-Wave Pairing in Electron-Overdoped A_{1-y}Fe_{2-x}Se₂ (A = K, Cs). *Physical Review X* **1**, 011009 (2011).
- 28 Yang, F., Wang, F. & Lee, D.-H. Fermiology, orbital order, orbital fluctuations, and Cooper pairing in iron-based superconductors. *Physical Review B* **88**, 100504 (2013).
- 29 Chen, X., Maiti, S., Linscheid, A. & Hirschfeld, P. J. Electron pairing in the presence of incipient bands in iron-based superconductors. *Physical Review B* **92**, 224514 (2015).
- 30 Mazin, I. I. Symmetry analysis of possible superconducting states in K_xFe_ySe₂ superconductors. *Physical Review B* **84**, 024529 (2011).
- 31 Satoshi, K. & Yukio, T. Tunnelling effects on surface bound states in unconventional superconductors. *Reports on Progress in Physics* **63**, 1641 (2000).
- 32 Nagato, Y. & Nagai, K. Surface and size effect of a d_{xy} -state superconductor. *Physical Review B* **51**, 16254-16258 (1995).
- 33 Hu, C.-R. Midgap surface states as a novel signature for $d_{x_a^2-x_b^2}$ -wave superconductivity. *Physical Review Letters* **72**, 1526-1529 (1994).

- 34 Misra, S. *et al.* Formation of an Andreev bound state at the step edges of $\text{Bi}_2\text{Sr}_2\text{CaCu}_2\text{O}_{8+\delta}$ surface. *Physical Review B* **66**, 100510 (2002).
- 35 Zhi, L. *et al.* Molecular beam epitaxy growth and post-growth annealing of FeSe films on SrTiO_3 : a scanning tunneling microscopy study. *Journal of Physics: Condensed Matter* **26**, 265002 (2014).
- 36 Kim, J. *et al.* Visualization of geometric influences on proximity effects in heterogeneous superconductor thin films. *Nature Physics* **8**, 464 (2012).

Chapter 4 Width-dependent Suppression of Superconductivity in Single Layer FeSe Nanoribbons

4.1 Introduction

Superconductivity is characterized by multiple length scales. In bulk superconductors, London penetration depth, the distance to which a magnetic field penetrates into a superconductor, and the coherence length, the minimum length to sustain superconducting phase coherence, are fundamental parameters that establish the limit for superconductivity. At the reduced dimensions, however, a critical minimum length scale for sustaining superconductivity arises from size effects. Superconductivity is usually suppressed at the length scale smaller than the coherence length in conventional superconductors. For 0D nanoparticles¹⁻³, Anderson criterion¹ determines the critical superconducting particle size where the quantum confinement induced Kubo gap⁴ (the mean energy level spacing) equals the bulk superconducting gap. For 1D nanowires, the proliferation of phase slips, resulting from thermal or quantum fluctuations, determines the minimum diameter that can sustain superconductivity^{5,6}.

For high-temperature superconductors, the minimum length scale is elusive due to the challenges in synthesizing nanostructures. Fe-based superconductor (FeSC) is a representative family of high-temperature superconductors and the superconductivity is believed to originate within the common two-dimensional (2D) X-Fe-X (X can be pnictogen or chalcogen) layers^{7,8}. It is therefore ideal to produce superconducting single-layer X-Fe-X nanoribbons of various width to study the size effect on high-temperature superconductivity. Recently discovered single layer

FeSe on SrTiO₃(001) consists of the simplest Se-Fe-Se structure with probably the highest T_c amongst all FeSCs and can be a model system to study the superconducting size effect^{9,10}.

Here we present a systematic investigation of size-dependent superconductivity in single layer FeSe nanoribbons. High-temperature superconducting single layer FeSe films were grown on SrTiO₃(001) substrate by MBE, followed by extensive annealing at 650 °C to produce well-defined FeSe nanoribbons with width ranging from a few to tens of nanometers. *In-situ* STM/S reveals three types of tunneling spectra: the superconducting gap, the V shape and the U shape. For ribbons larger than 9.0 nm, the dI/dV spectra have a superconducting gap with well-defined coherence peaks of up to 20 meV. Between 7.2 and 9.0 nm, the gap can still be resolved, while the coherence peaks are no longer well-defined. Below the critical width of 7.2 nm, superconductivity is suppressed in the FeSe nanoribbon. The spectra are V-shaped between 5.0 and 7.2 nm, and U-shaped below 5.0 nm. The U shape regime is likely a result of quantum confinement and the V shape regime is consistent with antiphase edge scattering induced gap suppression for *d*-wave superconductivity. Our findings confirm the destabilization of superconductivity in iron-based superconductors at reduced scale and determine the critical superconducting FeSe ribbon width.

4.2 Results and Discussion

Single layer FeSe films were grown on STO(001) substrates by MBE in an ultrahigh vacuum system with a base pressure below 1.0×10^{-10} Torr. Nb-doped STO(001) (0.05 wt%) substrates were first annealed at 950 °C for 30 min to produce an atomically flat surface. Then FeSe films were grown under Se-rich conditions (Fe/Se: 1/10) where Fe flux was provided by

electron beam evaporation, and Se from a Knudsen cell with a 0.2 monolayers per minute growth rate. The FeSe films followed a layer-by-layer growth mode, and were post-annealed at ~ 550 °C for 2-3 hours to remove excess Se on the surface to reach a superconducting state, and then further annealed at ~ 650 °C for 10 hours to produce FeSe nanoribbons.

Figure 4.1a shows an STM image of superconducting single layer FeSe on STO, where the film is conformal to the step-terrace morphology of the STO(001) substrates⁹. The film is also characterized by a high density of grain boundaries (GBs), appearing as a network of meandering lines with low contrast (Fig. 4.1a). Consistent with earlier studies, the as-grown FeSe films are not superconducting, likely due to the presence of excess Se as a result of Se-rich growth conditions¹¹. After annealing at 550 °C for ~ 2 hours to remove the excess Se, scanning tunneling spectroscopy reveals a superconducting gap of ~ 20 meV, measured by half of the energy difference between two coherence peaks (Fig. 4.1b), also consistent with earlier work^{9,12}. Furthermore, the originally meandering GB network also evolves into straight trenches after the annealing¹², as shown in Fig. 4.1c. The film now consists of larger grains ~ 50 nm in size, with crystallographic axes aligned with the STO(001). However, as shown in the atomic resolution image, the two grains across the grain boundary can exhibit a relative shift of one half of the lattice constant, i.e., the different grains within the FeSe film likely have different epitaxial relationships to the underlying STO(001) substrate.

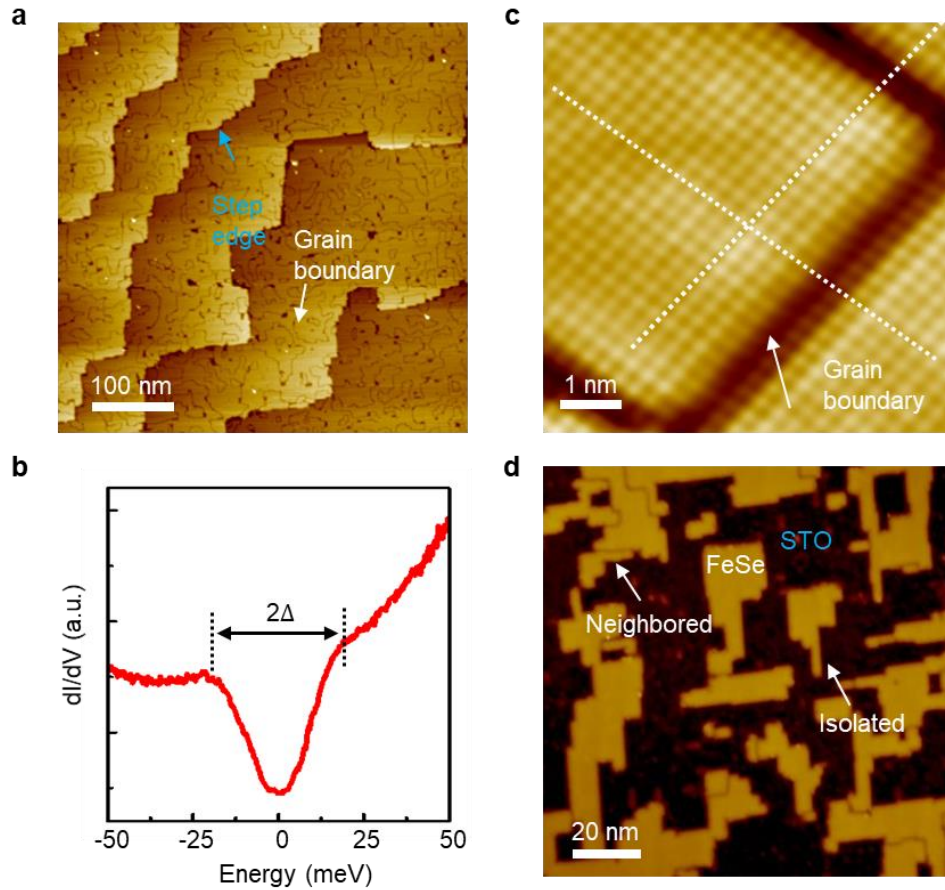


Figure 4.1 a, Large-scale STM image of a single layer FeSe film on SrTiO₃ ($V_s = -0.9$ V, $I_t = 0.1$ nA). The arrow marks a meandering grain boundary. **b**, dI/dV spectrum taken on single layer FeSe at 6 K. A 20 meV gap is defined by half the coherence peak-to-peak spacing. **c**, Atomic resolution STM image of a trench grain boundary ($V_s = 0.7$ V, $I_t = 0.1$ nA). The single layer FeSe film assumes the in-plane lattice constant of STO(001), thus is slightly under tensile strain. The dotted lines are guides to show the relative shift in alignment between the two grains. **d**, STM image of single layer FeSe nanoribbons after extensive annealing ($V_s = 0.5$ V, $I_t = 0.1$ nA).

Further annealing at 650 °C leads to the partial desorption of FeSe film and the formation of FeSe nanoribbons, ranging from a few to several tens of nanometers in width, measured from line profiles of STM images (Fig. 4.1d). Two types of ribbons are found: completely isolated

with only FeSe-to-STO edges, and neighbored with FeSe-to-STO edges on one side and trench-like GBs on the other side. As tunneling spectra reveal similar electronic structures for both types of nanoribbons of the same size, they are hence treated with no distinction in the following analysis.

dI/dV tunneling spectra were taken on FeSe nanoribbons of width ranging from 4.1 to 19.0 nm to investigate size effects on superconductivity, as shown in Fig. 4.2. For wide ribbons 1 and 2, at 19 and 12 nm, the spectra show clear superconducting gaps of 18 and 19 meV, respectively, similar to those taken on continuous FeSe films (e.g., Fig. 4.1b). At a reduced width of 7.3 nm (ribbon 3), while its tunneling spectrum is still gapped, the coherence peaks are no longer well defined. At 6.6 nm width (ribbon 4), the tunneling spectrum appears as V-shaped, indicating that superconductivity is suppressed. Further reducing the ribbon width to 4.7 (ribbon 5) and 4.1 nm (ribbon 6), the tunneling spectra become U-shaped with a gap of ~ 60 meV centered around the Fermi level, indicating that superconductivity is completely destabilized.

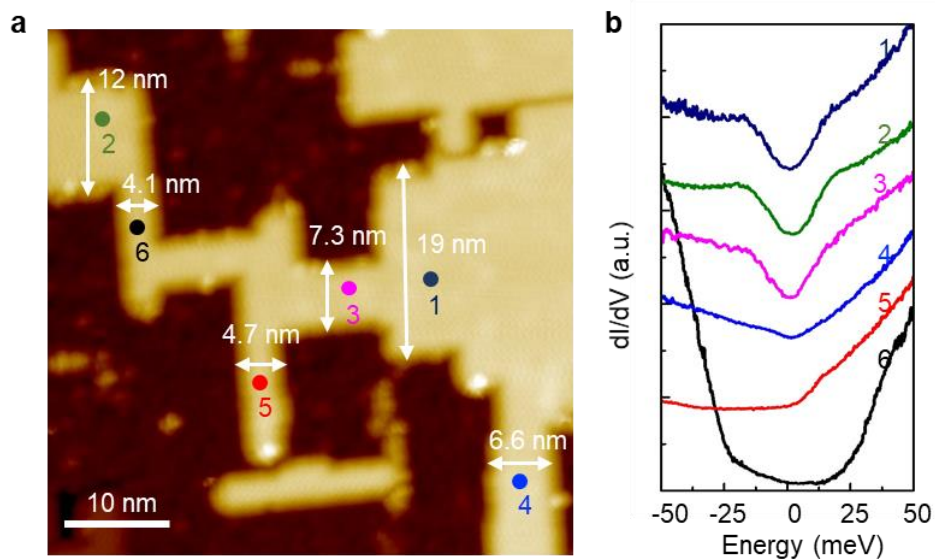


Figure 4.2 a, STM image of FeSe ribbons of various widths ($V_s = 1.0$ V, $I_t = 0.1$ nA). **b**, dI/dV spectra taken at six ribbons of different widths from 19.0 nm to 4.1 nm, labeled as ribbon 1 to 6 in **a**.

Another spatially resolved tunneling spectra along a ribbon with varying width suggest that only the shorter dimension (i.e., the width in term of nanoribbons) plays the dominant role in modifying superconductivity. This effect is shown in Fig. 4.3 where spatially resolved STSs are taken on a ribbon of varying width (3.5, 6.5, and >15 nm). For points 1 through 4 where the shorter dimensions (widths) are 3.5 and 6.5 nm, tunneling spectra are U-shaped for points 1 and 2, and V-shaped for points 3 and 4, indicating the suppression of superconductivity. For points 5 and 6 where the dimensions are >15 nm, the spectrum is gapped with coherence peaks at ± 19 meV, indicating superconductivity. The fact that only the shorter dimension, and not the aspect ratio, matters is further confirmed by examining “quantum dots”, where the aspect ratios are close to 1, such as the example shown in Fig. 4.3c inset. Tunnel spectrum taken on this quantum dot exhibits a U-shape (Fig. 4.3c), revealing that again superconductivity is suppressed. These results indicate that as long as one dimension of the nanoribbons is less than a critical width, superconductivity is suppressed, irrespective of the length of the other dimension, or aspect ratio.

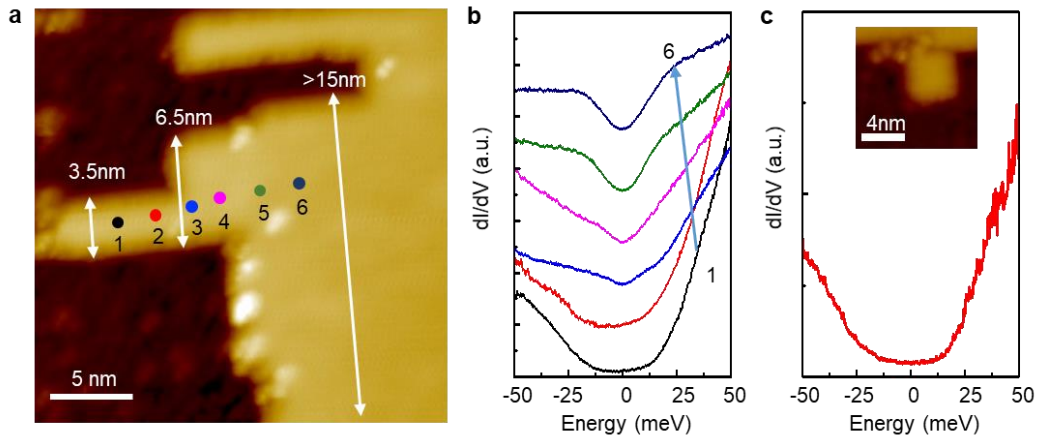


Figure 4.3 a, STM image of a FeSe nanoribbon of varying width ($V_s = 1.0$ V, $I_t = 0.1$ nA). **b**, dI/dV spectra taken at points 1-6 marked in **a**. **c**, dI/dV spectrum taken on a square-shaped FeSe quantum dot shown in the inset ($V_s = 1.2$ V, $I_t = 0.1$ nA).

Further analysis of tunneling spectra of additional similar FeSe nanoribbons confirms a critical ribbon width of 7.2 nm, below which superconductivity is suppressed (Fig. 4.4). For ribbons wider than 7.2 nm, superconducting gaps between 15 and 20 meV are observed that are relatively independent of the ribbon width. Note that between 7.2 and 9.0 nm, the superconducting coherence peaks start being suppressed (e.g. point 3 in Fig. 4.2). Between 5.0 and 7.2 nm, tunneling spectra generally exhibit a V shape, and below 5.0 nm a U shape with quantum well states (c.f. Fig. 4.5b). This evolution of the tunneling spectra clearly shows the suppression of the superconducting gap in FeSe nanoribbons with ribbon widths. The presence of two distinct V-shaped and U-shaped regime indicates different mechanisms for the suppression of superconductivity below the critical width.

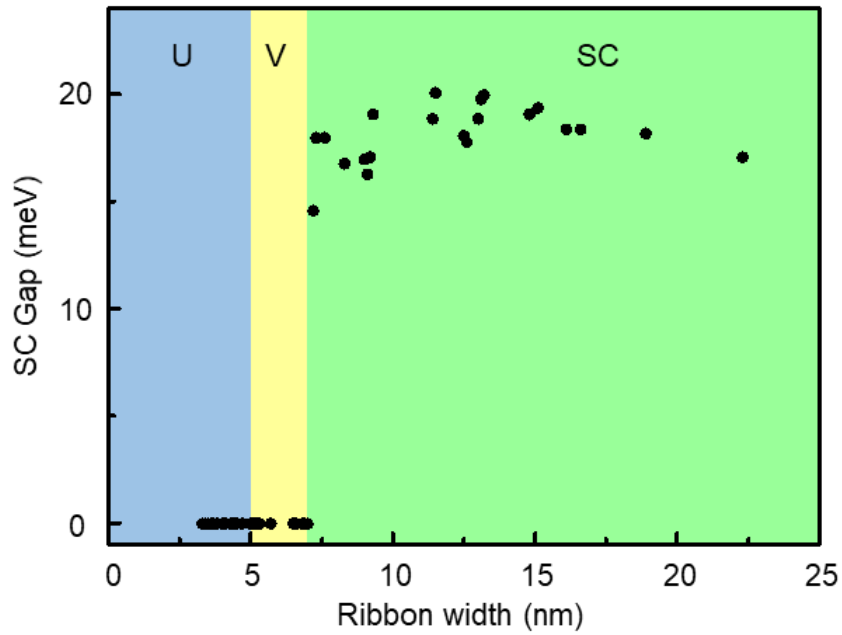


Figure 4.4 Plot of superconducting (SC) gaps as a function of single layer FeSe ribbon width.

The green regime has well-defined superconducting gaps, the yellow regime has V-shaped spectra with no coherence peaks and the blue regime has U-shaped spectra.

The U-shaped regime below 5.0 nm probably results from quantum confinement induced reduction of density of states (DOS) near the Fermi level, evidenced by the quantum well states observed in our experiment for ribbons smaller than 5.0 nm. Figs. 4.5a&b are larger scale dI/dV spectra taken at two ribbons of 20 and 4.8 nm wide. It evidently reveals that quantum well states (multiple peaks in the dI/dV spectrum) show up (from about -200 to -300 meV) when superconductivity is completely suppressed (at 4.8 nm). Density function theory (DFT) calculation also confirms the existence of singularities and reduced DOS between the singularities in FeSe nanoribbons at reduced widths (Figs. 4.5c&d). Note that due to the lack of constraint in the ribbon length direction, this quantum confinement effect is different from the Anderson criterion where absolute empty DOS near the Fermi level is required¹.

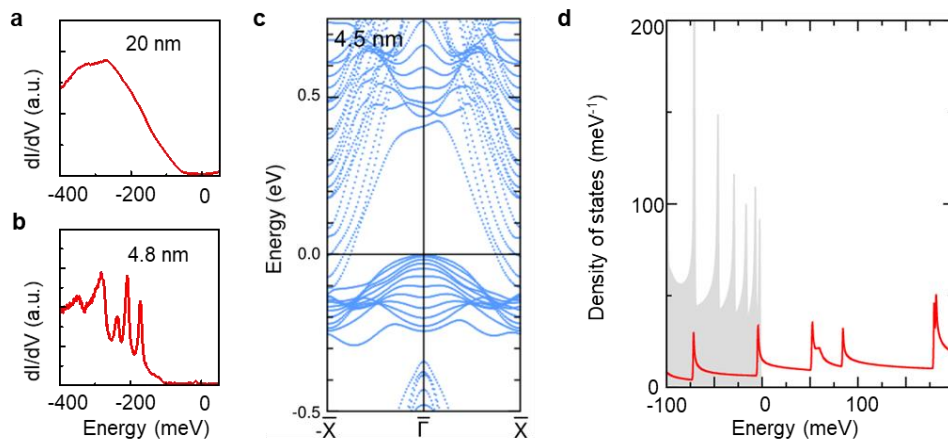


Figure 4.5 a, dI/dV spectrum taken at a 20 nm wide ribbon. **b**, dI/dV spectrum taken at a 4.8 nm wide ribbon. **c**, Calculated bands for a 4.5 nm ribbon. **d**, Calculated density of states of a 4.5 nm ribbon.

Different from the U-shaped regime where the normal state has changed, the V-shaped regime shows a complete suppression of superconducting coherence. Recent ARPES experiment¹³ and theory¹⁴ study suggest *d*-wave pairing for single layer FeSe/STO. For *d*-wave superconductivity, it has been shown that antiphase scattering could induce gap reduction near the film edge (Figs. 4.6a,c) as discussed in Chapter 3. Reducing the width, multiplied antiphase scattering between the two close edges will further suppress superconductivity in narrow ribbons (Fig. 4.6b). Our observed critical ribbon width range of 7.2 nm is about twice the scale (~ 3.5 nm from Chapter 3) that the edge scattering effect starts to diminish the superconducting gap in single layer FeSe, hence consistent with the scenario of suppression of superconductivity by antiphase edge scattering under *d*-wave pairing. Note that the V-shaped regime is wider than the superconducting coherence length (3.2 nm¹⁵), thus cannot be explained by the phase slips for 1D nanowires¹⁶.

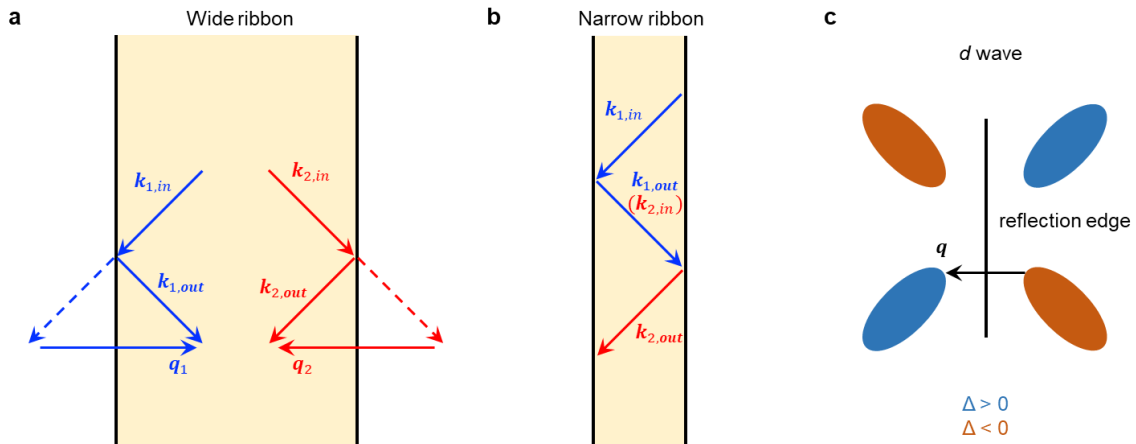


Figure 4.6 a, Edge scattering in a wide FeSe nanoribbon. The q vector is always perpendicular to the edge. **b**, Multiplied edge scattering in a narrow FeSe nanoribbon. **a**, Antiphase scattering on the edge for *d* wave pairing. The vertical black line represents the reflection edge. The ellipses

represent the gap structure and the two colors indicate the two signs (blue is positive and brown is negative) of the order parameter.

4.3 Summary

In summary, we have epitaxially synthesized high-temperature superconducting single layer FeSe nanoribbons with well-defined width from a few to several tens of nanometers on SrTiO₃(001) substrates. dI/dV spectra taken on different ribbons can be classified to 3 types by the lineshape: the superconducting gap, the V shape and the U shape. These 3 types of spectra suggest 3 different phases as a function of the ribbon width. Wide FeSe ribbons (width larger than 7.2 nm) are in the gap regime under superconducting phase. Reducing the width that two edges of the ribbon are close enough to induce multiplied antiphase scattering, the pair breaking effect will strongly suppress the superconductivity and destroy the coherence peaks in the tunneling spectrum. This is the V shape regime for ribbons between 5.0 and 7.2 nm, and here the normal state still preserves. Further reducing the ribbon width to below 5 nm, quantum well states dominate the band structure and the normal state is changed, resulting in the U shape regime. Our work, for the first time, determines the critical superconducting FeSe ribbon width and highlights the critical role dimensionality plays in high-temperature superconductivity.

References

- 1 Anderson, P. W. Theory of dirty superconductors. *Journal of Physics and Chemistry of Solids* **11**, 26-30 (1959).
- 2 Braun, F. & von Delft, J. Superconductivity in ultrasmall metallic grains. *Physical Review B* **59**, 9527-9544 (1999).
- 3 Sangita, B. & Pushan, A. A review of finite size effects in quasi-zero dimensional superconductors. *Reports on Progress in Physics* **77**, 116503 (2014).
- 4 Kubo, R., Kawabata, A. & Kobayashi, S. Electronic Properties of Small Particles. *Annual Review of Materials Science* **14**, 49-66 (1984).
- 5 Bezryadin, A., Lau, C. N. & Tinkham, M. Quantum suppression of superconductivity in ultrathin nanowires. *Nature* **404**, 971 (2000).
- 6 Zgirski, M., Riikonen, K.-P., Touboltsev, V. & Arutyunov, K. Size Dependent Breakdown of Superconductivity in Ultranarrow Nanowires. *Nano Letters* **5**, 1029-1033 (2005).
- 7 Paglione, J. & Greene, R. L. High-temperature superconductivity in iron-based materials. *Nature Physics* **6**, 645 (2010).
- 8 Stewart, G. R. Superconductivity in iron compounds. *Reviews of Modern Physics* **83**, 1589-1652 (2011).
- 9 Wang, Q.-Y. *et al.* Interface-Induced High-Temperature Superconductivity in Single Unit-Cell FeSe Films on SrTiO₃. *Chinese Physics Letters* **29**, 037402 (2012).
- 10 Li, Z. *et al.* Visualizing superconductivity in FeSe nanoflakes on SrTiO₃ by scanning tunneling microscopy. *Physical Review B* **91**, 060509 (2015).
- 11 He, S. *et al.* Phase diagram and electronic indication of high-temperature superconductivity at 65 K in single-layer FeSe films. *Nature Materials* **12**, 605 (2013).
- 12 Zhi, L. *et al.* Molecular beam epitaxy growth and post-growth annealing of FeSe films on SrTiO₃: a scanning tunneling microscopy study. *Journal of Physics: Condensed Matter* **26**, 265002 (2014).
- 13 Zhang, Y. *et al.* Superconducting gap anisotropy in monolayer FeSe thin film. *Physical Review Letters* **117**, 117001 (2016).
- 14 Agterberg, D. F., Shishidou, T., O'Halloran, J., Brydon, P. M. R. & Weinert, M. Resilient nodeless *d*-Wave superconductivity in monolayer FeSe. *Physical Review Letters* **119**, 267001 (2017).
- 15 Fan, Q. *et al.* Plain s-wave superconductivity in single-layer FeSe on SrTiO₃ probed by scanning tunneling microscopy. *Nature Physics* **11**, 946 (2015).
- 16 Arutyunov, K. Y., Golubev, D. S. & Zaikin, A. D. Superconductivity in one dimension. *Physics Reports*, **464**, 1-70 (2008).

Chapter 5 Superconductivity on Edge: One-dimensional Superconducting Channel on the Edge of Antiferromagnetic Single Layer FeTeSe Nanoribbons

5.1 Introduction

Superconductivity normally emerges only as the static antiferromagnetic (AFM) order is suppressed in Fe-based superconductors¹⁻³. The parent compound of iron chalcogenides, FeTe, consists of quasi-planar Te-Fe-Te trilayers (space group: $P4/nmm$) with a square lattice of iron (2 Fe atoms in the crystallographic cell) in tetragonal coordination to tellurium⁴. This trilayer is the common building block for all Fe-based superconductors, and it is widely believed the interactions leading to high-temperature superconductivity originate from the Fe atoms within the layer^{2,3}. Bulk FeTe crystal at ambient conditions also exhibits a distinct long-range bicollinear AFM ordering⁵⁻⁹, with Fe moments ferromagnetically aligned along one diagonal direction of the Fe sublattice and antiferromagnetically along the other. Alloying with Se suppresses the bicollinear AFM order and superconductivity emerges with T_c of 10 K at a critical Se concentration of $x = 0.3$ ^{10,11}. This phase transition can be further manipulated by reducing the thickness of FeTe_{1-x}Se_x to a single atomic layer. Recent work has shown an increase of T_c to 50 K in epitaxial single layer FeTe_{1-x}Se_x grown on STO substrates at an even lower critical Se concentration of $x = 0.1$ ¹². Despite those advances, how superconductivity emerges when the bicollinear AFM is suppressed in FeTe_{1-x}Se_x is still unknown.

Here, we explore the effect of dimensionality on the interplay between magnetic ordering and superconductivity by investigating nanoribbons of single layer $\text{FeTe}_{1-x}\text{Se}_x$ films. Scanning tunneling microscopy/spectroscopy reveals a 2 nm wide 1D superconducting channel on the edge of the ribbons, where their bulk exhibits bicollinear AFM order and is not superconducting. Tunneling spectroscopy shows an edge superconducting gap of 12 meV, and its temperature dependence indicates a superconducting transition temperature of 40 K. This superconducting channel can be suppressed for ribbons with width below 10 nm, likely due to quantum size effects. DFT calculations suggest that both alloying with Se and the presence of the edge destabilize the ordered BCL magnetic phase, resulting in a paramagnetic region near the edge with strong checkerboard fluctuations and an electronic structure similar to that of single layer FeSe that is conducive to the superconductivity.

5.2 Results and Discussion

Four single layer $\text{FeTe}_{1-x}\text{Se}_x$ ($0 \leq x \leq 1$) films were grown on $\text{SrTiO}_3(001)$ substrates by molecular beam epitaxy (MBE) in an ultrahigh vacuum system with a base pressure below 1.0×10^{-10} Torr. Fe flux was provided by electron beam evaporation and Se and Te were from Knudsen cells. Se(Te) concentration is tuned by adjusting the Se(Te) evaporating temperature. All the films followed a layer-by-layer growth mode with a 0.2 monolayers per minute growth rate. Nb-doped STO (001) (0.5%wt) substrates were first annealed at 950 °C for 30 min to produce an atomically flat surface. The FeSe film was grown under Se-rich condition ($T_{\text{Se}} = 95$ °C, Fe/Se: 1/10 to 15), and was post annealed at 650 °C for 10 hours to produce FeSe nanoribbons. The FeTe film was grown under Te-rich condition ($T_{\text{Te}} = 255$ °C, Fe/Te: 1/5 to 10),

and then annealed at 450 °C for 4 hours to produce partially covered single layer FeTe flakes. The $\text{FeTe}_{1-x}\text{Se}_x$ ($x < 0.1$) film was grown under Se-lack and Te-rich condition ($T_{\text{Se}} = 80$ °C, $T_{\text{Te}} = 262$ °C, Fe/Se/Te: 1/1/10 to 15), and the $\text{FeTe}_{1-x}\text{Se}_x$ ($x > 0.1$) film was grown under Se-rich and Te-rich condition ($T_{\text{Se}} = 95$ °C, $T_{\text{Te}} = 262$ °C, Fe/Se/Te: 1/(10 to 15)/(10 to 15)). Both the $\text{FeTe}_{1-x}\text{Se}_x$ ($x < 0.1$) and the $\text{FeTe}_{1-x}\text{Se}_x$ ($x > 0.1$) films were post annealed first at 450 °C for 5 hours and then at 650 °C for 10 hours to produce nanoribbons. It is challenging to determine the exact Se concentration due to post growth annealing, which typically induces the substitution of Te with Se. STM/STS measurements were conducted in an ultrahigh vacuum system with a base pressure of 2.0×10^{-11} Torr, which is directly connected to the MBE growth chamber. Electrochemically etched polycrystalline W tips, or mechanically sharpened Pt tips were used for STM imaging at room temperature and liquid helium temperature with the bias voltage applied to the sample. Tunneling spectra were taken at 6 K with a lock-in amplifier (at bias modulation of 0.4 mV at 860 Hz).

The as-grown $\text{FeTe}_{1-x}\text{Se}_x$ films are conformal to the step-terrace morphology of the STO substrates (Fig. 5.1). They are not superconducting, likely due to the presence of excess Se as a result of Se-rich growth conditions^{13,14}. The films were then extensively annealed at 450 °C to induce superconductivity. Afterwards, the samples are annealed at higher temperatures (e.g., 650 °C) to produce different types of edges at: 1) $\text{FeTe}_{1-x}\text{Se}_x$ steps, and 2) trench-like grain boundaries (GBs) (Figs. 5.2a-d).

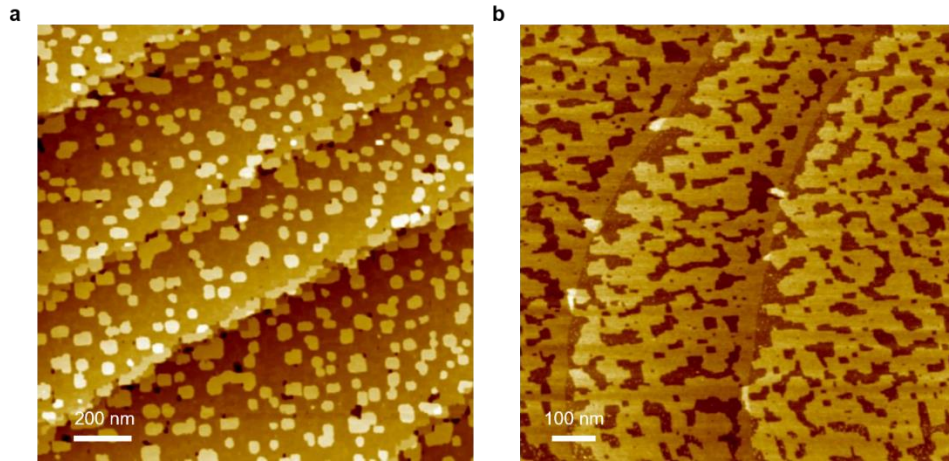


Figure 5.1 **a**, STM image of the as-grown $\text{FeTe}_{1-x}\text{Se}_x$ ($x < 0.1$) film ($V_s = 1.0$ V, $I_t = 0.1$ nA). **b**, STM image of the $\text{FeTe}_{1-x}\text{Se}_x$ ($x < 0.1$) film after annealing at ~ 450 °C for 5 hours ($V_s = 1.0$ V, $I_t = 0.1$ nA). 10 more hours annealing at ~ 650 °C will result in nanoribbons as in Fig. 5.2b.

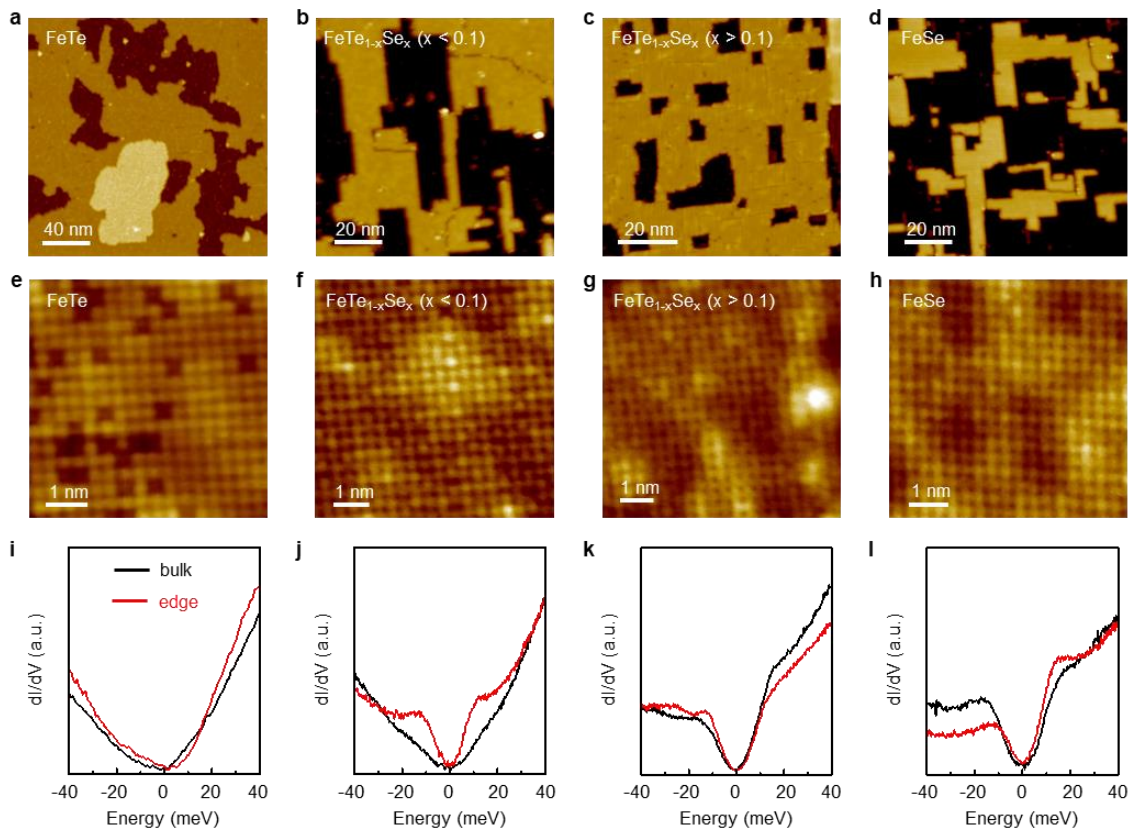


Figure 5.2 a-d, STM images of partially covered single layer FeTe, FeTe_{1-x}Se_x ($x < 0.1$), FeTe_{1-x}Se_x ($x > 0.1$) and FeSe films ($V_s = 1.2$ V, $I_t = 0.1$ nA). There is a 2nd layer FeSe island in **a**. **e-h**, Atomic resolution images on FeTe ($V_s = -0.5$ V, $I_t = 0.1$ nA), FeTe_{1-x}Se_x ($x < 0.1$) ($V_s = 50$ mV, $I_t = 0.1$ nA), FeTe_{1-x}Se_x ($x > 0.1$) ($V_s = 50$ mV, $I_t = 0.1$ nA) and FeSe ($V_s = 50$ mV, $I_t = 0.1$ nA). **i-l**, dI/dV spectra taken at 6 K in the bulk (black curves) and on the edge (red curves) of the four monolayer FeTe, FeTe_{1-x}Se_x ($x < 0.1$), FeTe_{1-x}Se_x ($x > 0.1$) and FeSe.

As shown in the atomic resolution images in Figs. 5.2e-h, a (1x1) structure is apparent for all Se concentrations, with the exception of the second case FeTe_{1-x}Se_x with $x < 0.1$, where additional (2x1) ordering can also be observed at different bias, as discussed in more details below. There are also other notable differences between these films. For example, the FeTe film exhibits a number of vacancies (likely Te) (Fig. 5.2e), while the FeSe film is more uniform (Fig. 5.2h).

The electronic properties of the FeTe_{1-x}Se_x films are further probed by dI/dV tunneling spectroscopy. In the case of FeTe, dI/dV spectra taken in the bulk of the ribbons and near the edges are both V-shaped, with no gaps at the Fermi level (Fig. 5.2i). For Se concentrations larger than 10%, both the bulk and edge are gaped (Figs. 5.2k,l): for FeSe, 18 ± 2 and 13 ± 2 meV, and for FeTe_{1-x}Se_x ($x > 0.1$), 15 ± 2 and 13 ± 2 meV, respectively. The bulk gap values are consistent with earlier works^{13,14}, and the reduced gap at the edge has been attributed to antiphase scattering in Chapter 3. Interestingly, for FeTe_{1-x}Se_x films with Se concentration below 10%, while the film itself is not gaped in the bulk, a robust 1D superconducting channel is observed along the edges, whose properties and possible mechanisms are discussed below. Our ARPES measurement (Fig. 5.3) confirms that the FeTe_{1-x}Se_x ($x > 0.1$) film has a superconducting FeSe-like electron pocket at M point and hole pocket below the Fermi level at Γ point¹⁵⁻¹⁷, while the band structure of the

FeTe_{1-x}Se_x ($x < 0.1$) film is more non-superconducting FeTe-like, with no features at M point but a hole-like band at Γ point^{18,19}.

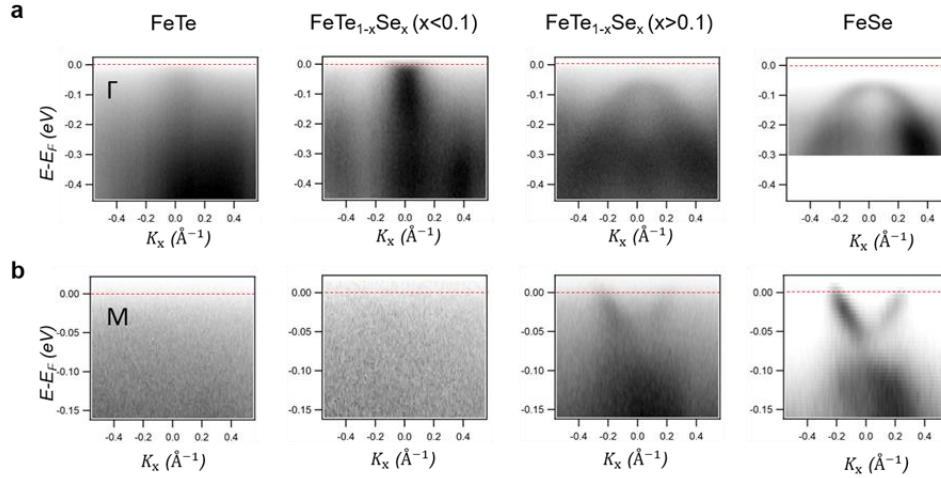


Figure 5.3 a,b, Evolution of the ARPES intensity plot near Γ and M for single layer FeTe_{1-x}Se_x/STO ($0 \leq x \leq 1$) at 80 K. The dashed red lines mark the Fermi level.

Figure 5.4a shows an atomic resolution STM image of an FeTe_{1-x}Se_x ($x < 0.1$) ribbon with a step edge on the left decorated with bright features. Within the bulk of the ribbon multiple (2x1) domains are evident with the domain boundaries, as marked by dashed white lines. Different domains are shifted by one Te/Se atom row, indicated by the red and blue arrows. Similar domain boundaries have been observed on the surface of multilayer epitaxial FeTe films on STO²⁰ and Fe_{1+y}Te_{0.9}Se_{0.1} crystals²¹, and, as discussed below, are likely correlated with BCL magnetic domains. Near the edges within 2-3 atomic rows, bright features are seen along the edges, likely due to defects such as missing atoms²², leading to a disordered (2x1) structure. Similarly, at trench-like grain boundaries (Fig. 5.4b), disordered (2x1) structures are also seen. At the right grain, where the (2x1) is parallel to the edge, the edge structure is more disordered

than that on the left with the (2x1) perpendicular to the edge, where the (2x1) ordering extends almost to the outermost atomic row.

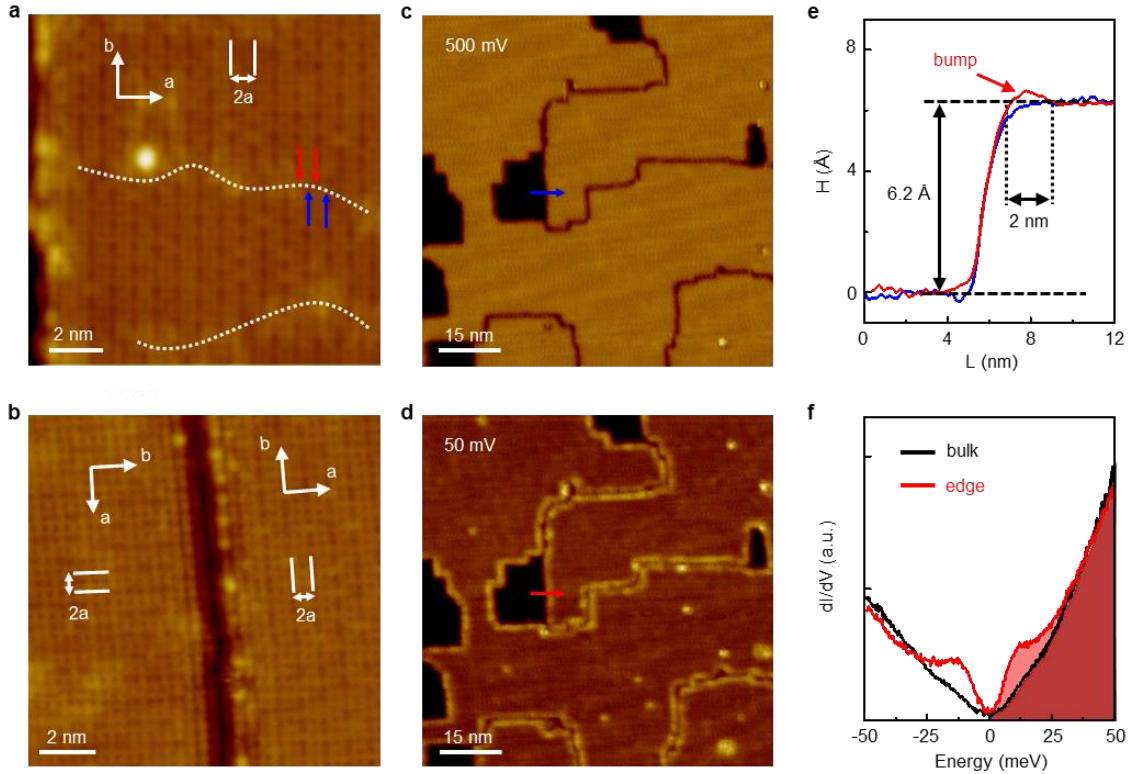


Figure 5.4 **a**, Atomic resolution STM image of a ribbon edge ($V_s = -50$ mV, $I_t = 0.7$ nA). The dashed lines are domain boundaries between two domains with one lattice shift, marked by the red and blue arrows. **b**, STM image of a trench-like GB ($V_s = -50$ mV, $I_t = 0.5$ nA). The 2x1 patterns of the left and right grains are rotated by 90 degrees. **c**, STM image on the annealed $\text{FeTe}_{1-x}\text{Se}_x$ ($x < 0.1$) film, showing both type of edges ($V_s = 500$ mV, $I_t = 0.1$ nA). **d**, STM image of the same location as in **c**, but at a different bias ($V_s = 50$ mV, $I_t = 0.1$ nA). **e**, Line profiles along lines marked by two arrows in **c** & **d**. **f**, dI/dV spectra taken in the bulk (black) and on the edge (red) of a ribbon at 6K. The shadow area indicates larger integrated density of states on the edge (red area) than that of in the bulk (dark area).

All the edges exhibit similar electronic structures, as shown in the STM images in Figs. 5.4c,d taken at different bias voltages. At 500 mV above the Fermi level (Fig. 5.4c), both types of edges appear featureless, and at 50 mV above (Fig. 5.4d), the edges appear bright. The appearance of the edge channel not only depends on the bias voltage, but is also sensitive to the set-point used (Fig. 5.5), where a smaller set-point (larger tip-sample distance) yields greater contrast at the edges, at the expense of reduced atomic resolution.

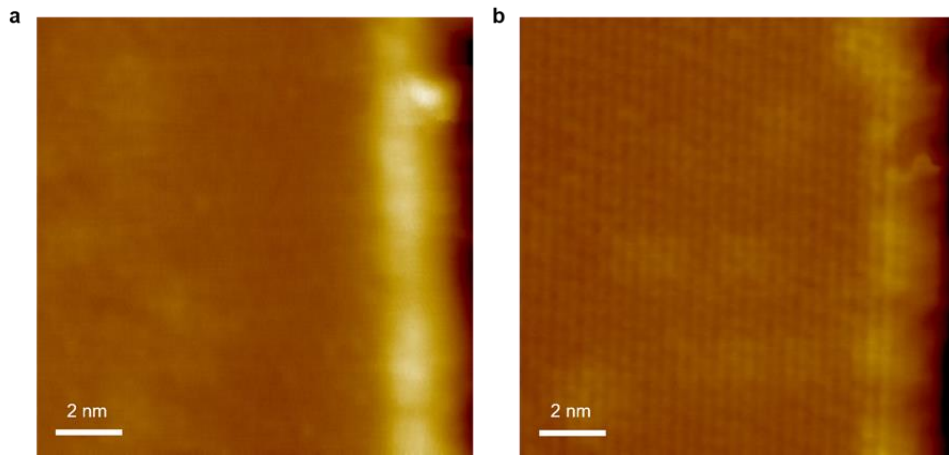


Figure 5.5 a, STM image of the $\text{FeTe}_{1-x}\text{Se}_x$ ($x < 0.1$) ribbon-to-STO edge ($V_s = 50$ mV, $I_t = 0.1$ nA). The edge is on the very right. **b**, STM image of the same edge as in **a**, but with a larger scanning current setpoint ($V_s = 50$ mV, $I_t = 0.2$ nA).

Line profiles across the same edge marked by the arrows in Figs. 5.4c,d are presented in Fig. 5.4e. Both profiles show a 2 nm transitional region before the profile reaches the “bulk” value: a 2 nm “bump” for 50 mV where the edge appears bright, and a ~ 2 nm “uptake” for the 500 mV where the edge appears dark, indicating an edge channel width of ~ 2 nm. More detailed analysis of the bias dependent imaging shows that this edge contrast remains up to ± 100 mV, independent of the bias polarity (Fig. 5.6). As the contrast in STM imaging reflects the difference in the integrated local density of states (LDOS), Fig. 5.4d illustrates that the integrated LDOS

from the Fermi level to the applied bias (the area below the dI/dV curve from the Fermi level to the bias voltage) is larger on the edge (the red area) than in the bulk (the black area) when the bias is smaller than 50 mV in magnitude.

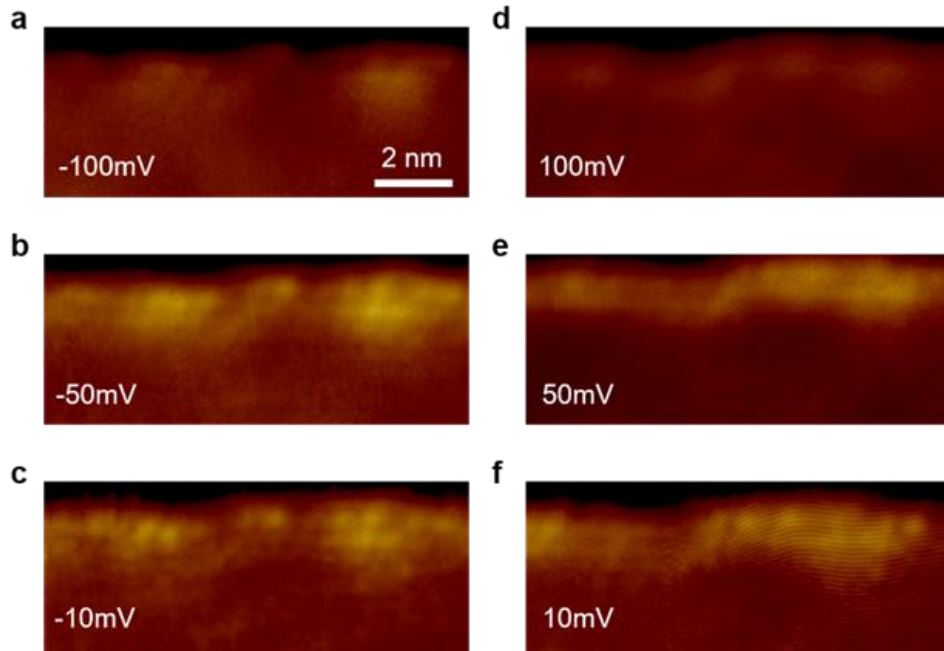


Figure 5.6 a-d, STM images of the same $\text{FeTe}_{1-x}\text{Se}_x$ ($x < 0.1$) ribbon edge at different biases as marked in the images.

The contrasting electronic property for the edge and bulk is further confirmed by spatially resolved tunneling spectra taken at 6 K, as shown in Fig. 5.7a. The spatially dependent dI/dV spectra taken perpendicular to the edge show well-defined gap and coherence within 2 nm of the edge, consistent with the width of the bright edge channel in the STM image (c.f., Figs. 5.4d,e).

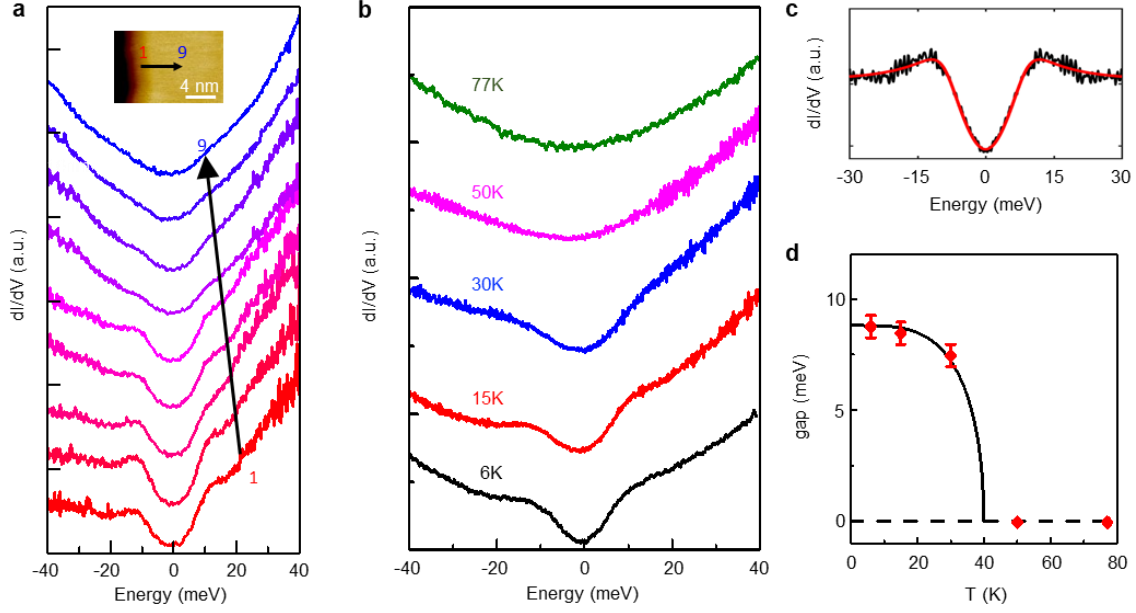


Figure 5.7 a, Spatially resolved dI/dV taken along a line marked as a black arrow in the inset. The starting point 1 (red) is on the edge and the ending point 9 (blue) is in the bulk. The inset is an STM image of a $\text{FeTe}_{1-x}\text{Se}_x$ ($x < 0.1$), showing the ribbon edge ($V_s = 600$ mV, $I_t = 70$ pA). **b**, dI/dV spectra taken on the ribbon edges at temperatures indicated. **c**, s -wave Dynes function fitting of normalized dI/dV spectrum at 6 K in **b**. Black curve is the processed data, and red curve is the Dynes function fitted with $\Gamma = 4.6$ meV, $\Delta = 8.8$ meV. **d**, Fitting the superconducting gaps from the Dynes function fitting (red diamond) to the BCS theory (black line) indicates a superconducting transition temperature of 40 K.

The superconducting nature of the observed edge gap is confirmed by temperature-dependent dI/dV measurements as shown in Fig. 5.7b. The gap can be defined up to 30 K, and beyond 50 K the spectra are mostly V-shaped. Figure 5.7c shows the s -wave Dynes function²³

$$dI/dV = \text{Re} \left[(eV - i\Gamma) / \sqrt{(eV - i\Gamma)^2 - \Delta^2} \right]$$

fitting of the background subtracted dI/dV spectrum shown in Fig. 5.7b (details of data processing²⁴ are in Fig. 5.8). With fitting parameters

$\Gamma = 4.5$ meV and $\Delta = 8.8$ meV, excellent fits to the Dynes function are found, strongly suggesting that the gaps in the dI/dV spectra taken near the edge of single layer $\text{FeTe}_{1-x}\text{Se}_x$ ($x < 0.1$) ribbons originate from superconducting pairing. This is further supported by fitting the temperature dependent gap to BCS theory²⁵ (Fig. 5.7d), yielding a superconducting transition temperature of 40 K, which is the T_c record of 1D superconductivity²⁶.

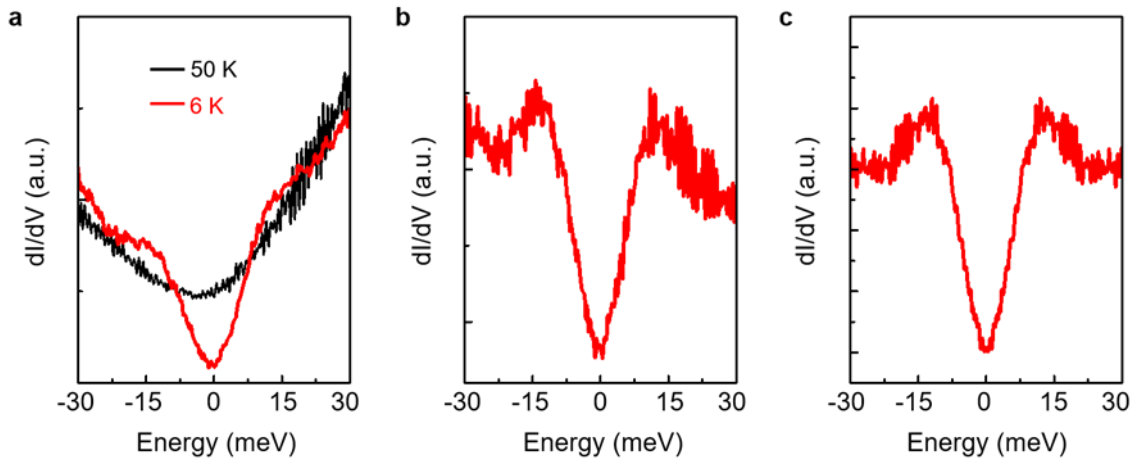


Figure 5.8 a, Raw dI/dV spectra taken on the $\text{FeTe}_{1-x}\text{Se}_x$ ($x < 0.1$) ribbon edge at 6 K (red curve, below T_c) and 50 K (black curve, above T_c). **b**, Background correction. dI/dV spectrum taken at 6 K in **a** divided by the spectrum taken at 50 K in **a**. **c**, Symmetrization. Average of the spectrum from **b** and its mirror with respect to zero bias.

To examine the impact of ribbon width on this superconducting channel, dI/dV tunneling spectroscopy was conducted on four $\text{FeTe}_{1-x}\text{Se}_x$ ($x < 0.1$) ribbons with widths of 3.2, 8.6, 10.0, and 20.0 nm, as shown in Fig. 5.9. For ribbons width greater than 10 nm (Figs. 5.9c,d,g,h), well-defined superconducting gaps are seen at the edges while the bulk spectra are V-shaped, similar to those discussed above (c.f., Fig. 5.4f). At a critical width of 8.6 nm however, both ribbon edge and bulk exhibit V-shaped spectra, indicating that edge superconductivity is suppressed (Fig. 5.9b,f), likely due to quantum size effects²⁷ and as discussed in Chapter 4. This is consistent with

the observation of significantly diminished density of states for a ribbon with 3.2 nm width (Fig. 5.9a,e).

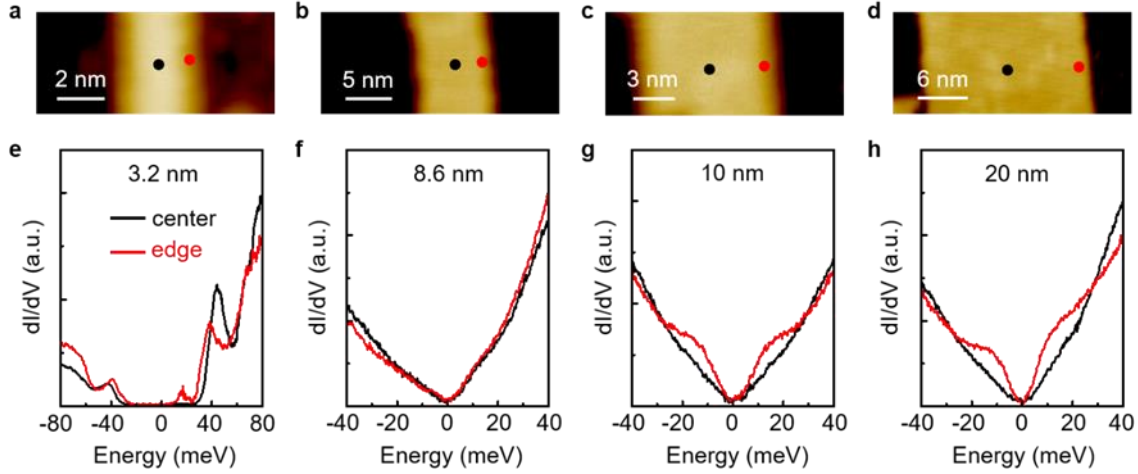


Figure 5.9 a-d, STM images of $\text{FeTe}_{1-x}\text{Se}_x$ ($x < 0.1$) nanoribbons of 3.2 nm, 8.6 nm, 10 nm and 20 nm, respectively ($V_s = 1.2$ V, $I_t = 0.1$ nA). **e-h**, dI/dV spectra taken in the center (marked by black dots) and near the edge (red dots), marked by the black and red dots, respectively in **a-d**.

To gain insight into the observed superconductivity at the edge of $\text{FeTe}_{1-x}\text{Se}_x$ ($x < 0.1$) ribbons but not in the bulk, we first calculate the changes in the electronic (and magnetic) properties of single layer $\text{FeTe}_{1-x}\text{Se}_x$ films with Se concentration by DFT. For pure FeSe/STO , our recent calculations indicate a ground state of frustrated paramagnetic phase characterized by the checkerboard (CB) quantum fluctuations²⁸. Thus, the competition between the CB and BCL configurations is calculated for unsupported and STO-supported $\text{FeTe}_{1-x}\text{Se}_x$ monolayers for 0, 6.25, and 12.5% Se (Fig. 5.10a). For pure FeTe , the BCL is favored by 17.2 meV/Fe for the free monolayer, which decreases to 9.3 meV/Fe when the monolayer is supported on STO. At 6% Se, these differences decrease to 10.1 and 2.8 meV/Fe, respectively; for 12.5% Se for the STO-supported layer, the CB configuration is now more stable than the BCL by 3.6 meV/Fe. (For

calculations neglecting SOC, the CB is additionally favored by 3-4 meV/Fe.) The DFT results suggest that around 10% Se, the STO-supported monolayer BCL phase will be destabilized in favor of a paramagnetic phase with strong CB fluctuations²⁸, resulting in an electronic structure similar to that of FeSe which is conducive to superconductivity, consistent with our experimental observations (c.f., Fig. 5.2). (As is the case also for FeSe, the stripe collinear phase is calculated to be lower in energy, which is both consistent and necessary²⁸ for the system to be in the frustrated paramagnetic phase characterized by CB quantum fluctuations.)

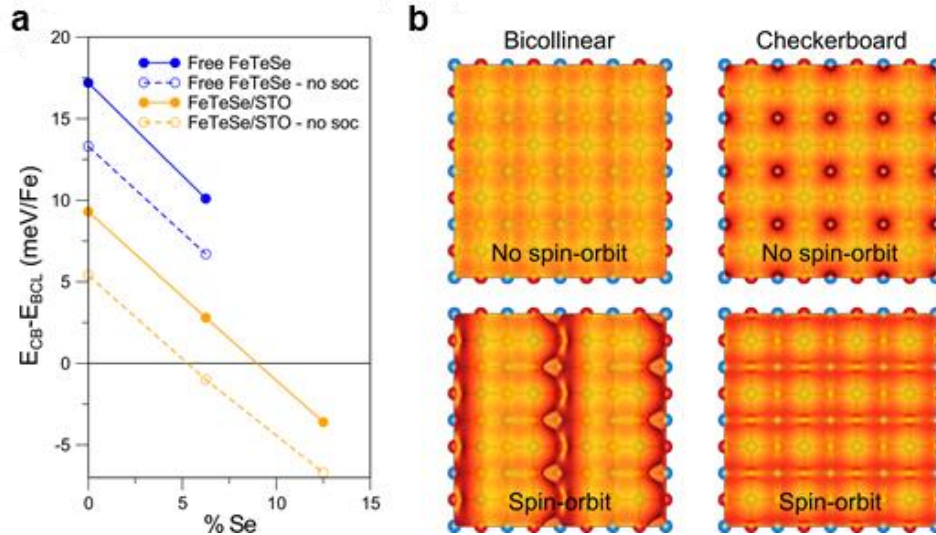


Figure 5.10 a, Calculated energy difference between the CB and BCL structures as a function of Se concentration for free and STO-supported $\text{FeTe}_{1-x}\text{Se}_x$ layers, both with and without spin-orbit. The critical concentrations for both bulk and unsupported $\text{FeTe}_{1-x}\text{Se}_x$ are greater than for the monolayer on STO. **b**, Simulated constant current STM images ($10^{-5} e/\text{\AA}^3$ isosurface of occupied states, 0.5 eV bias) for FeTe in the BCL and CB configurations, with and without spin-orbit coupling. Red (blue) balls represent Fe (Te) atoms.

The significant differences in the electronic structure of the BCL and CB magnetic configurations are reflected in the STM images. Simulated (constant current) STM images of

FeTe (Fig. 5.10b) for the BCL agree with the same (2x1) structure observed in the experiments (Figs. 5.4a,b). The (2x1) structure is not related to atomic distortions, but rather is a consequence of the combination of magnetic configuration and spin-orbit coupling (SOC); while the possible connection between the (2x1) pattern and the BCL ordering has been made previously^{8,20,24}, the essential role played by SOC has not been appreciated. Simulated images that use the identical atomic structure, but do not include SOC, show a (1x1) pattern (Fig. 5.10b). This simulation confirms that the BCL magnetic phase induced (2x1) ordering in FeTe detectable by normal STM imaging (a spin-polarized tip is not necessary), consistent with earlier work^{8,12,20}. For 6% Se doped single layer FeTe, which mimics the case of our FeTe_{1-x}Se_x ($x < 0.1$) ribbon bulk, the simulated STM image shows a (2x1) pattern (Fig. 5.11a), consistent with the STM images (Figs. 5.4a,b). Thus, the meandering domain boundaries in Fig. 5.4a are magnetic in nature (Fig. 5.11b), rather than structural grain boundaries.

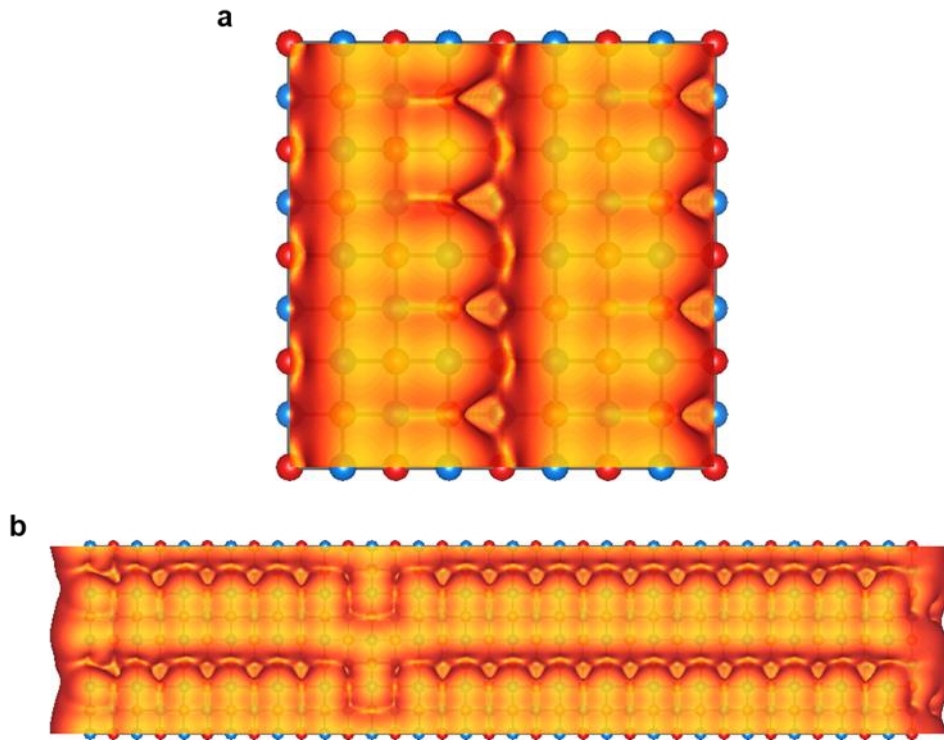


Figure 5.11 a, Simulated STM for the 6% Se monolayers, with bicollinear AFM order and corresponding 2x1 pattern. Red atoms are Fe, blue Te (yellow Se). **b**, FeTe perpendicular bicollinear ribbon with spin defect. Spin defects give rise to shifts in lines. The experimental “domain boundaries” in the 2x1 regions (Figs. 5.4a,b) are likely shifts in spins, not actual atomic shifts. This also is a simpler explanation of why the boundary is not straight across the ribbon.

Although these results suggest a switch from a magnetically BCL ordered phase to one with CB-like electronic (superconducting) behavior similar to FeSe with increasing Se concentration, additional effects are needed to account for the observed superconductivity at the $\text{FeTe}_{1-x}\text{Se}_x$ ($x < 0.1$) ribbon edge but not in the bulk. The experimental results suggest that the superconductivity in this case (for $x < 0.1$) is limited to within 2 nm from the edge. To address this possibility, we consider 6.8 nm FeTe ribbons and compare the relative energies of different magnetic configurations. (We limit these calculations to pure FeTe for computational simplicity.) For 2 nm CB regions along the edges, the energy difference between the BCL and CB phases decreases significantly to 5.4 meV/Fe (from 17.2 meV/Fe) for BCL stripes parallel to the edge (c.f., the right domain in Fig. 5.4b). Figure 5.12a is a simulated STM image for an FeTe ribbon with BCL ordering in the bulk (parallel to the edge) and CB-AFM on the edge (2 nm). (For BCL stripes perpendicular to the edge, the reduction is only 1-2 meV/Fe, reflecting the different interfaces between the phases and suggesting that the BCL region will extend closer to the edge in this case, consistent with Fig. 5.4b. A simulated STM image is shown in Fig. 5.13a.) Thus, near the edge the BCL phase (for stripes running parallel to the edge) is destabilized relative to the CB. These calculations for FeTe, together with results for different Se concentrations, indicate that the edge of $\text{FeTe}_{1-x}\text{Se}_x$ ribbons with Se concentrations less than 10% will exhibit the

CB-like electronic structure – and can be superconducting – while the bulk of the ribbon remains in the BCL magnetic phase.

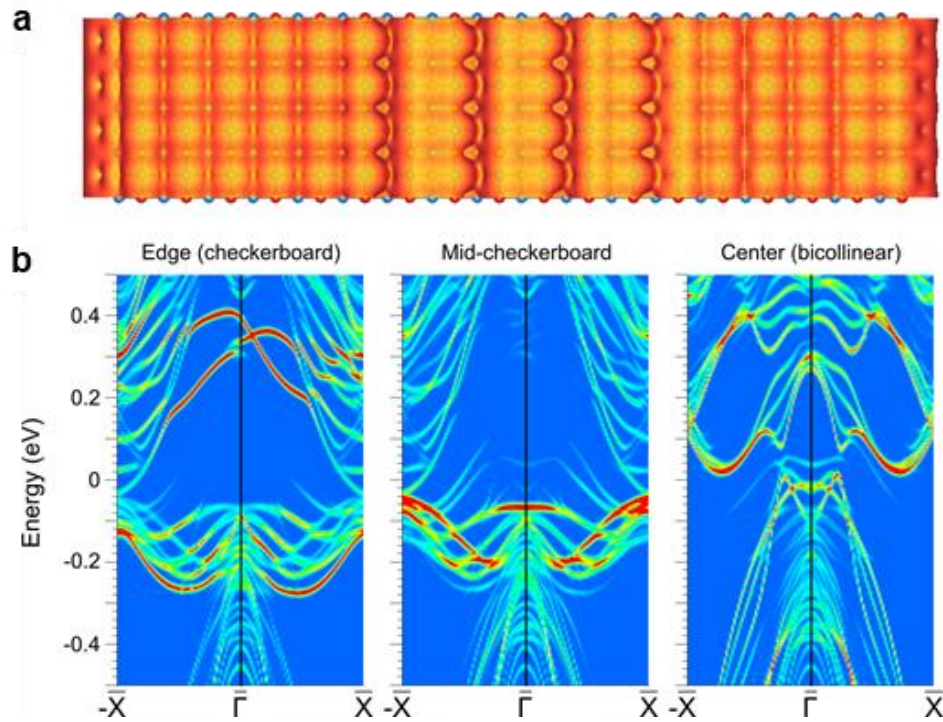


Figure 5.12 a, Simulated FeTe ribbon with bicollinear AFM in the bulk (parallel to the edge) and checkerboard AFM on the edge (2 nm). **b**, k -projected local bands of FeTe ribbon with bicollinear AFM in the bulk (parallel to the edge) at different locations. The middle panel is 1 nm in from the edge. The weighting is over the whole thickness of the ribbon, not in the vacuum region probed by the STM/STS tip.

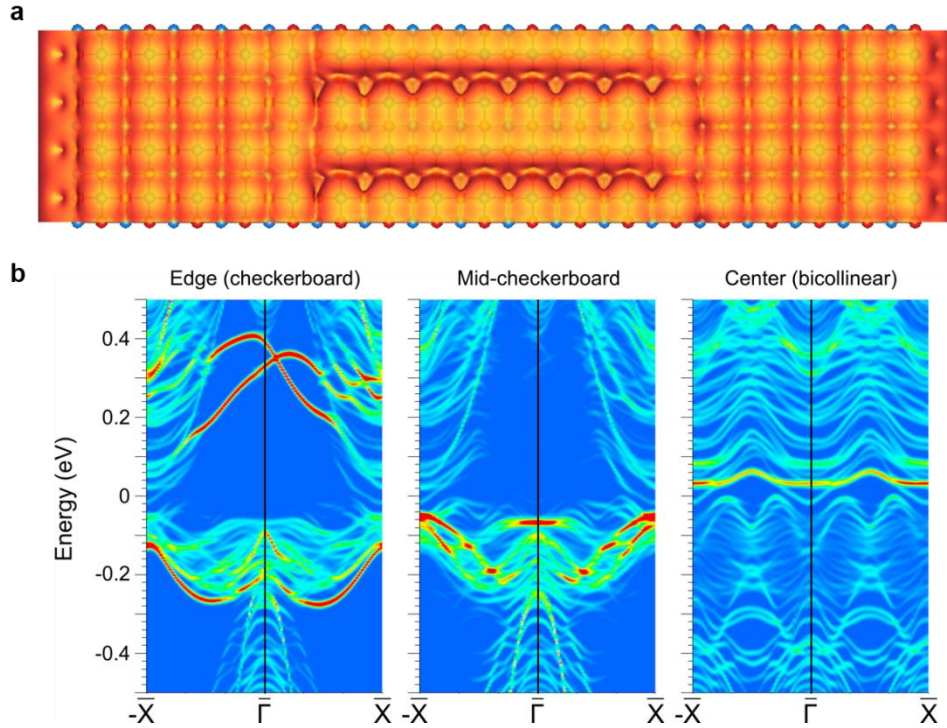


Figure 5.13 a, Simulated FeTe ribbons with bicollinear AFM in the bulk (perpendicular to the edge) and checkerboard AFM on the edge (2 nm). **b**, k -projected local bands of FeTe ribbon with bicollinear AFM in the bulk (perpendicular to the edge) at different locations. Similar to Fig. 5.12b, but for rotated magnetic order. The bulk bicollinear looks different, but it is simply because the ribbon projection is rotated. The color scheme is the same for all the different panels. Especially for the edge states, k and $-k$ are different because of the broken time reversal.

The k -resolved local electronic bands for BCL parallel to the edge are shown in Fig. 5.12b (bands for BCL perpendicular to the edge are shown in Fig. 5.13b). The bands in the CB region near the edge of the FeTe ribbon closely resemble the projected bands of a FeSe monolayer on STO: electron pockets derived from M and no Fermi surface around the center of the zone¹⁵⁻¹⁷. (In the ribbon geometry, Γ -X projects to Γ , and X-M project to X.) In the region near the edge, there are edge states that still have weight 1 nm from the edge. In the BCL region,

the bands have the characteristic features and dispersions for the bands along the FM direction of the stripes. The picture that emerges from these calculations is that both Se doping and the presence of the edge destabilize the ordered BCL magnetic phase, resulting in a paramagnetic region near the edge with strong CB fluctuations that locally lead to an FeSe-like electronic structure conducive to the superconductivity. Therefore, even though the Se concentration is inadequate (less than 10%) to induce bulk superconductivity in single-layer $\text{FeTe}_{1-x}\text{Se}_x$ ribbon, the presence of edge suppresses the BCL sufficiently that it becomes superconducting.

DFT calculations were done using the Full-potential Linearized Augmented Plane Wave (FLAPW) program *flair*²⁹ and the Vienna ab initio simulation package (VASP)^{30,31}. The in-plane constant was fixed to that of $\text{SrTiO}_3(001)$, 3.9052 Å. 4x4 supercells were used to address the Se doping; calculations for the STO substrate were modeled by a symmetric TiO_2 -terminated SrTiO_3 slab with $\text{FeTe}_{1-x}\text{Se}_x$ layers on both sides. A 15 Å vacuum region separated images. Additionally, the 6.8 nm FeTe ribbons had a 13.7 Å vacuum region between edges. The Te/Se heights were relaxed, and spin-orbit coupling was included except as noted. The calculations used k-point meshes equivalent to 40x40 Monkhorst-Pack for the 1x1 cell, and the PBE GGA parameterization was used. VASP calculations used a plane wave cutoff of 400 eV, while the FLAPW ones used a 200 (2000) eV cutoff for the wave functions (density/potential).

5.3 Summary

In summary, we have epitaxially grown non-superconducting single layer $\text{FeTe}_{1-x}\text{Se}_x$ ($x < 0.1$) ribbons with well-defined straight ribbon edges on $\text{SrTiO}_3(001)$ substrates. Scanning tunneling microscopy/spectroscopy reveals a 2 nm 1D superconducting channel on the edge of

the ribbons, while the bulk of the ribbons is not superconducting. DFT calculations suggest the emergence of this edge superconductivity is related to the enhanced suppression of bicollinear AFM order near the edge, which destabilizes the ordered BCL magnetic phase, and results in a paramagnetic region with strong checkerboard fluctuations that locally leads to an FeSe-like electronic structure conducive to superconductivity. This work highlights the role of dimensionality in the interplay between superconductivity and magnetism, and demonstrates that nanostructuring can be an effective route towards inducing and enhancing superconductivity in Fe-based superconductors.

References

- 1 Dai, P. Antiferromagnetic order and spin dynamics in iron-based superconductors. *Reviews of Modern Physics* **87**, 855-896 (2015).
- 2 Paglione, J. & Greene, R. L. High-temperature superconductivity in iron-based materials. *Nat. Phys.* **6**, 645-658 (2010).
- 3 Stewart, G. R. Superconductivity in iron compounds. *Reviews of Modern Physics* **83**, 1589-1652 (2011).
- 4 Mizuguchi, Y. & Takano, Y. Review of Fe chalcogenides as the simplest Fe-based superconductor. *Journal of the Physical Society of Japan* **79**, 102001 (2010).
- 5 Fruchart, D. *et al.* Structure antiferromagnétique de Fe_{1.125}Te accompagnée d'une déformation monoclinique. *Materials Research Bulletin* **10**, 169-174 (1975).
- 6 Ma, F., Ji, W., Hu, J., Lu, Z. Y. & Xiang, T. First-principles calculations of the electronic structure of tetragonal α -FeTe and α -FeSe crystals: evidence for a bicollinear antiferromagnetic order. *Phys. Rev. Lett.* **102**, 177003 (2009).
- 7 Bao, W. *et al.* Tunable $(\delta\pi, \delta\pi)$ -type antiferromagnetic order in α -Fe(Te,Se) superconductors. *Phys. Rev. Lett.* **102**, 247001 (2009).
- 8 Enayat, M. *et al.* Real-space imaging of the atomic-scale magnetic structure of Fe_{1+y}Te. *Science* **345**, 653-656 (2014).
- 9 Hänke, T. *et al.* Reorientation of the diagonal double-stripe spin structure at Fe_{1+y}Te bulk and thin-film surfaces. *Nature Communications* **8**, 13939 (2017).
- 10 Liu, T. J. *et al.* From $(\pi,0)$ magnetic order to superconductivity with (π,π) magnetic resonance in Fe_{1.02}Te_{1-x}Se_x. *Nat. Mater.* **9**, 716-720 (2010).
- 11 Kawasaki, Y. *et al.* Phase diagram and oxygen annealing effect of FeTe_{1-x}Se_x iron-based superconductor. *Solid State Communications* **152**, 1135-1138 (2012).
- 12 Li, F. *et al.* Interface-enhanced high-temperature superconductivity in single-unit-cell FeTe_{1-x}Se_x films on SrTiO₃. *Physical Review B* **91**, 220503 (2015).
- 13 Wang, Q. Y. *et al.* Interface-induced high-temperature superconductivity in single unit-cell FeSe films on SrTiO₃. *Chinese Physics Letters* **29**, 037402 (2012).
- 14 Li, Z. *et al.* Molecular beam epitaxy growth and post-growth annealing of FeSe films on SrTiO₃: a scanning tunneling microscopy study. *J. Phys. Condens. Matter.* **26**, 265002 (2014).
- 15 Liu, D. *et al.* Electronic origin of high-temperature superconductivity in single-layer FeSe superconductor. *Nat. Commun.* **3**, 931 (2012).
- 16 Tan, S. *et al.* Interface-induced superconductivity and strain-dependent spin density waves in FeSe/SrTiO₃ thin films. *Nat Mater* **12**, 634-640 (2013).
- 17 Lee, J. J. *et al.* Interfacial mode coupling as the origin of the enhancement of T_c in FeSe films on SrTiO₃. *Nature* **515**, 245-248 (2014).

- 18 Liu, Z. K., *et al.* Measurement of coherent polarons in the strongly coupled antiferromagnetically ordered iron-chalcogenide $\text{Fe}_{1.02}\text{Te}$ using angle-resolved photoemission spectroscopy. *Physical review letters* **110**, 037003 (2013).
- 19 Han, Z. Q., Shi, X., Peng, X. L., Sun, Y. J. & Wang, S. C. High-quality $\text{FeTe}_{1-x}\text{Se}_x$ monolayer films on $\text{SrTiO}_3(001)$ substrates grown by molecular beam epitaxy. *Chinese Physics Letters*, **34**, 107401 (2017).
- 20 Li, W. *et al.* Charge ordering in stoichiometric FeTe: Scanning tunneling microscopy and spectroscopy. *Physical Review B* **93**, 041101 (2016).
- 21 Aluru, R., Zhou, H., Essig, A., Reid, J.P., Tsurkan, V., Loidl, A., Deisenhofer, J. & Wahl, P. Atomic scale coexistence of short-range magnetic order and superconductivity in $\text{Fe}_{1+y}\text{Se}_{0.1}\text{Te}_{0.9}$. *arXiv* 1711.10389 (2017).
- 22 Huang, D. *et al.* Dumbbell defects in FeSe films: a scanning tunneling microscopy and first-principles investigation. *Nano Letters* **16**, 4224-4229 (2016).
- 23 Dynes, R. C., Narayanamurti, V. & Garno, J. P. Direct measurement of quasiparticle-lifetime broadening in a strong-coupled superconductor. *Physical Review Letters* **41**, 1509-1512 (1978).
- 24 Manna, S. *et al.* Interfacial superconductivity in a bi-collinear antiferromagnetically ordered FeTe monolayer on a topological insulator. *Nature Communications* **8**, 14074 (2017).
- 25 Bardeen, J., Cooper, L. N. & Schrieffer, J. R. Theory of superconductivity. *Physical Review* **108**, 1175-1204 (1957).
- 26 Arutyunov, K. Y., Golubev, D. S. & Zaikin, A. D. Superconductivity in one dimension. *Physics Reports*, **464**, 1-70 (2008).
- 27 Li, Z. *et al.* Visualizing superconductivity in FeSe nanoflakes on SrTiO_3 by scanning tunneling microscopy. *Physical Review B* **91** (2015).
- 28 Shishidou, T., Agterberg, D. F. & Weinert, M., Magnetic fluctuations in single-layer FeSe. *Communications Physics* **1**, 8 (2018).
- 29 Weinert, M., Schneider, G., Podloucky, R. & Redinger, J. FLAPW: applications and implementations. *Journal of Physics: Condensed Matter* **21**, 084201 (2009).
- 30 Kresse, G. & Furthmüller, J. Efficient iterative schemes for ab initio total-energy calculations using a plane-wave basis set. *Physical Review B* **54**, 11169-11186 (1996).
- 31 Kresse, G. & Joubert, D. From ultrasoft pseudopotentials to the projector augmented-wave method. *Physical Review B* **59**, 1758-1775 (1999).

Chapter 6 Summary and Outlook

6.1 Summary

The recently discovered single layer FeSe on SrTiO₃ substrate exhibits the highest T_c in the iron-based superconductors family and unique structural and electronic properties different from lots of the already known superconductors. This dissertation research investigates the mechanism of superconductivity and explores tuning factors to modify the superconducting phase.

By tuning the post annealing temperature, we prepared single layer FeSe films on STO with [110]_{Fe} and [100]_{Fe} edges. Spatially resolved tunneling spectra show that the superconducting gap is suppressed on the specular [110]_{Fe} edge, but remains constant on the specular [100]_{Fe} edge. By fitting the gap as a function of position, we obtain a finite and positive superconducting extrapolation length of 8.0 nm on the specular [110]_{Fe} edge and an infinite extrapolation length on the specular [100]_{Fe} edge. Additionally, on the rough [100]_{Fe} edge, superconductivity is also suppressed. The finite extrapolation length on the [110]_{Fe} edge and its edge orientation and roughness dependent behavior is consistent with d wave pairing symmetry in single layer FeSe/STO.

Further increasing the post annealing time and temperature, we prepare single layer FeSe nanoribbon of well-controlled width from a few to tens of nanometers. dI/dV spectra conducted on various ribbons show a ribbon width dependent suppression of superconductivity. For FeSe ribbons wide than 9.0 nm, the tunneling spectra have well-defined superconducting gaps. Between 7.2 to 9.0 nm, the gap can still be defined while the coherence peaks are suppressed.

Below the critical ribbon width of 7.2 nm, Cooper pairs are destabilized. For ribbons between 5.0 and 7.2 nm, the dI/dV spectra are in V shape. Below 5.0 nm, quantum well states dominate the density of states spectra, exhibiting U-shaped spectra. The gap versus ribbon width relation demonstrates that unconventional pairing can be modified by reducing the superconductor size and determines the critical length scale for superconducting FeSe nanoribbons.

By introducing another source Te, we synthesize single layer $\text{FeTe}_{1-x}\text{Se}_x$ ($0 \leq x \leq 1$) films with different Se concentrations on STO. After post annealing, we investigate the tunneling spectra on the edge and in the bulk of different films. As expected, FeTe is not superconducting both on the edge and in the bulk. FeSe and $\text{FeTe}_{1-x}\text{Se}_x$ ($x > 0.1$) is superconducting everywhere on the film. Surprisingly, on single layer $\text{FeTe}_{1-x}\text{Se}_x$ ($x < 0.1$), there is a one-dimensional superconducting channel of 2 nm wide on the edge, while the bulk is non-superconducting. The edge superconductivity is confirmed by the gap closing at raised temperature and Dynes function fitting of the dI/dV spectra. The 2×1 ordering from STM images and DFT simulations suggest the bulk of the $\text{FeTe}_{1-x}\text{Se}_x$ ($x < 0.1$) film is in bicollinear antiferromagnetic phase. DFT calculations further suggest that the film edge helps to destabilize the bicollinear magnetic order and locally induce single layer FeSe-like band structure which is conducive to the superconductivity. This observation demonstrates that nanostructure boundaries can also act as a factor to modify the interplay between magnetism and superconductivity.

6.2 Outlook

6.2.1 Interface Engineering

The STO substrate plays a significant role in the superconducting T_c enhancement in single layer FeSe/STO^{1,2}. Modifying the STO surface termination and tracing the response of the superconducting gap help to specifically determine the role of the interface structure. It has been reported that STO crystal with mixed TiO₂ and SrO termination can be prepared by adjusting the annealing temperature and atmosphere³. By annealing in O₂, we prepared STO substrates with coexisting TiO₂ and SrO terminations. STM and atomic force microscopy images demonstrate the presence of TiO₂ and SrO surfaces (Figs. 6.1a,b). Closeup STM imaging illustrates that there is a $\sqrt{13} \times \sqrt{13}$ surface reconstruction on TiO₂ and a 3×1 reconstruction on SrO surface (Figs. 6.1c,d). Single layer FeSe grown on this substrate shows 1×1 lattice in FeSe/TiO₂ and 3×1 ordering in FeSe/SrO (Fig. 6.2a). And the superconducting gap size of FeSe/SrO is about 30% smaller than the gap of FeSe/TiO₂ (Fig. 6.2b). To identify the tuning factor behind this gap size difference, more investigation on the surface reconstruction and the band structure of TiO₂ and SrO surface is expected.

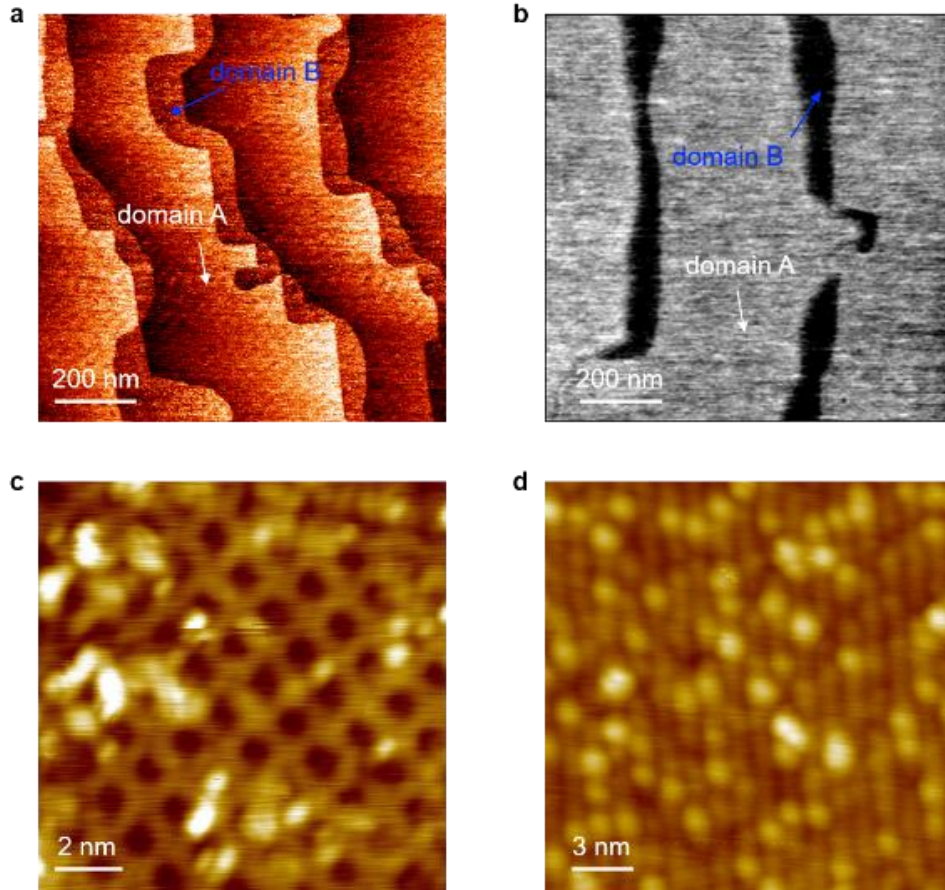


Figure 6.1 a, STM image of STO annealed in O₂ with TiO₂ (domain A) and SrO (domain B) terminations ($V_s = 1.0$ V, $I_t = 0.1$ nA). **b**, Atomic force microscopy image of lateral friction on the same STO sample with TiO₂ and SrO terminations. **c**, STM image of the TiO₂ surface ($V_s = 50$ mV, $I_t = 0.1$ nA). There is a $\sqrt{13} \times \sqrt{13}$ reconstruction. **d**, STM image of the SrO surface ($V_s = 2.0$ V, $I_t = 0.1$ nA). There is a 3×1 reconstruction.

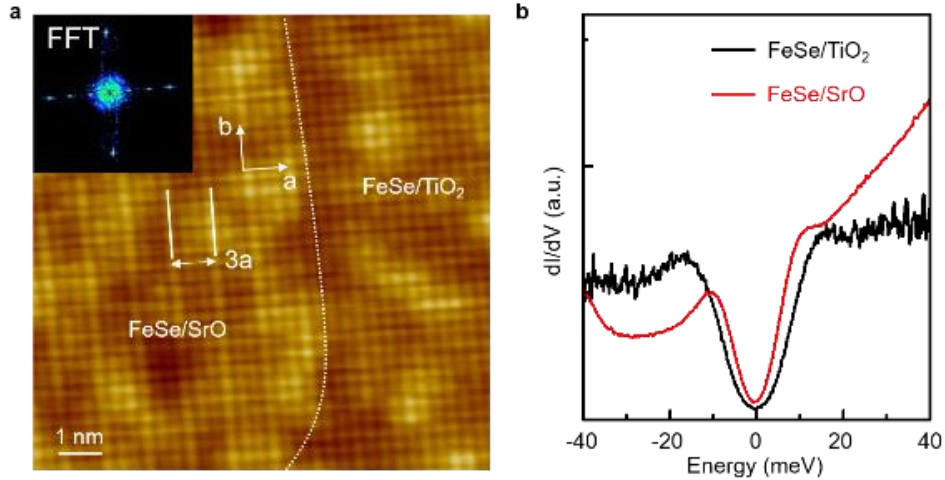


Figure 6.2 a, Atomic resolution STM image of single layer FeSe on STO with mixed TiO₂ and SrO terminations ($V_s = 50$ mV, $I_t = 0.1$ nA). On the right is FeSe/TiO₂. On the left is FeSe/SrO, and there is a 3×1 ordering. The inset is fast Fourier transform of FeSe/SrO, showing the 3×1 ordering. **b**, dI/dV spectra taken on FeSe/TiO₂ and FeSe/SrO. The superconducting gap is 11 meV for FeSe/SrO and 17 meV for FeSe/TiO₂.

6.2.2 Local Superconducting-like Pairing

In the FeSe/STO system, only single layer FeSe on STO is superconducting^{4,5}. For bilayer or thicker layer films, the tunneling spectra are in U shape, showing a semiconducting-like behavior. However, we observe superconducting-like gaps locally at some extended defects on bilayer FeSe (Fig. 6.3) at 6 K. The length scale of the extended defect is 2 to 3 nm, and the local gap size is about 17 meV, which is the same as the gap on the first layer FeSe. Though more investigations on the response of the local gap to increased temperature and applied magnetic field are still needed, this result sheds light on revealing the superconducting pairing mechanism in FeSe.

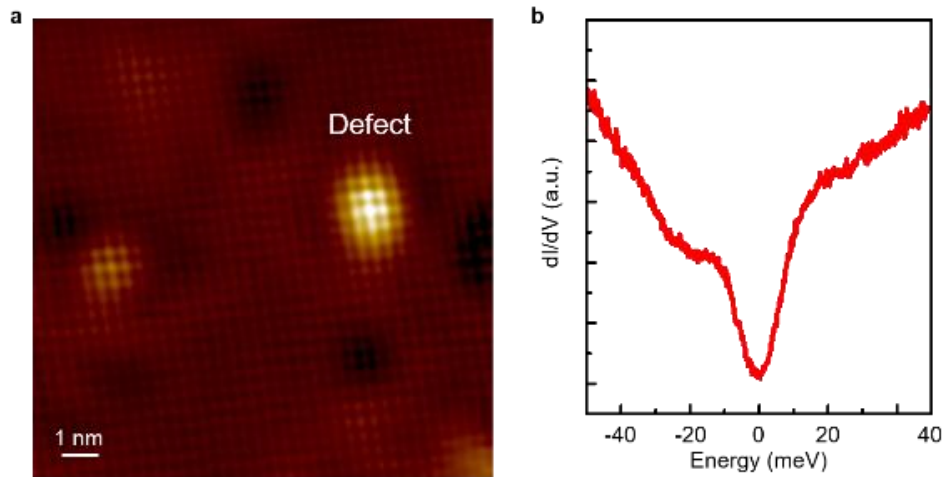


Figure 6.3 a, Atomic resolution STM image of bilayer FeSe on STO ($V_s = -2.0$ V, $I_t = 0.1$ nA). There is an extended defect (bright spot at the top right) on the film. **b**, dI/dV spectrum taken at the extended defect in **a**. The gap is 17 meV.

References

- 1 Dung-Hai, L. What makes the T_c of FeSe/SrTiO₃ so high? *Chinese Physics B* **24**, 117405 (2015).
- 2 Huang, D. & Hoffman, J. E. Monolayer FeSe on SrTiO₃. *Annual Review of Condensed Matter Physics* **8**, 311-336 (2017).
- 3 Koster, G., Kropman, B. L., Rijnders, G. J. H. M., Blank, D. H. A. & Rogalla, H. Quasi-ideal strontium titanate crystal surfaces through formation of strontium hydroxide. *Applied Physics Letters* **73**, 2920-2922 (1998).
- 4 Liu, X. *et al.* Dichotomy of the electronic structure and superconductivity between single-layer and double-layer FeSe/SrTiO₃ films. *Nature Communications* **5**, 5047 (2014).
- 5 Wang, Q.-Y. *et al.* Interface-Induced High-Temperature Superconductivity in Single Unit-Cell FeSe Films on SrTiO₃. *Chinese Physics Letters* **29**, 037402 (2012).

CURRICULUM VITAE

Zhuozhi Ge

zge@uwm.edu

Education

University of Wisconsin Milwaukee, Milwaukee, WI Aug. 2018
Doctor of Philosophy, Condensed Matter Physics

University of Science and Technology of China, Hefei, P. R. China July 2012
Bachelor of Science, Physics

Experimental Skills

- Material Preparation: molecular beam epitaxy (MBE), chemical vapor deposition (CVD)
- Characterization: scanning tunneling microscopy/spectroscopy (STM/S) in ultrahigh vacuum (UHV), scanning electron microscopy (SEM), angular-resolved photoemission spectroscopy (ARPES), Raman spectroscopy, X-ray diffraction (XRD)

Research Experience

West Virginia University, Morgantown, WV 2017-present
Visiting Graduate Research Assistant; Advisors: Lian Li and Michael Weinert

Started and led the research on superconductivity in single layer $\text{FeTe}_{1-x}\text{Se}_x$ on SrTiO_3

- Applied a new phase sensitive approach, the edge scattering effect, to determine the pairing symmetry of single layer FeSe as d wave, which can be generalized to detect the gap symmetry of iron-based superconductors
- Discovered a new factor, the film edge, to facilitate the phase transition from antiferromagnetic order to superconductivity for single layer $\text{FeTe}_{1-x}\text{Se}_x$ ($x < 0.1$)
- Determined the critical size below which superconductivity is suppressed in single layer FeSe nanoribbons, which is critical for further applications
- Studied the impact of interface on superconductivity in FeSe/TiO_2 and FeSe/SrO

University of Wisconsin Milwaukee, Milwaukee, WI 2014-2017
Graduate Research Assistant; Advisor: Lian Li

Collaborated with colleagues investigating topological insulators and transition metal dichalcogenides. Took charge of our lab-moving from Milwaukee to Morgantown

- Discovered two types of step edges in few-layer Sb films and analyzed the topology
- Investigated the dependence of edge states on edge terminations for bilayer WSe_2 on graphene
- Explored the charge density wave in single- and few-layer NbSe_2 films

Presentations and Publications

Conference Presentations

Ge, Z., Yan, C., Agterberg, D., Weinert, M. and Li, L. Suppression of high temperature superconductivity in single layer FeSe nanoribbons. APS March Meeting 2018 Abstracts. Y35.002. Oral presentation delivered at the APS March meeting, Los Angeles, CA, March 2018.

Yan, C., **Ge, Z.** (presenter), Chen, M. X., Weinert, M. and Li, L. MBE growth and electronic properties of 2D topological insulators on Bi₂Te₃. APS March Meeting 2018 Abstracts. E08.009. Oral presentation delivered at the APS March meeting, Los Angeles, CA, March 2018.

Ge, Z., Yan, C., Agterberg, D., Weinert, M. and Li, L. Studies of single layer FeSe nanoribbons on SrTiO₃. APS March Meeting 2017 Abstracts. Y26.008. Oral presentation delivered at the APS March meeting, New Orleans, LA, March 2017.

Ge, Z., Tomer, D., Rajput, S. and Li, L. Impact of impurities on superconducting state of bilayer FeSe/SrTiO₃. American Physical Society (APS) March Meeting 2016 Abstracts. B11.010. Oral presentation delivered at the APS March meeting, Baltimore, MD, March 2016.

Peer Reviewed Publications

Chen, M. X., **Ge, Z.**, Li, Y. Y., Agterberg, D. F., Li, L. and Weinert, M. Effects of interface oxygen vacancies on electronic bands of FeSe/SrTiO₃(001). *Phys. Rev. B*, **94**, 245139 (2016).

Sims, H., Leonard, D. N., Birenbaum, A. Y., **Ge, Z.**, Berlijn, T., Li, L., Cooper, V. R., Chisholm, M. F. and Pantelides, S. T. Intrinsic interfacial van der Waals monolayers and their effect on the high-temperature superconductor FeSe/SrTiO₃. *arXiv:1805.03293* (2018). PRL under review.

Ge, Z., Yan, C., Agterberg, D., Weinert, M. and Li, L. Width-dependent Suppression of Superconductivity in Single Layer FeSe Nanoribbons. Under revision.

Ge, Z., Yan, C., Agterberg, D., Weinert, M. and Li, L. Nodeless *d*-wave superconductivity in single layer FeSe/SrTiO₃ probed by quasiparticle scattering off step edges. Submitted.

Ge, Z., Yan, C., Agterberg, D., Weinert, M. and Li, L. Superconductivity on edge: One-dimensional superconducting channel on the edge of antiferromagnetic single layer FeTeSe nanoribbons. Submitted.

Ge, Z., Yan, C., D., Weinert, M. and Li, L. Tuning superconductivity in single layer FeSe on SrTiO₃ by interface engineering. In preparation.

Yan, C., Chen, M. X., **Ge, Z.**, Weinert, M. and Li, L. Imaging the two types of edge states in few-layer Sb films. In preparation.

Liu, L., **Ge, Z.**, Yan, C., Moghadam, A. D., Weinert, M. and Li, L. Termination-dependent edge states of MBE-grown bilayer WSe₂ islands. In preparation.

Liu, L., **Ge, Z.**, Yan, C., Zhang, H., Weinert, M. and Li, L. Phase transition in 1T/2H NbSe₂ bilayer. In preparation.

Teaching Experience

University of Wisconsin Milwaukee, Milwaukee, WI

Teaching Assistant, General Physics Laboratory

2013-2014

Teaching Assistant, Physics I

2012-2013

Community and Service

Professional Community

American Physical Society

Student Member

2015-present

Campus Community Service

Chinese Student Scholar Association at UWM, Milwaukee, WI

President

2013-2014

Honors and Awards

Chancellor's Graduate Student Award

University of Wisconsin, Milwaukee

2016-2018

Research Excellence Award

University of Wisconsin, Milwaukee

2014-2015

David Lichtman Memorial Scholarship

University of Wisconsin, Milwaukee

2014

Outstanding Leadership Award

University of Wisconsin, Milwaukee

2014

Chancellor's Graduate Student Award

University of Wisconsin, Milwaukee

2012-2013